Surface Chemical Studies of Metal Oxide Nanocrystals Supporting Infrared Localized Surface Plasmon Resonances

A Dissertation
Presented to
The Academic Faculty

By

Weize Hu

In Partial Fulfillment
Of the Requirements for the Degree
Doctor of Philosophy in the
School of Chemical & Biomolecular Engineering

Georgia Institute of Technology
August 2018

Surface Chemical Studies of Metal Oxide Nanocrystals

Supporting Infrared Localized Surface Plasmon Resonances

Approved by:

Dr. Michael A. Filler, Advisor
School of Chemical & Biomolecular Engineering
Georgia Institute of Technology

Dr. Christopher W. Jones
School of Chemical & Biomolecular Engineering
Georgia Institute of Technology

Dr. Ryan P. Lively
School of Chemical & Biomolecular Engineering
Georgia Institute of Technology

Dr. Zhiqun Lin
School of Materials Science and Engineering
Georgia Institute of Technology

Dr. Baratunde A. Cola
The George W. Woodruff School of Mechanical Engineering
Georgia Institute of Technology

Date Approved: July 18, 2018

ACKNOWLEDGEMENTS

First of all, I would like to thank my advisor, Dr. Michael A. Filler, for his steady and persistent guidance and support on my research over the last 5 years. Under his mentorship, I learned how to overcome challenges and failures. With rich knowledge in the field and serious research attitude, he has always been my role model as a scientist and researcher. In addition, our experience together helped me tremendously on my future career development. I also want to thank to my PhD thesis committee members: Dr. Christopher W. Jones, Dr. Ryan P. Lively, Dr. Zhiqun Lin and Dr. Baratunde A. Cola for their helpful questions and comments on my thesis.

I further thank Dr. Siwei Guo in Dr. Kawajiri's group, for his help on mathematical modeling and late-night discussion on manuscripts. I also thank Mathew Boebinger and Dr. Matthew McDowell at school of mechanical engineering, Georgia Tech, for their assistance with TEM measurements. I would also like to thank current and former Filler lab group members: Dr. Li-Wei Chou, Dr. Saujan Sivaram, Dr. Dmitriy Boyuk, Dr. Martin Ek, Dr. Chengquan Wang, Dr. Gozde Tutuncuoglu and Amar Mohabir for their help in researches and daily life. I want to thank all the people I met in Atlanta, and my good friends Xu Du and Zihao Qu for sharing both good and bad times during these five years. And to my partner, Wenjie Mei; I could not thrive through my hardest time in my life without your passion and company.

In the end, I feel grateful to my parents and entire family for their love and supports. Without them, I could not chase my dream in a foreign country and pursue my PhD degree in chemical engineering

TABLE OF CONTENTS

LIST OF TABLES

LIST OF FIGURES

Pages

SUMMARY

Heavily doped metal oxide nanocrystals exhibit tunable localized surface plasmon resonances in the infrared, a property that is promising for applications in photonics, spectroscopy, and photochemistry. Colloidal synthesis – whereby a nanocrystal grows by continuously adding monomers in the solution – is a scalable and ubiquitous method for doped metal oxide nanocrystal synthesis. Although the plasmonic metal oxide nanocrystals were first demonstrated nearly ten years ago, the interplay between localized surface plasmon, dopants and surface adsorbates remains elusive. The lack of understanding in this interaction hinders the utilization of infrared localized surface plasmon for many applications.

In this thesis, we use *in situ* diffuse reflectance infrared Fourier transform spectroscopy to identify the previously unknown, yet critical, role of gas-phase redox reaction on plasmonic properties in indium tin oxide nanocrystals. We directly observe a dominant influence of oxygen and nitrogen annealing which result in a temperature dependent, reversible localized surface plasmon energy shift above 1000 cm^{-1}. Both high-resolution electron microscopy images and X-ray diffraction patterns confirm there is no obvious structural transformations after either oxygen or nitrogen annealing that account for observed spectral changes. We quantitatively extract the time-resolved LSPR energies at each point the reaction through *operando* IR measurements. A kinetic model, which involves surface reaction and bulk diffusion, allows us to rationalize the underlying physicochemical process and quantitatively connect nanocrystal redox chemistry, solid-state diffusion, carrier density and the localized surface plasmon resonances. This fundamental understanding provides a foundation from which to rationally program nanocrystal structure for a desired spectral response.

Next, we expand the colloidal synthesis to group III doped zinc oxides. Using a hot-injection method, we successfully synthesized aluminum, gallium, and indium doped zinc oxide and fully characterize their structural and optical properties with a suit of techniques. Similar results in LSPR modulation via chemical redox reactions in doped zinc oxide indicates that interstitial oxygen compensation plays a key role in modulating carrier densities for both doped indium oxide and zinc oxide. In addition, due to the dopant atom size difference, the doping profile of indium-doped zinc oxide is completely different from aluminum and gallium doped zinc oxide. The etching experiment demonstrates that a significant amount of indium dopants is segregated on the surface which prevents indium-doped zinc oxide nanocrystals from exhibiting plasmonic properties. We also show that the quality factor of synthesized aluminum and gallium doped zinc oxide, which is 3 times higher than previous reports, is compatible with widely-used infrared plasmonic material, indium tin oxide nanocrystals. These materials are cost-effective and an earth-abundant substitution for indium tin oxide for infrared plasmonic applications.

In the third part of the thesis, we specifically use time-dependent infrared spectroscopy to quantify the increase in desorption rate and show that the desorption rate of two model molecules, indole and benzoic acid, from indium tin oxide nanocrystals is enhanced by as much as 60% upon illumination with broadband low-intensity mid-infrared light. For the first time, we show that the deep subwavelength confinement of infrared light by plasmonic nanocrystals can accelerate a heterogeneous chemical process. While the mechanism of desorption remains to be elucidated, our work clearly shows that the in-coupling of low-energy mid-infrared light into plasmonic nanostructures can affect chemical processes. This initial work is likely to motivate further studies of low energy plasmon-molecule coupling and the resulting chemistry.

Our experiments identify the key role of dopants and redox reaction on the infrared optical properties and show that changes to interstitial oxygen concentration are critical to the LSPRs in metal oxide nanocrystals. This work also provides the first demonstration of the excitation of low-energy LSPR can affect surface chemistry. The fundamental insights of surface chemical studies promise unprecedented control of metal oxide plasmonic properties and functionalities.

CHAPTER 1

INTRODUCTION AND BACKGROUND

Light-matter interactions cover a vast realm of physical phenomena including light reflection, refraction, scattering, absorption and emission. As the size of the matter decreases, the interactions start deviating from macroscopic materials. The recent advances in nanomaterials research has been enabled by advanced synthesis and characterization techniques that allow researchers to systematically explore the light-matter interactions in nanoscale. For example, quantum dots, which are very small semiconductor particles, have distinct optical properties compared to those of larger particles. Their light absorption and emission properties are strongly dependent on the particle dimensions and surrounding environment. Other than quantum dots, plasmonic materials, represent a new group of nanomaterials, are attracting more attention due to its unique light-matter interaction over a wide spectrum range, from ultraviolet to infrared. Various researches have been seeking to synthesize these materials and control their optical properties.

1.1 Localized surface plasmon resonances

The history of localized surface plasmon resonances can date back to the 4^{th} century, when the Romans created the famous Lycurgus cup. The cup is made of a dichroic glass which exhibits different colors depending on the light illumination. It is also one of the earliest known object in which the materials derive its properties from embedded plasmonic nanostructures that exhibit what we know as localized surface plasmon resonance (LSPR). As shown in Figure 1.1(a), LSPR is collective oscillation of free charge carriers at the interface between conductors

and dielectrics in response to an external electromagnetic field. LSPRs have two distinct characteristics: deep sub-wavelength confinement of light and enhanced local electric field. It strongly enhances the absorption and scattering of resonant light by the particles. Due to the dislocation of electron cloud in the particle, the excitation of LSPR also produces a large buildup of electrical field intensity at the particle's surface. Similar to that shown in Figure 1.1(b), the local electric intensity can be enhanced by 10 to 1,000 folds at certain areas on the nanoparticle's surface.

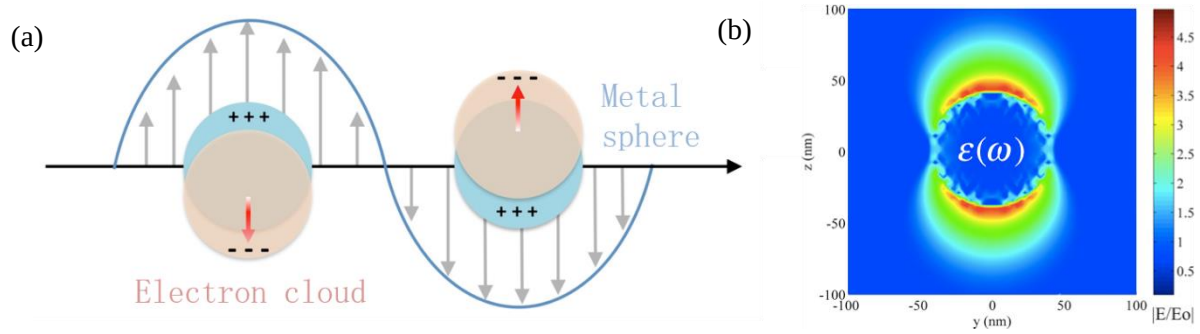

Figure 1.1. (a). Localized surface plasmon resonance schematic where the free conduction electrons of a metal are excited into collective oscillation via coupling of incident light.[1] (b). Simulated spatial distribution of the LSPR-induced electric field enhancement around a sphere.

In order to better describe the LSPRs in small particles, the Drude-Lorentz model is used to quantify collective oscillation of free electrons. The dielectric permittivity of metals, which is given as:

$$\varepsilon(\omega) = \varepsilon_{\infty} - \frac{\omega_p^2}{\left(\omega^2 + i\omega\gamma\right)} \tag{1.1}$$

where ω is the frequency of excitation, ω_∞ is the high frequency dielectric constant of the material, γ is the damping factor associated with scattering of free carriers and ω_p is the bulk plasma frequency which is given by:

$$\omega_p = \sqrt{\frac{ne^2}{m_e \varepsilon_0}} \tag{1.2}$$

where n is the free carrier density, e is the unit of elementary charge, m_e is the effective mass of free carrier and ε_0 is permittivity of free space. The Drude-Lorentz model can also be expressed as a complex function:

$$\varepsilon(\omega) = \varepsilon_r(\omega) + i\varepsilon_i(\omega) \tag{1.3}$$

The real and imaginary parts of the dielectric function are then given as:

$$\varepsilon_r = \varepsilon_\infty - \frac{\omega_p^2}{\left(\omega^2 + \gamma^2\right)} \tag{1.4}$$

$$\varepsilon_i = \frac{\gamma\omega_p^2}{\left[\omega\left(\omega^2 + \gamma^2\right)\right]} \tag{1.5}$$

For very small particles, the optical response is dominated by the dipole contribution. Thus LSPRs are best characterized in terms of the response of a nanoparticle to an external electromagnetic excitation which is given by its electronic polarizability α as:

$$\alpha = 4\pi R^3 \frac{\varepsilon - \varepsilon_m}{\varepsilon + \kappa\varepsilon_m} \tag{1.6}$$

where R is the radius of the particle, ε_m is the dielectric constant of the embedded medium and κ is the shape factor (2 for spheres). The optical resonance will be achieved when the polarizability reaches maximum where the denominator of equation (1.6) approaches zero.

$$\varepsilon_r + \kappa\varepsilon_m = 0 \tag{1.7}$$

Substituting equation (1.4) into (1.7), the localized surface plasmon resonances can be achieved as:

$$\omega_{lsp} = \sqrt{\frac{\omega_p^2}{\left(\varepsilon_\infty + \kappa\varepsilon_m\right)} - \gamma^2} \tag{1.8}$$

which can typically be approximated as:

$$\omega_{lsp} = \frac{\omega_p}{\sqrt{\left(\varepsilon_\infty + \kappa\varepsilon_m\right)}} = \sqrt{\frac{ne^2}{m_e\varepsilon_0\left(\varepsilon_\infty + \kappa\varepsilon_m\right)}} \tag{1.9}$$

since γ is much smaller than the optical frequencies of interest and can be neglected. The equation shows that LSPR frequency is dependent on the carrier density, free carrier effective mass, geometry of the particle, as well as the dielectric constant of surrounding environment. Equation 1.9 has been effectively used to describe LSPR frequency responses, and will play an important role in this thesis.

1.2 Traditional plasmonic materials and its applications

As LSPR was first discovered in metallic particles, the majority of literature on localized surface plasmons focus on noble metals. The most common plasmonic metals namely, gold, silver and copper have free electron densities in the range of 10^{23} cm^{-3} with corresponding LSPRs in the visible. Localized surface plasmon can strongly couple resonant light to the metallic nanostructures and have demonstrate its potentials for many sensing and energy applications.

1.2.1 Chemical sensing

One of the major applications of plasmonics is in chemical sensing. Owing to the capability of near field enhancement, surface plasmon resonances play the central role in the

surface enhanced Raman spectroscopy (SERS). The theoretical SERS EM enhancement factor scales as fourth power of field enhancement at the nanoparticle surface.[2-3] For a typical metal nanoparticle, the field enhancement is approximately increased by a factor of 10, thus, the magnitude of the SERS EM enhancement is 10^4 to 10^5.[4] As a robust and effective analytical technique, SERS has been applied to many analytical systems in recent years.[5-8] Recent advances in nanoparticle device fabrication allow the Raman enhancement up to 10^{10} which enable of probing single molecule on a single nanostrucuter.[9-11]

Another fully-fledged chemical sensing technique using LSPR is wavelength-shift LSPR sensing. As described in equation (1.9), the resonant frequency ω_{lsp} is sensitive to the local dielectric environment ε_0. Thus, changes in the local environment - such as through the presence of an adsorbate - should cause a shift in resonant frequency. The optical response enables an ultra-fast and real-time detection of surrounding environment which has been demonstrated for a number of systems in molecular-adsorption detection[12] and biosensing.[13-14] Moreover, recent work pushes the sensitivity of plasmonic gas sensors to a single-particle level by coupling the plasmonic nanostructure with a gold antenna (Figure 1.2 (c) and (d)).[15]

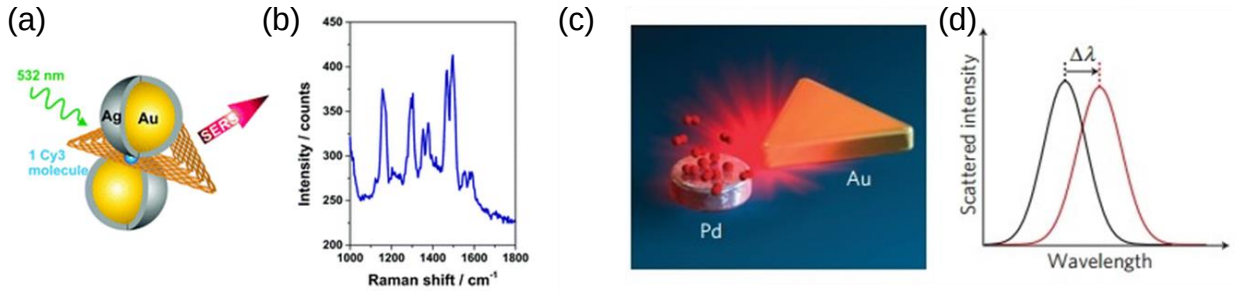

Figure 1.2 Localized surface plasmon enhanced chemical sensing: (a) Au nanoparticle dimers formed using DNA origami substrate, with Raman enhancement up to 10^{10}; (b) SERS spectrum of a single Cy3 molecule.[11] (c) Hydrogen sensing using a resonant antenna-enhanced scheme; (b)

Hydrogen absorption on the palladium particle changes its complex dielectric function, which causes a resonance shift ($\Delta\lambda$) of the gold antenna that can be optically detected.[15]

1.2.2 Catalysis

It is well known that noble metals can be used as catalysts for a wide range of chemical reactions. Conventionally, there are two catalytic mechanisms affect the reaction which are thermal-driven and charge-carrier-driven mechanism. The excitation of LSPR in the plasmonic metals yield an excited, athermal electron distribution, which can induce photochemical reactions either through resonant heating of the nanostructure or by transferring of energetic charge-carriers to the surface reactant during the plasmon decay process. In details, the charge-carrier transfer route can be classified into two categories: indirect hot-electron transfer mechanism and direct intramolecular excitation mechanism. As shown in Figure 1.3 (a), in the indirect hot-electron transfer mechanism, the surface adsorbates are excited through transferring the hot-electrons generated via nonradioactive decay of a localized surface plasmon to lowest unoccupied molecular orbital. For the direct charge transfer mechanism, the localized surface plasmon directly excites electrons from highest occupied molecular orbital to lowest molecular orbital in the adsorbate without metal to adsorbate charge transfer (Figure 1.3 (b)).

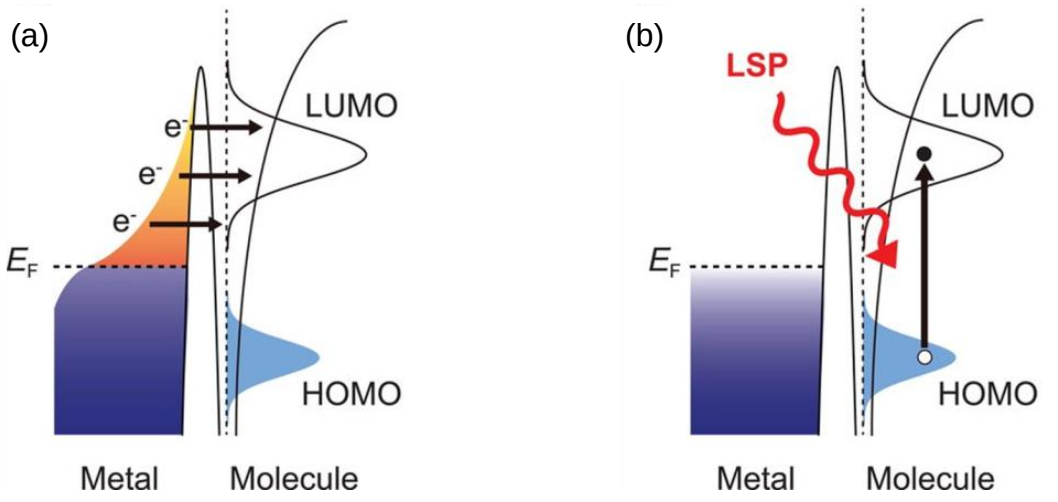

Figure 1.3. Charge-carrier excitation mechanisms for plasmon-induced chemical reactions.[16] (a) Indirect hot-electron transfer mechanism. (b) Direct charge transfer mechanism.

Although the underlying mechanism of plasmonic photocatalysis is still under debate, a number of plasmon enhanced reactions have been demonstrated on metal nanostructures including water splitting,[17-19] hydrogen dissociation,[20] ethylene epoxidation,[21-22] and methane formation.[23] But more recent studies on dye molecules interaction with excited plasmonic metal nanostructure using *in situ* Raman[24-25] and scanning tunnelling microscope[16] shows more solid evidence supporting a direct charge transfer mechanism. As a result, by engineering plasmonic nanostructures with resonant wavelengths matching the charge excitation energies of adsorbates, plasmonic materials shows the potential capability of selectively activation of targeted chemical bonds, ultimately, modifying the reaction pathways.

1.2.3 Photovoltaics

Photovoltaics, the conversion of sunlight to electricity, is growing rapidly over past 10 years. The total production of photovoltaics reaches 300 GW by the end of 2016.[26] In order to

keep up the pace of the demand in the industry, next generation photovoltaics require highly efficient conversion of sunlight to electricity while maintaining low costs. However, conventional wafer-based crystalline Si solar cells pose a tradeoff between absorption efficiency and carrier diffusion lengths. The prior requires higher physical thickness, but the latter benefits from a lower thickness.

Coupling the metal nanostructures, which possess strong light-matter interactions from its plasmonic properties, into a photovoltaic device can increase the absorption efficiency, and thus reduce the physical thickness of the photovoltaic absorber layers. As shown in Figure 1.4, there are three approaches to improve the efficiency.[27] First of all, by using metallic nanopartilcles as subwavelength scattering elements at the surface of the solar cell, sunlight is preferentially scattered and trapped into the semiconductor thin film by multiple and high-angle scattering. Second, plasmonic near-field enhancement from metallic nanoparticles can increase semiconductors' effective absorption cross-section, and thus improve the photovoltaic efficiency. In the last approach, light can be trapped by the excitation of surface plasmon polariton at the metal/semiconductor interface. By engineering the device materials, absorption of the surface plasmon polariton in the semiconductor can be stronger than in the metal. As a result, the surface plasmon polariton coupling can focus light into semiconductor layer to improve the efficiency.

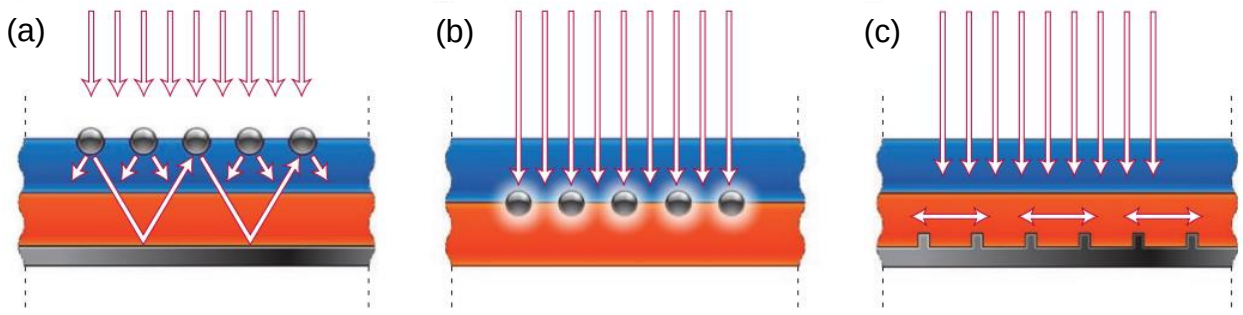

Figure 1.4. Plasmonic light-trapping geometries for thin-film solar cells.[27] (a) Light trapping by scattering from metal nanoparticles at the surface of the solar cell. (b) Light trapping by the

excitation of localized surface plasmons in metal nanoparticles embedded in the semiconductor. (c) Light trapping by the excitation of surface plasmon polaritons at the metal/semiconductor interface.

1.3 Heavily doped semiconductor materials

A number of applications such like photothermal therapy,[28-29] surface enhanced infrared spectroscopy (SEIRS),[30] long-wavelength wave guiding[31] and surface plasmon polariton assisted heat transfer[32] require LSPRs to expand to infrared regime. However, the charge carrier concentration is intrinsically fixed in the conventional plasmonic metals. The factor that plasmonic frequency is predominately governed by charge carrier density N which is one of the main hindering factors metal plasmonic response in the lower energy spectrum. The nature of high charge carrier concentration in metals restrict the LSPR to in the visible regime. In addition, both real and imaginary part of the dielectric permittivity of gold and silver become extremely large which cause the field enhancement vanish. As a result, noble metals is not an ideal material for supporting LSPR in the infrared.

Degenerately doped semiconductors with tunable charge-carrier concentrations (10^{19} - 10^{21} cm^{-3}), represent a new group of plasmonic materials that offer an alternative to traditional metals across a wide range of optical spectrum from visible to far-infrared. Compared to the fixed charge carrier density in metals, the tunable carrier density via chemical doping or post synthetic chemical, photochemical and electrochemical reactions provide an extra degree of freedom to design the optical properties in these materials. By material type, the doped plasmonic semiconductors can be classified into four different groups, metal chalcogenides,

metal nitrides, doped group IV materials and transparent conductive oxides (TCOs), each with their own advantages and disadvantages.

Some binary copper and mercury chalcogenide compounds are intrinsically cation vacancy doped semiconductors that support LSPR in near-IR.[33-34] Early experimental and theoretical studies of these metal chalcogenide nanocrystals provide some crucial fundamental insights, like size and dopant profile effect, to plasmonic semiconductors.[35-36] However, due to its nature of cation vacancy doping mechanism, metal chalcogenides are sensitive to ambient oxygen which will destabilize its LSPR properties.[37] Metal nitrides sustain remarkably high carrier concentration, up to 10^{22} cm^{-3} in TiN, which make them a substitution for Au or Ag for application concerning LSPR in the visible spectrum.[38] Although is reported that the optical properties of metal nitride can be adjustable by chemical reactions,[39-40] it can hardly lower the energy to mid-infrared region. Another group of plasmonic semiconductor materials is doped group IV materials. Since group IV materials such as Si and Ge are dominant in the semiconductors industry, there are rich literatures regarding to their synthesis, doping and surface chemistry. Although, plasmonic Ge nanostructures remain a challenge, many reports have demonstrated the tunable LSPR properties in doped Si nanowires[41-42] and nanocrystals.[43-45] Due to the fact that intrinsic Si has very low carrier concentration, the substitutional doping, like P and B, is required to induce plasmonic properties located in mid-infrared. Since the synthesis of heavily doped Si nanostructure depends on gas-phase reaction which are nonthermal plasma synthesis[44-45] or chemical vapor deposition,[41-42] the yield and uniformity are the main limitations for plasmonic Si nanostructures.

Transparent conductive oxides (TCOs) can be doped much higher than many other semiconductors (such as silicon) which gives them metal-like optical properties in the near and

mid-IR. The list of potential plasmonic TCO materials has expanded to doped molybdenum oxide,[46] tungsten oxide,[47] cadmium oxide,[48] indium oxide[49-50] and zinc oxide.[51-52] Among them, tin doped indium oxide (ITO) and aluminum doped zinc oxide (AZO) attract the most attention due to its low-toxicity, ease of synthesis,[50, 53] and widely tunable LSPR from near- to mid-infrared (Figure 1.5). More importantly, ITO and AZO possess great chemical stability under ambient conditions due to its aliovalent doping and crystal structure.[49-50, 53] However, on the other hand, oxygen vacancy doped WO_{3-x} and MoO_{3-x}[46-47] are not stable when exposing to the oxygen which are similar to metal chalcogenides. Here, understanding the doping mechanism of doped metal oxide is crucial to explain the tunability and stability in degenerately doped metal oxides.

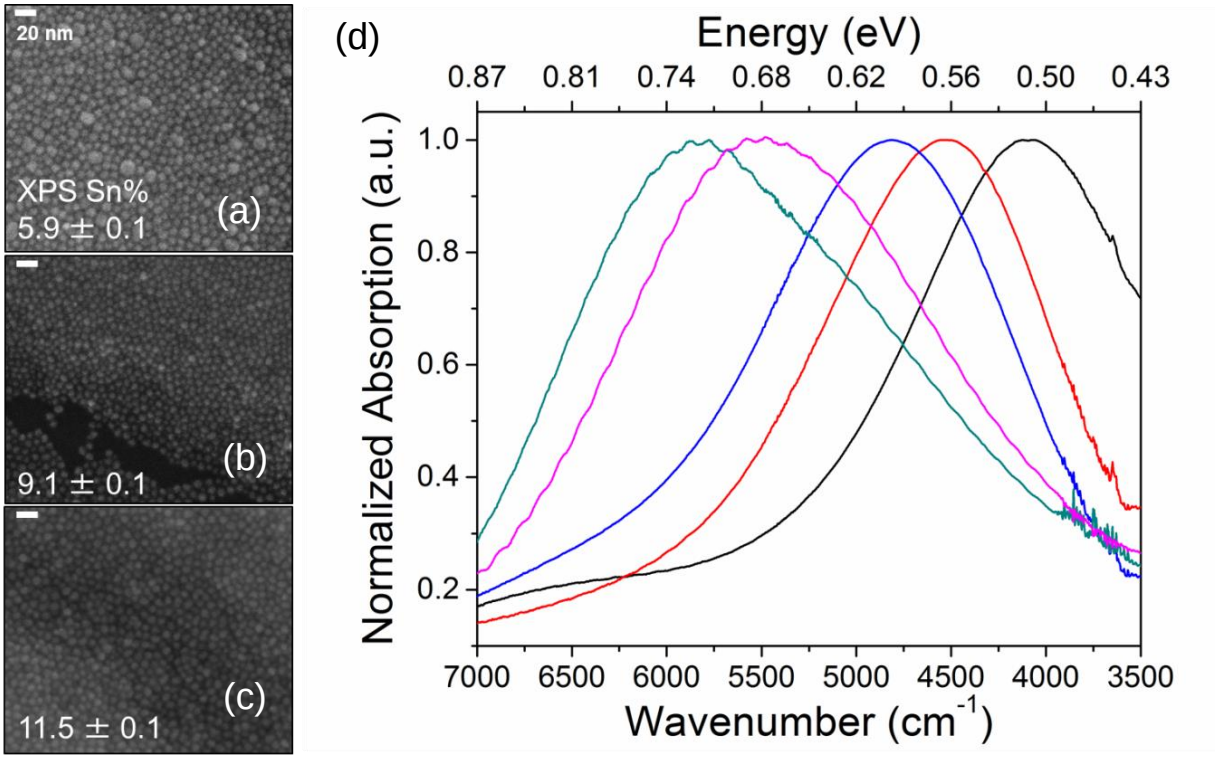

Figure 1.5. SEM images of TIO nanopartilcles of varying doping concentrations (a) 5.9 ±0.1%, (b) 9.1 ±0.1% and (c) 11.5 ±0.1%; (d) LSPR extinction spectra in solvent dispersion supported by ITO with different doping concentrations

1.4 Doping mechanism

Doping is the intentional introduction of impurities into an intrinsic semiconductor for the purpose of modulating its physical properties. Recently, a number of conductivity, luminescence and absorption studies of doped metal oxide, along with the references found in the bulk materials, elucidate the underlying doping mechanism. The free charge carrier in these materials is generally generated by three sources: defect/vacancy doping, aliovalent substitutional doping and extrinsic interstitial doping

1.4.1 Aliovalent substitutional doping

As a fundamental building block in microelectronic industry, semiconductors are commonly doped with aliovalent substantial dopant for tuning their physical properties. In this approach, a lattice atom is substituted with one of higher or lower valence, donating a free electron or free hole to the conduction band or conduction band respectively. Aliovalent substitutional doping has been widely employed to produce transparent conduction oxides with high carrier densities, including ITO,[49] AZO[54] and etc. Since the conduction band in metal oxides is largely derived from the valence orbitals of metal cations, substituting a higher valence cation can introduce extra electrons to the conduction band and create n-type semiconductor. For example, by substituting In^{3+} by Sn^{4+}, three electrons of Sn atom form ionic bonds with nearby oxygen and one extra electron can be donated to conduction band. However, such free carriers can be compensated by other ionic defects in metal oxides including oxygen interstitials through following reaction:[55]

$$O_i^{''} + 2e^- \rightleftarrows O_i^{2-}$$

where $O_i^{''}$ is interstitial oxygen. On the other hand, p-type semiconductor can be created by substitution of lower valence and compensated by oxygen vacancy.

1.4.2 Vacancy doping

Anion/cation vacancy doping provides another way to dope the semiconductor material without the need for dopants of atoms different from the intrinsic composition. The vacancies effectively dope the materials through complete or partial free charge compensation of deficient cations or anions. Metal oxide are commonly anion vacancy doped which is realized by oxygen vacancies. Oxygen vacancies are doubly charged, allowing up to two free electrons to be donated to the conduction band, leading to LSPR in the reduced form of tungsten oxide and molybdenum oxide (WO_{3-x} and MoO_{3-x}).[49-50, 53] Cation vacancy doping is commonly seen in metal chalcogenide nanocrystals. For example, $Cu_{2-x}S$ are self-doped through the creation of copper vacancies and holds LSPR in near-IR.[33-34]

1.4.3 Extrinsic interstitial doping

Interstitial doping is rarer than the previous two doping approaches. It is only feasible in metal oxides with crystal lattice large enough to accommodate an extrinsic dopant to sit in the interstitial sites without inducing a structural phase change. The extra interstitial cations can donate their charges into conduction bands. The plasmonic properties in extrinsic interstitial doped metal oxide has been shown in tungsten bronze (M_xWO_3) with alkali cations (Li^+, Na^+, Cs^+, or Rb^+) as dopants.[56]

1.5 Tunability of LSPR in semiconductor nanostructures

Owing to the nature of semiconductor materials, LSPRs supported by doped metal oxide nanocrystals can be dynamically modulated through tuning their carrier concentration without changing morphologies or surroundings. The tunability in both resonant energy and intensity of LSPR supported by semiconductor nanocrystals has been demonstrated through various approaches including (1) chemical redox reactions, (2) electrochemical charging, and (3) photodoping

1.5.1 Chemical redox reactions

Semiconductor nanocrystals can participate into redox reactions as an oxidant or reductant by accepting or donating their conduction or valence band electrons. Early demonstrations of this approach mainly focus on defect/vacancy doped plasmonic materials. For example, copper sulfide nanocrystals can react with oxidants, I_2, to create Cu vacancies which increase holes and carrier density.[57] As a result, LSPR energy blue-shifts and intensity increases. Then, by adding reductant which is sodium biphenyl, it will refill the hole and red-shift the LSPR. The chemical redox reaction approach has also been demonstrated in plasmonic metal oxide. There is a slightly red-shift on ITO nanocrystals when they are exposed to oxidant cerium nitrite and shift back when exposed to reductant sodium ascorbate.[58]

1.5.2 Electrochemical charging

In conventional semiconductor device such as capacitors or battery-type cells, an external bias will lead to accumulation or depletion of charge carriers at the interface. From band structure point of view, the external voltage shifts the Fermi level which change the equilibrium carrier concentration in the semiconductor material, thus achieving on-demand tuning of their

carrier density. For plasmonic metal oxide, it is first demonstrated in ITO nanocrystal thin film.[59] The LSPR supported by ITO nanocrystals shifts to higher energy while applying a negative bias. As a following study, Milliron et al. have expanded this approach to ITO nanocrystals in NbO_x glass composites. By varying the external bias, the composites have the capability of voltage-selective control of transmittance between visible and NIR for dual-band electrochromic smart window.[60]

1.5.3 Photodoping

The excitation of electrons from valence band to conduction band by illumination has been widely studied in photo-catalytic systems after Fujishima and Honda's finding of photolysis of water at semiconductor electrode.[61] By promoting electrons in valence band to conduction band, we can dynamically tune the electron density, thus the LSPR in semiconductor nanocrystals. The first demonstration of photodoping is on ZnO nanocrystals. Upon UV illumination, promoted electrons in conduction band are stabilized by using ethanol as a hole scavenger.[62] This approach has also been applied to aliovalent-doped metal oxide.[63] The study shows that photodoping can tune the carrier density in both doped and undoped In_2O_3 nanocrystals to a similar concentration.

1.6 Interplay between LSPR and surface reactions

It is worth noting that all the LSPR modulations on doped metal oxide nanocrystals are conducted in solution phase such as solvents in chemical redox reactions, electrolytes in electrochemical charging and hole scavengers in photodoping. There are situations where spectral response changes desirably in a gas environment. However, the complex interplay of

doping mechanisms in doped metal oxide and its interaction with surface reactions convolutes the problem.

In this thesis, we seek to quantitatively demonstrate the influence of the surface redox reaction on LSPRs supported by doped In_2O_3 and ZnO nanocrystals. Time-resolved spectroscopic data coupled with a transient model are used to establish a connection between surface redox chemistry, carrier density, and the LSPR of metal oxide nanocrystals. On the other hand, the plasmonic effect on surface adsorbates are studied using a molecular desorption system. Both studies rely on *in situ* infrared spectroscopy to probe the LSPR absorptions and surface adsorbate change during these reactions. Overall, this thesis seeks to develop a general methodology to engineer the optical properties in plasmonic metal oxide nanocrystals and demonstrate their possible applications in local energy delivery.

CHAPTER 2

METHODS

Plasmonic metal oxide nanocrystals are synthesized in a standard Schlenk line setup. This chapter provides theory and experimental details for synthesizing these nanocrystals using colloidal synthesis and characterizations of their structural and optical properties with various spectroscopic and microscopic techniques.

2.1 Metal oxide nanocrystal colloidal synthesis

A typical colloidal synthetic system to prepare colloidal nanocrystals is composed of three major components: metal precursors, organic surfactants, and solvents. In some circumstances, solvents can serve as surfactants as well. (e.g. oleylamine in ITO nanocrystal synthesis) Precursors are generally organometallic compounds or metal salt, which will be decomposed into reactive chemical species in atomic or molecular form (monomers) before nucleation and growth. For metal oxide nanocrystal formation, the precursors are mainly metal carboxylates, which possess of a metallic cation and a long chain carboxylic acid such as oleic acid, stearic acid, etc. As the initial step of forming metal oxide nanocrystals, the building block, $M(OH)_n$ monomers, can be formed by aminolysis, alcoholysis or hydrolysis of the precursors depending on the lysing agents (Figure 2.1). While these reactions are running at high temperatures (~200 °C), the nucleophiles, amines or alcohols, normally possess long hydrocarbon chains to prevent evaporation.

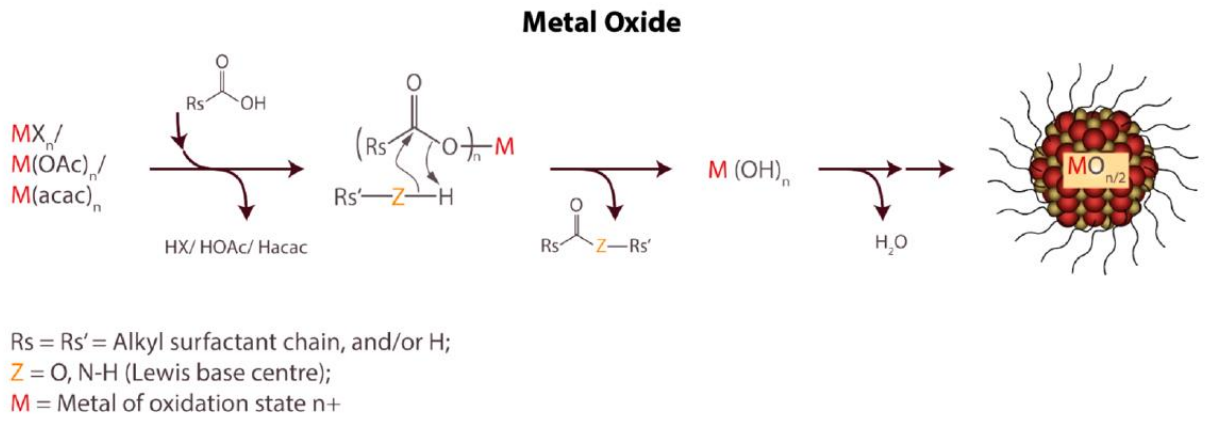

Figure 2.1. Reaction pathway for metal oxide nanocrystal formation: metal carboxylate formation and subsequent lysis with a suitable protic moiety.[64]

The evolution of monomer concentration in the solution tracks each stage of the nanocrystal growth. As shown in Figure 2.2, the growth can be divided into three stages, which are monomer generation, nucleation, and nanocrystal growth. In the first stage, as the lysis reaction continues, the monomers will keep increasing and finally reach saturation in the solution. Due to the presence of energy barriers for nucleation, the monomers do not spontaneously nucleate even when the monomer is saturated in the solution. Beyond supersaturation of monomer, when the critical concentration of the monomer is achieved, nucleation happens. The burst nucleation rapidly consumes the monomers in the solution, and leads to a quick decrease in the monomer concentration. Additional nucleation events do not occur since the monomer concentration drops below and would hardly accumulate back to the critical concentration as the growth step comes in. After nucleation, the nuclei grow by continuously consuming monomers. As shown in the plot, the growth stage is accompanied by a continuous drop in monomer concentration which reaches the saturation concentration eventually. Surfactants, with long alkyl chains will coordinate nanocrystal surfaces to passivate the dangling bonds during the growth.

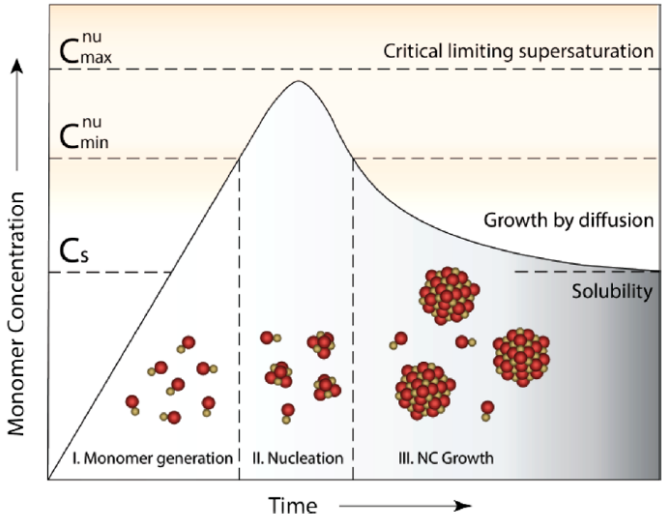

Figure 2.2. LaMer-Dinegar model of colloidal nanocrystal formation. The three stages of monomer generation, nucleation, and growth are demarcated in the region below the growth curve along with cartoons depicting the progression of the synthesis.[64]

For practical operation, the colloidal synthesis techniques can be divided into three major approaches: (1) heat-up, (2) hot-injection, and (3) continuous injection. The primary difference in the nanocrystal formation between these methods lies in the temporal separation of the events of nucleation and growth. For the heat-up approach, all the chemicals (precursors, surfactants, and solvents) involved in the synthesis are mixed in a single flask and heat up to initiate nucleation and subsequent growth. The advantage of this approach is ease of scale-up and a higher degree of reproducibility due to the simplicity of the synthesis process. However, it suffers from the issue of broad size and shape distribution due to the possibility of overlapping between nucleation and growth stage. Hot-injection method can avoid this issue as an instantaneous burst nucleation is achieved upon a quick injection. During this short period of time, a high degree of supersaturation is induced and creates a single nucleation step. Generally, a narrower size and shape distribution can be achieved using hot-injection method. Last but not

least, the continuous injection method is an intermediate approach combining the advantages and disadvantages of previous approaches. One remarkable difference is that continuous injection can allow the synthesis of core-shell heterostructure by changing the reactant solution during the nanocrystal growth process.[65]

2.2 Sample preparation

Both Sn doped In_2O_3 and Al/Ga/In doped ZnO nanocrystals are synthesized in the Schlenk line set up shown in Figure 2.3. The vacuum line is connected to a rotary vane pump (Edwards, RV5) and holds a base pressure of 50 mTorr. A thermal couple is inserted into the solution to monitor the reaction temperature. ITO nanocrystals are synthesized using heat-up approach and AZO/GZO/IZO nanocyrstals are synthesized using hot-injection approach. The detailed synthesis procedures are shown below and summarized in Table 2.1

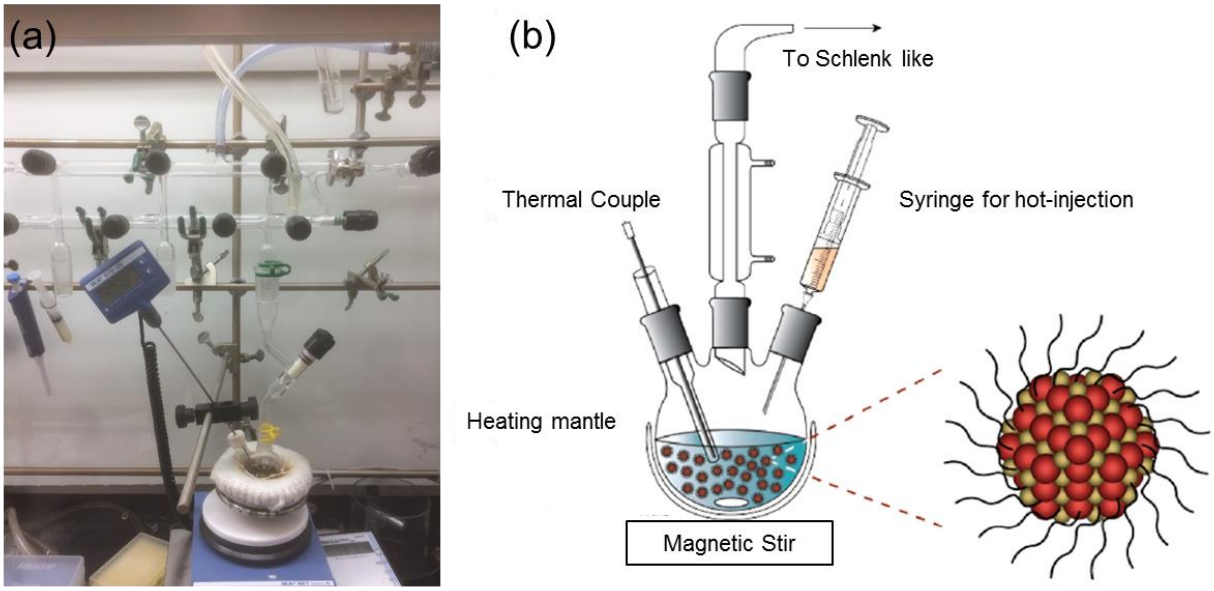

Figure 2.3. (a) Schlenk line setup used to synthesize ITO and doped ZnO nanocrystals in the lab. (b) Schematic of glassware setup for nanocrystal synthesis using hot-injection approach. A two-neck flask without syringe is used to heat-up approach. (Adapted from reference [64])

2.2.1 Tin doped indium oxide (ITO) nanocrystals

A solution containing 0.5 mmol indium acetylacetonate ($In(acac)_3$), 0.027 mmol tin bis(acetylacetonate) dichloride ($Sn(acac)_2Cl_2$) in 7g of oleylamine (OA) was mixed in a 50 mL two-necked flask and then connected to the Schlenk-line setup. Three times of pumping and refilling with N_2 are applied subsequently to eliminate oxygen in the system. The reaction is carried out at 250 °C for 5 hours with magnetically stirring and nitrogen flowing. A thermocouple is inserted into the flask in order to monitor the reaction temperature. The solution turned clear as the precursor salts dissolved, and processed to light yellow while temperature ramp up to 200 °C. Upon reaching 250 °C, a dark blue-green color was observed and lasted during the whole reaction period.

The resulting reaction mixture is precipitated by adding ethanol (30mL) and centrifuged at 3000 rpm for 10 minutes to remove the supernatant. The ITO particles are further cleaned by another two cycles of redispersion in hexane, reprecipitation with ethanol and centrifugation. During redispersion, 20 μL OA and 40 μL oleic acid (OLAC) are added to further stabilize the nanocrystal dispersion. Finally, the ITO nanoparticles are dispersed in a hexane. Different Sn doping concentration is achieved by varying the amount of Sn precursor added. All other procedures remain the same. Approximately 50 mg of ITO nanoparticles with ~10 nm diameters are synthesized in each batch.

2.2.2 Aluminum, gallium, indium doped zinc oxide (AZO, GZO, IZO) nanocrystals

In a 20 mL of glass vial, a precursor solution A containing Zinc sterate ($Zn(St)_2$) (1 mmol), $Al(acac)_3$ (0.1, 0.2, and 0.3 mmol), or $Ga(acac)_3$ (0.1, 0.2, and 0.3 mmol) or $In(acac)_3$ (0.05, 0.2, and 0.5 mmol) and OA (3 mmol) in 4 ml of 1-octadecene (ODE) is magnetically stirred at 140 °C for 1 h. In a separate 50 mL of three-neck flask, solution B containing 10 mmol

of 1,2 hexadecanediol (HDDIOL) in 11 mL of ODE is magnetically stirred and heated to 140 °C for 1 h under N_2. Both solutions turn clear during the heating. The precursor solution A is injected quickly into solution B using a syringe when the temperature of solution B reaches 230 °C. The temperature of the reaction mixture drops and then keeps at 210 °C for 5 h for the growth of doped ZnO nanocrystals. Upon injection of solution A to solution B, the mixture turns into yellow while reaction goes.

When the reaction mixture is cooled down to room temperature, ethanol is added to the reaction mixture to precipitate the nanocrystals out of the solution. The doped ZnO nanocrystals were then collected by centrifugation (5000 rpm for 10 min). After two cycles of redispersion in hexane (2 mL) and reprecipitation by ethanol, 20-30 mg of precipitate is eventually collected and dispersed in 10 mL of hexane.

Table 2.1. Summary of synthesis chemicals and conditions for doped In_2O_3 and doped ZnO nanocrystals.

Nanocrystals	**Method**	**Precursors**	**Surfactants**	**Solvents**	**Rxn Cond.**
ITO	Heat-up	$In(acac)_3$ $Sn(acac)_2Cl_2$	OA	OA	250 °C for 5 h
AZO/GZO/IZO	Hot-injection	$Zn(St)_2$ $Al(acac)_3$ $Ga(acac)_3$ $In(acac)_3$	HDDIOL, and OA	ODE	140 °C for 1 h and then 210°C for 5 h

2.3 Sample characterizations

2.3.1 Infrared spectroscopy

Infrared spectra are commonly obtained by passing infrared light through a sample and determine what fraction of the incident light is absorbed at a particular energy. As a powerful and non-destructive tool, IR spectroscopy is used to characterize localized surface plasmon absorptions in plasmonic nanocrystals, as well as surface adsorbates on the nanocrystal surface *in situ*. All the IR spectra are collected by a Fourier transform infrared (FTIR) spectrometer (Bruker, Vertex 70) equipped with a narrow-band liquid N_2-cooled HgCdTe (MCT) detector. The detection infrared light is generated by a broadband Si Globar. Depending on the interested spectrum range, a KBr (mid-infrared) or CaF_2 (near-infrared) beam splitter is installed for Fourier transform operation.

There are two spectra collection geometries employed in this system: reflection and transmission. As shown in Figure 2.4, a diffuse reflectance accessory (Harrick Scientific Products, Praying Mantis) is installed in the spectrometer for reflection geometry measurements. In the diffuse reflection accessory, the sample (powders or thin film with reflection layer) is placed in the reaction chamber which is backed up with a rotary pump (Edwards, RV12). Two mirrors in the accessory direct the incident infrared beam onto the sample, and the other two guide the reflective beam to the detector. The reaction chamber is composed of two gas inlets, one gas outlet, a heating crucible, and a sealing dome. The reaction chamber enables a closed system for time- and temperature-dependent IR characterizations of plasmonic nanocrystals. Various reaction gases including N_2, O_2, H_2 and H_2O can be dosed into the reaction chamber through mass flow controllers (MKS Instruments, 1479A) or manually controlled leak valves. The top dome of the reaction chamber contains ZnSe (or CaF_2) windows to enable infrared light input and output. A convection gauge (Duniway Stockroom Corp., CVT-275) is applied to monitor the pressure inside of the reaction chamber and the base pressure is 5 Torr.

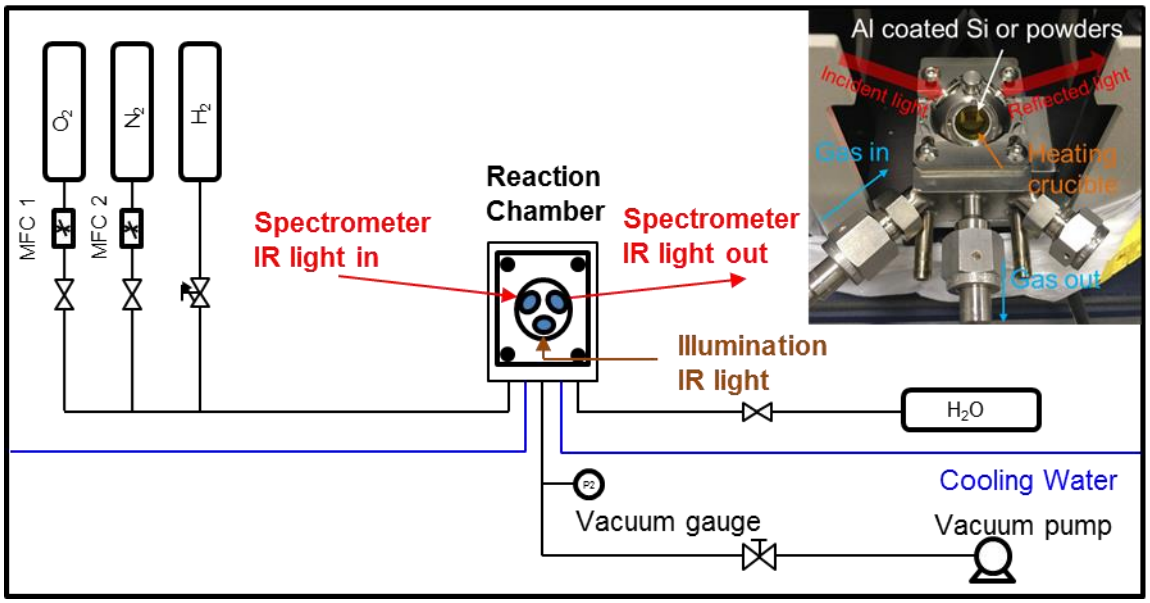

Figure 2.4. Schematic diagram of *in situ* diffuse reflectance infrared spectroscopy setup and gas delivery system.

The IR transmission measurements use a transmission film holder (Figure 2.5). Metal oxide nanocrystals are spin-cast onto highly IR transparent Si substrate. Then, the transmission geometry can collect angle-dependent IR absorption of nanocrystal thin films using blank Si as background.

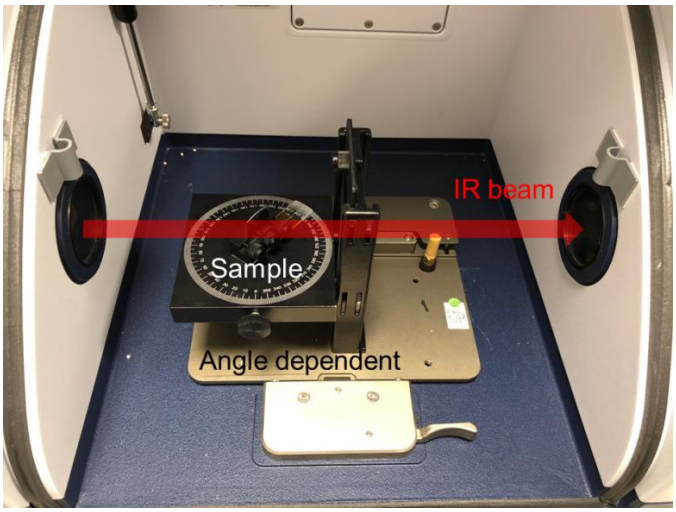

Figure 2.5. Illustration of thin film transmission measurement with transmission film holder.

2.3.2 Beer-Lambert Law

In order to quantitatively study the surface adsorbates using IR spectroscopy, the Beer-Lambert law which relates the absorption of light to the properties of the material plays the essential role. From mathematical point of view, it is the linear relationship between absorbance and resonator numbers. Spectrometers usually measure in terms of transmittance (T), which can be expressed as:

$$T = \frac{I}{I_0} \tag{2.1}$$

where I is the light intensity after it transmitted through the material and I_0 is the incident light intensity. The Beer's law relates the transmittance to the arbitrary cross-sectional area (σ), optical length (l) and numbers of resonators (N). The attenuation of light through a thin slab of material can be described in the following equation:

$$d\left(\frac{I}{I_0}\right) = -\sigma \bullet N \bullet dz \tag{2.2}$$

where dz is the thickness of the slab. Integration on both side:

$$\ln(I) - \ln(I_0) = -\sigma \bullet N \int dz \tag{2.3}$$

$$\ln\left(\frac{I}{I_0}\right) = -\sigma N l \tag{2.4}$$

By definition, the light absorbance (A) is:

$$A = -\log(T) = -\log\left(\frac{I}{I_0}\right) = -\frac{1}{2.303}\ln\left(\frac{I}{I_0}\right) = \frac{1}{2.303}\sigma N l \tag{2.5}$$

It correlates the absorbance to the number of resonators linearly.

While there are several assumptions need to be clarify before the validation of absorbance quantification. First of all, for the same material, the absorption cross-sectional area

(σ) or the molar absorptivity is constant. Since molar absorptivity is a fundamental constant for a pure molecule at a given wavenumber of absorption, which depends on the electronic structure of a molecule and how it changes during a vibration, this assumption is generally valid. Second, the light path is constant. As our detection geometry is fixed, this assumption is also valid as well. At last, the intermolecular interactions which is the peak width need to be consistent so that it can contribute to same peak height. By validate the above three assumptions, the Beer-Lambert law allows us quantitatively calculate the surface adsorbates using IR peak intensities.

The validation of Beer-Lambert law in our system is confirmed by the ligand removal experiment. The as synthesized plasmonic ITO nanocrystals are capped with hydrocarbon ligands to passivate the surface. By annealing at relative low temperature, the ligands desorb which cause a dielectric environment change. As a consequence, the LSPR peak shifts. This phenomenon is well studied in wavelength shift LSPR sensing and can be quantitatively expressed as:[1]

$$\Delta\lambda_{\max} = m\Delta n\left[1-\exp\left(\frac{-2N}{l_d}\right)\right] \tag{2.6}$$

where $\Delta\lambda_{\max}$ is the shift in LSPR peak maximum, m is the bulk refractive-index response of the nanoparticles; Δn is the change in refractive index induced by the adsorbate; N is the number of effective adsorbate; and l_d is the characteristic EM-field-decay length. Linearize equation (2.6):

$$-N \propto \ln\left(1-\frac{\Delta\lambda_{\max}}{m\Delta n}\right) \tag{2.7}$$

As shown in Figure 2.6, the integration of C-H stretch has a linear correlation with the LSPR shift term $\ln\left(1-\frac{\Delta\lambda_{\max}}{m\Delta n}\right)$ which validates of Beer-Lambert law and confirms that the peak intensity can represents the quantities of surface adsorbates.

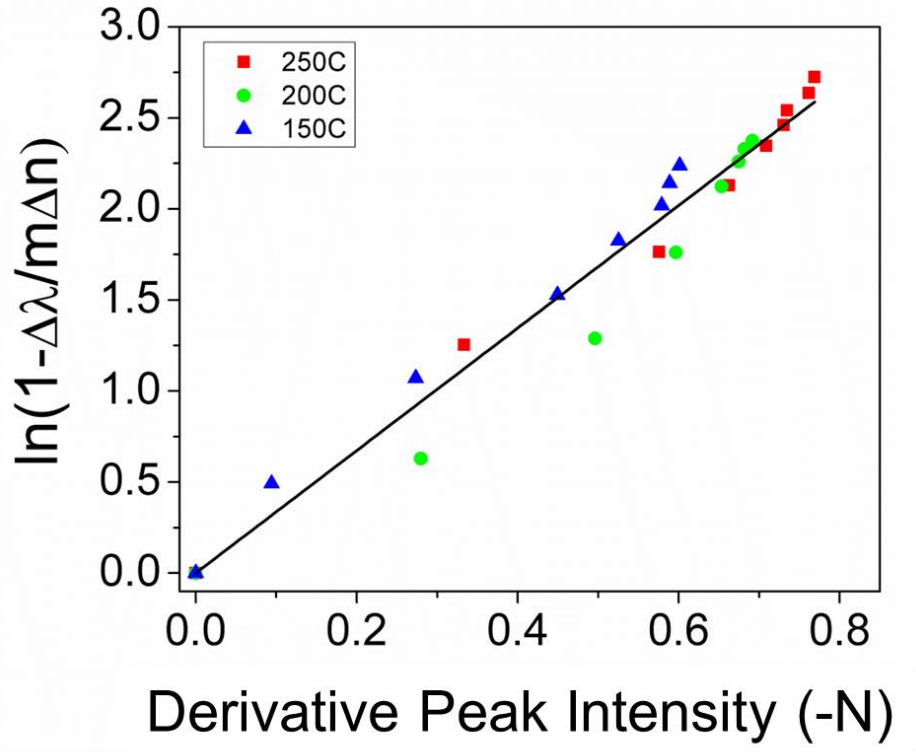

Figure 2.6. The validation of Beer-Lambert law: the linear correlation between derivative C-H peak intensity (-N) and the LSPR shift term $\ln\left(1-\frac{\Delta\lambda_{max}}{m\Delta n}\right)$ in ligand removal experiment.

2.3.3 Morphology analysis

Nanocrystal morphology is characterized with a suite of techniques, including scanning electron microscopy (SEM, Zeiss Ultra 60 FE), transmission electron microscopy, Hitachi HD-2700 and Fecnai F30). For SEM imaging, nanocrystals are spin-cast onto a Si substrate and then UV-ozone for 30 minutes to remove hydrocarbon ligands. For nanocrystal film cross-section image, cleaned sample is gently cleaved in the center using a diamond scriber and mounted onto SEM stubs using carbon tape. For TEM imaging, nanocrystals are drop-cast onto lacey carbon grids (Ted Pella).

The crystal structure of synthesized metal oxide is characterized using X-ray diffraction (XRD, Panalytical Empyrean and X' Pert PRO Alpha-1). The result pattern is compared with standard JCPDS database to confirm the crystal structure.

2.3.4 Elemental analysis

The nanocrystal composition is characterized using X-ray photoelectron spectroscopy (XPS, Thermo K-Alpha) and inductively coupled plasma atomic emission spectrometer (ICP-AES, Perkin Elmer Optima 3000 DV).

CHAPTER 3

REVERSIBLE TUNING OF THE SURFACE PLASMON RESONANCE OF INDIUM TIN OXIDE NANOCRYSTALS BY GAS-PHASE OXIDATION AND REDUCTION

3.1 Overview

In this chapter, we demonstrate a reversible modulation of LSPRs of tin-doped indium oxide by gas-phase reaction. Nanocrystal carrier density, and thus spectral response, is adjustable via chemical reaction; however, the fundamental processes that govern this behavior are poorly understood. Here, we study the time- and temperature-dependence of the LSPRs supported by ITO nanocrystals during O_2 and N_2 annealing with *in situ* reflectance infrared Fourier transform spectroscopy (DRIFTS). We show that LSPRs redshifts upon oxidation in O_2 and blueshifts to its original position upon reduction in N_2. A reaction-diffusion model is developed to understand the underlying mechanism and reveals an interplay between surface reaction, oxygen interstitial diffusion, and tin-oxygen complex formation determines the dynamics of this process. These findings provide a foundation from which to rationally program plasmonic nanocrystal structure for a desired spectral response.

3.2 Introduction

The strong light-matter interactions of LSPRs have attracted attention as a route to capture solar radiation,[66-69] improve sensitivity of spectroscopy,[9, 70-71] and promote chemical reactions.[20-22, 72-73] Doped metal oxide nanocrystals, due to the ease of tuning carrier density, are emerging as a versatile platform with which to manipulate LSPRs throughout the infrared.[37, 41, 51,

[74-78] Sn-doped indium oxide, also known as ITO, is particularly intriguing due to the simplicity of synthesizing nanocrystals,[50, 53] its broadly adjustable LSPR,[78] and its chemical stability under ambient conditions.[49-50, 53] The LSPR supported by ITO nanocrystals is controllable by aliovalent doping (i.e., changes in Sn concentration) during synthesis, in addition to post-synthetic photo[63] and electrochemical doping.[59] While these methods are usually carried out in solution; there are situations where nanocrystal powders and gas phase modulation of spectral response are desirable. Simple air annealing of ITO nanocrystals causes a substantial redshift of the LSPR in ITO nanocrystals.[59, 78] However, there is little understanding of the physicochemistry that underlies this process. More generally, establishing a connection between the redox chemistry, carrier density, and the LSPR of metal oxide nanocrystals, of ITO or other materials, in gas phase environments would provide a foundation from which to engineer plasmonic response for a host of new applications.

The connection between redox chemistry and carrier density is well established in bulk and thin film ITO.[55, 79-81] In_2O_3 exhibits a cubic bixbyite structure where one fourth of the lattice sites are vacant. For intrinsic In_2O_3, oxygen vacancies yield a carrier density on the order of 10^{19} cm^{-3},[79, 82] which is insufficient to support a mid-infrared LSPR (>500 cm^{-1}).[63] On the other hand, aliovalent substitution of In^{3+} by Sn^{4+} yields ITO and a concomitant increase in carrier density to ~10^{21} cm^{-3}.[83] The aliovalent doping of Sn dominates the free carriers as it contributes to two orders of magnitude higher of carrier density compared to oxygen vacancies. Oxidation can reduce carrier density via the formation of neutral tin-oxygen $\left(2Sn_{In}^{\bullet} - O_i^{''}\right)$ complexes, where oxygen atoms occupy vacancy sites and trap two free electrons. The concentration of $\left(2Sn_{In}^{\bullet} - O_i^{''}\right)$ depends on O_2 partial pressure and tin content.[55] Alternatively, the carrier density of thin films is also known to increase in reductive environments.[80-81]

Here, we investigate the oxidation and reduction of plasmonic ITO nanocrystals. Time-resolved extinction spectra are collected with *in situ* diffuse reflectance infrared Fourier transform spectroscopy (DRIFTS) as a function of gaseous species (O_2 or N_2) and temperature. We identify conditions that permit ITO nanocrystal spectral response to be reversibly modulated. A reaction-diffusion model, developed to understand the dynamics of this process, supports an interplay between surface reaction, oxygen interstitial diffusion, and tin-oxygen complex formation.

3.3 Experimental Details

Dispersions of ITO nanocrystals are synthesized according to a previously reported protocol.[59] A solution containing 0.5 mmol $In(acac)_3$ (Sigma-Aldrich, 99.99%) and 0.043 mmol tin $Sn(acac)_2Cl_2$ (Sigma-Aldrich, 98%) in 7g of OA (Sigma-Aldrich, 70%) is mixed in a 50 mL two-necked flask and connected to a Schlenk line. The reaction is carried out at 250 °C for 5 hours under N_2 flow. The resulting reaction mixture is precipitated by adding 20 mL ethanol followed by centrifugation at 3000 rpm for 10 minutes, after which the supernatant is removed. The ITO nanocrystals are cleaned by two cycles of redispersion in hexane (BDH, 98.5%), reprecipitation with ethanol, and centrifugation. During redispersion, 20 μL oleylamine and 40 μL oleic acid (Sigma-Aldrich, 90%) are added to stabilize the nanocrystal dispersion. Nanocrystal structure is characterized with a suite of techniques, including X-ray photoelectron spectroscopy (XPS, Thermo K-Alpha), X-ray diffraction (XRD, Panalytical Empyrean), and (scanning) transmission electron microscopy ((S)TEM, Hitachi HD-2700 and FEI Tecnai F30). Nanocrystals are deposited onto lacey carbon grids for TEM measurement. As-synthesized ITO nanocrystals exhibit an average diameter of 9.4 ± 1.7 nm, as shown in Figure 3.1(a). The

morphologies are consistent with literature reports for this synthesis.[50, 53] The Sn composition of these nanocrystals, as approximately determined via XPS, is 11.5 atom%.

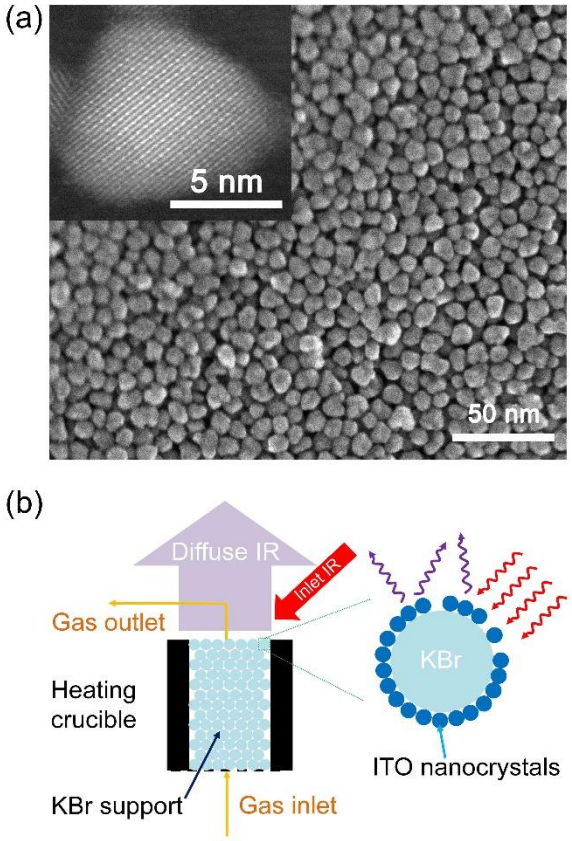

Figure 3.1. (a) Representative secondary electron image of synthesized ITO nanocrystals. Inset: High resolution STEM image of an individual ITO nanocrystal along the [0-11] zone axis, (b) Schematic illustration of the *in situ* DRIFTS measurement.

Time-resolved DRIFTS measurements are accomplished in a diffuse reflectance accessory (Harrick Scientific Products, Praying Mantis) coupled to a Fourier transform infrared spectrometer (Bruker, Vertex 70) equipped with a CaF_2 beam splitter and a liquid nitrogen-cooled HgCdTe detector. The DRIFTS measurement geometry is schematically illustrated in Figure 3.1(b). The diffuse reflectance accessory, in addition to mirrors that direct the incident infrared beam onto the sample and collect the diffusely scattered light, contains a reaction

chamber with a crucible where the ITO nanocrystals are placed. The top dome of the reaction chamber contains ZnSe windows to enable infrared light input and output. The combination of a rotary vane pump (Edwards, RV12) and o-ring seals enables reaction chamber base pressure of 5 mTorr. Prior to each experiment, the crucible is first filled with KBr powder (Sigma-Aldrich, > 99%), 30 μL of ITO nanocrystal solution is then drop-cast on top, the solvent is allowed to evaporate, and the reaction chamber is evacuated. The flow rates of O_2 (Airgas, 99.999%) and N_2 (Airgas, 99.999%), which are controlled with mass flow controllers (MKS Instruments, 1479A), are 72 sccm for all experiments. Total chamber pressure is 4.5 Torr. Two pre-treatment cycles, each consisting of 30 minutes of O_2 and 50 minutes of N_2 annealing at 300 °C, are conducted to remove the surface ligands, as confirmed via DRIFTS (not shown). All DRIFTS spectra are collected with unpolarized light and a spectrometer resolution of 4 cm^{-1}. Each spectrum consists of 64 scans and fresh KBr powder is used as a reference. Peak positions are extracted using GaussianAmp, Origin's built-in peak analyzing function.

The simulation and parameter estimation are carried out using gPROMS ModelBuilder 4.0.0. Discretization is accomplished with the second order orthogonal collocation on finite element method (OCFEM), which is known to be effective for problems involving both reaction and diffusion.[84-85] Acceptable computational time and accuracy are achieved with 2000 nodes. The parameter estimation problem is formulated as a nonlinear programming (NLP) problem, which is then solved with the sequential quadratic programming (SQP) solver in gPROMS. In the SQP technique, the full problem is approximated as a quadratic problem and the solution to this sub-problem are used to construct a better approximation and, over many iterations, a more optimal solution.[86]

3.4 Results and Discussion

As shown in Figure 3.2(a), ITO nanocrystals exhibit a LSPR near 5200 cm^{-1} (0.65 eV) after dispersion, drying, and ligand removal on KBr powder (i.e., t = 0 minutes). The LSPR redshifts to approximately 4300 cm^{-1} (0.53 eV) upon O_2 exposure at 300 °C for 30 minutes. We note that the original and final LSPR peak position varies by ±50 cm^{-1} between experiments, an effect we attribute to subtle changes in nanocrystal packing when filling the DRIFTS crucible. The absorption features between 5000 and 5500 cm^{-1} as well as below 4000 cm^{-1} are absorptions due to water vapor present in the air outside of the reaction chamber. LSPR peak position normalized to its value at t = 0 minutes (i.e., 5200 cm^{-1}) is plotted in Figure 3.2(b) as a function of time for oxidation at 250, 300, and 350 °C. For all temperatures, a rapid redshift occurs at short times before plateauing at long times. The magnitude of the redshift is proportional to oxidation temperature, with 250, 300, 350 °C yielding final LSPRs at ~4500, 4300 and 3900 cm^{-1}.

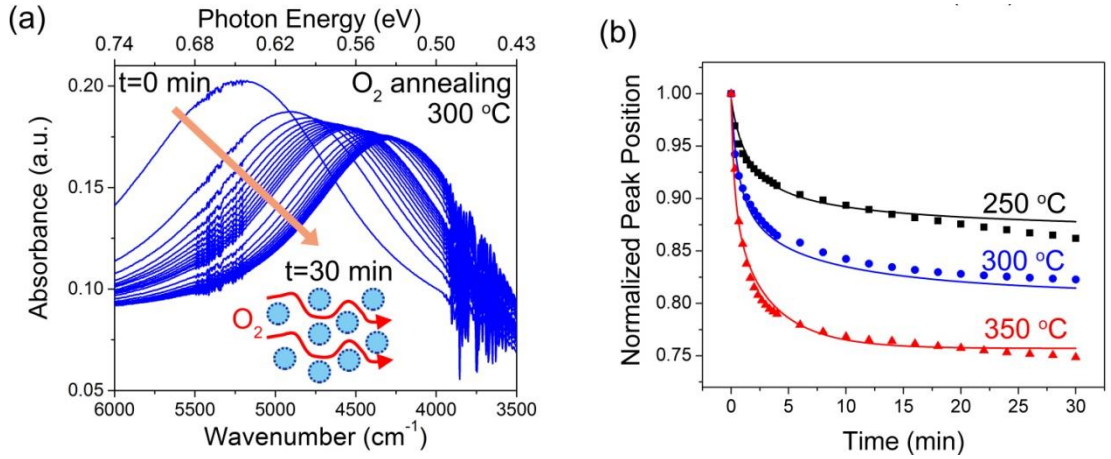

Figure 3.2. (a) Absorption spectra as a function of time during O_2 annealing at 300 °C; (b) Peak position as a function of time for O_2 annealing at 250 (black squares), 300 (blue circles), and 350 (red triangles) °C. Peak positions are normalized relative to the value prior to O_2 annealing (i.e., at t = 0 minutes). Points are experimental data and lines are model fits.

An inverse process occurs upon annealing ITO nanocrystals in a N_2 environment. Figure 3.3(a) shows that the LSPR blueshifts back to its original position at 300 °C. Figure 3(b) shows that the same behavior occurs for N_2 annealing at 350 °C; however, annealing at 250 °C results in a far more modest blueshift. The time required for the LSPR to blueshift to its original energy is ~50 minutes whereas the time required to fully redshift is only ~30 minutes. Analogously to the redshift observed upon O_2 annealing, the blueshift seen at 300 and 350 °C initially occurs rapidly and then plateaus. Notably, vacuum annealing at 300 °C (not shown) leads to a similar blueshift

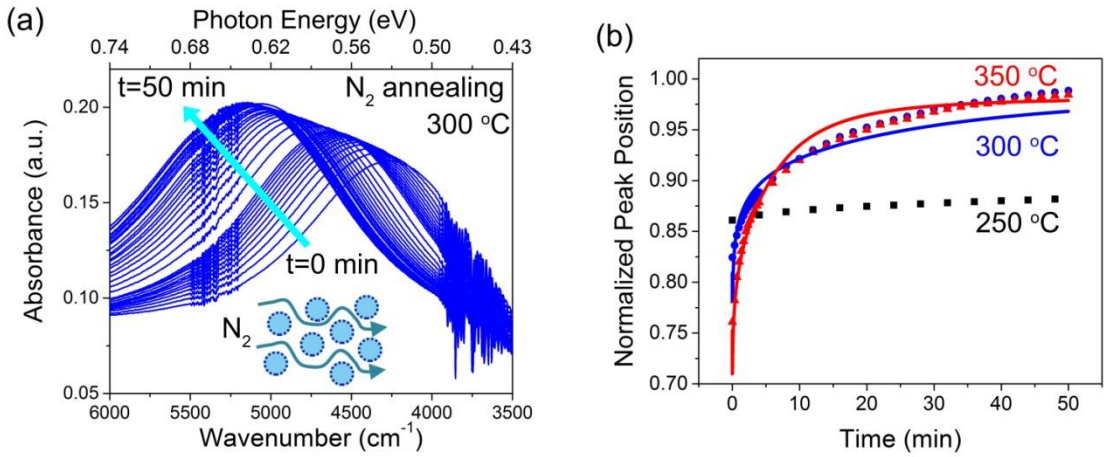

Figure 3.3. (a) Absorption spectra as a function of time during N_2 annealing at 300 °C; (b) Peak position as a function of time for N_2 annealing at 250 (black squares), 300 (blue circles), and 350 (red triangles) °C. Peak positions are normalized relative to their value prior to O_2 annealing. Points are experimental data and lines are model fits.

The data in Figures 3.2 and 3.3, in conjunction with the known defect chemistry of ITO thin films,[80-81] indicate a mechanism of O_2- and N_2-induced ITO nanocrystal oxidation and reduction, respectively. Such a mechanism is supported by the high resolution TEM images in

Figure 3.4(a) and the XRD patterns in Figure 3.4(b), which do not reveal obvious structural transformations after either O_2 or N_2 annealing that could account for observed spectral changes. The nanocrystals remain single-crystalline with clearly observable boundaries, indicating that sintering, if any, is minimal.

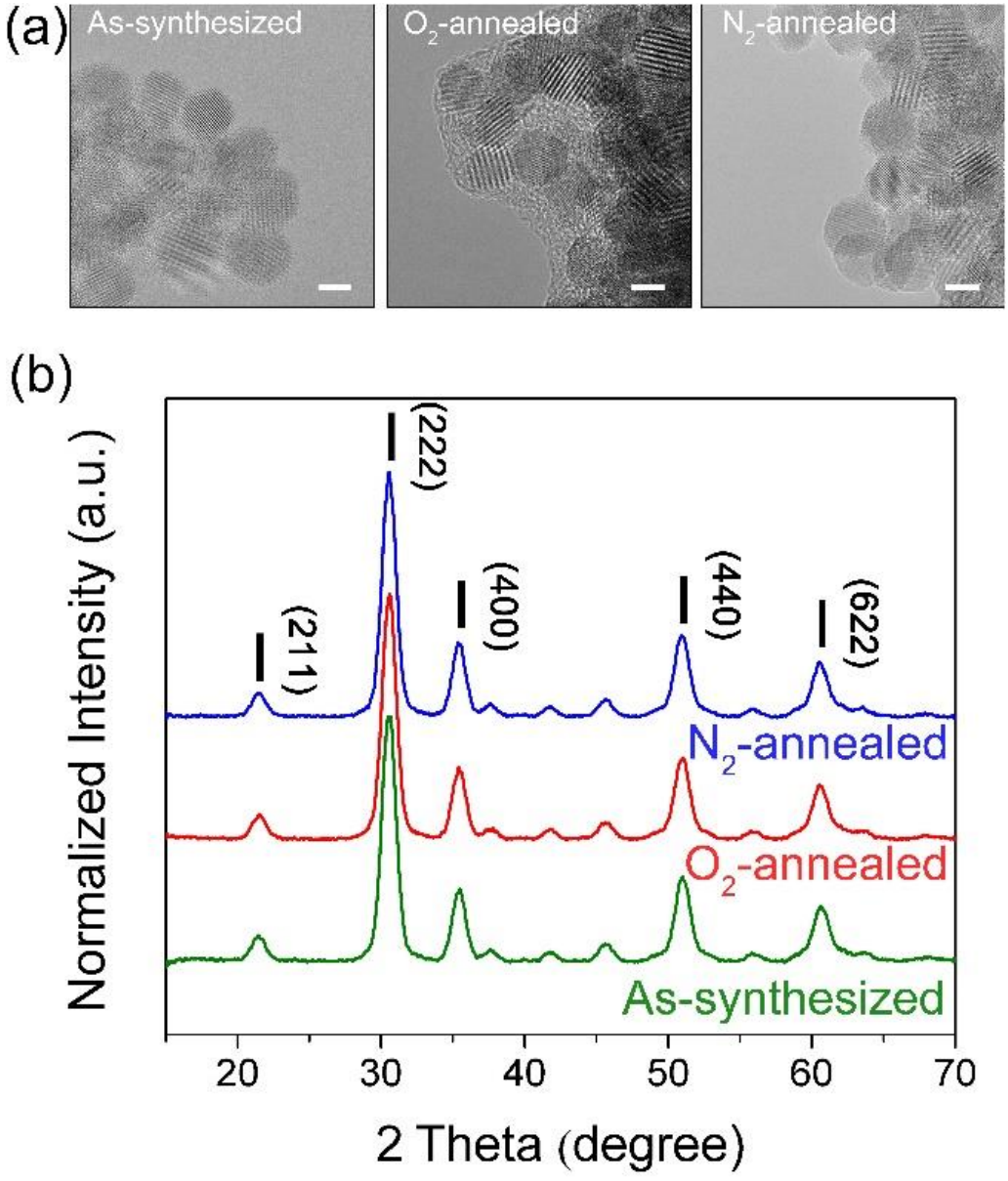

Figure 3.4. (a) TEM images of as-synthesized, O_2-annealed, and N_2- annealed ITO nanocrystals. Scale bars, 5 nm. (b) XRD spectra of as-synthesized, O_2-annealed, and N_2- annealed ITO nanocrystals.

The d-spacing, as determined from the selected area electron diffraction (SAED) patterns, both before and after annealing are consistent with standard values for ITO as well. (**Figure 3.5** and **Table 3.1**).

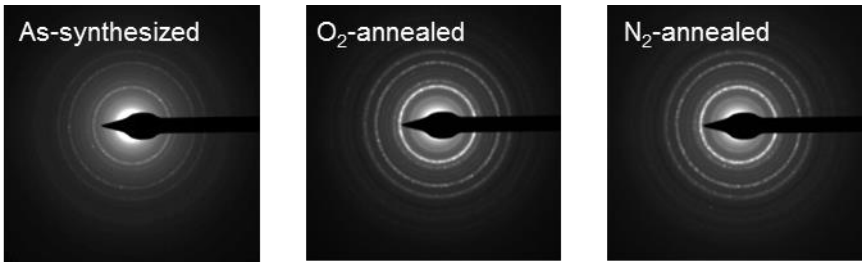

Figure 3.5. SAED patterns of as-synthesized, O_2-annealed, and N_2-annealed ITO nanocrystals.

Table 3.1. d-spacing of ITO standard (JCPDS card no. 71-2194) as well as as-synthesized, O_2-annealed, and N_2-annealed ITO nanocrystals.

	Standard	As-synthesized	O_2-annealed	N_2-annealed
Planes	d-space (Å)	d-space (Å)	d-space (Å)	d-space (Å)
211	4.13	4.12	4.20	4.20
222	2.92	2.94	2.99	2.94
400	2.53	2.54	2.59	2.57
411	2.38	2.18	2.20	2.21
431	1.98	2.00	2.00	1.99
521	1.85	1.80	1.84	1.82
622	1.53	1.53	1.54	1.54

We propose an oxidation/reduction mechanism to explain the observed LSPR optical response and construct a reaction-diffusion model to quantify it. More specifically, O_2 decomposition on the ITO nanocrystal surface delivers interstitial oxygen atoms that diffuse into the "bulk" and form tin-oxygen complexes. These complexes reduce the carrier density and

cause the observed redshift of the LSPR. The observed blueshift results from the reverse of this process.[55, 81] Models that consider only surface reaction or assume rapid oxygen interstitial diffusion are insufficient to describe our experimental data.

Several assumptions are made to simplify our reaction-diffusion model. First, we assume that substitutional Sn atoms, not oxygen vacancies, provide the majority of charge carriers in heavily-doped ITO.[79, 81] Second, as supported by the large formation energy for Sn point defects,[87] we assume substitutional Sn atoms are fixed in the lattice. Only interstitial oxygen atoms can diffuse. Finally, we assume spherical nanocrystals since geometry only modifies reaction-diffusion models by a constant of order unity.[88]

The mass balances for interstitial oxygen and substitutional tin, respectively, can be expressed as:

$$\frac{d\left[O_i''\right]}{dt} = \frac{1}{r^2}\frac{d}{dr}\left(r^2 D_{eff}\frac{d\left[O_i''\right]}{dr}\right) - R_f + R_r \tag{3.1}$$

$$\frac{d\left[Sn_{In}^{\bullet}\right]}{dt} = -2R_f + 2R_r \tag{3.2}$$

where $\left[O_i''\right]$ is the excess interstitial oxygen concentration, $\left[Sn_{In}^{\bullet}\right]$ is the substitutional tin concentration, $\left[2Sn_{In}^{\bullet} - O_i''\right]$ is the tin-oxygen complex concentration, R_f and R_r are the forward and reverse reaction rates for tin-oxygen complex formation, respectively, D_{eff} is the effective diffusion coefficient, and r is the distance from the nanocrystal's center. No diffusion term is included for substitutional Sn as it is assumed immobile in the lattice (*vide supra*).

The tin-oxygen complex forms via reaction of two substitutional Sn atoms, an interstitial oxygen atom, and two electrons:

$$2Sn_{In}^{\bullet} + O_i^{''} + 2e^{-} \underset{k_r}{\overset{k_f}{\rightleftarrows}} \left(2Sn_{In}^{\bullet} - O_i^{''}\right) \quad \text{(Reaction 1)}$$

If the reaction is assumed elementary, then the forward and reverse reaction rates can be expressed as:

$$R_f = k_f \left[Sn_{In}^{\bullet}\right]^2 \left[O_i^{''}\right] \tag{3.3}$$

$$R_r = k_r \left[2Sn_{In}^{\bullet} - O_i^{''}\right] \tag{3.4}$$

By substituting equations (3.3) and (3.4) into equations (3.1) and (3.2), the mass balances become:

$$\frac{d\left[O_i^{''}\right]}{dt} = \frac{1}{r^2}\frac{d}{dr}\left(r^2 D_{eff}\frac{d\left[O_i^{''}\right]}{dr}\right) - k_f \left[Sn_{In}^{\bullet}\right]^2 \left[O_i^{''}\right] + k_r \left[2Sn_{In}^{\bullet} - O_i^{''}\right] \tag{3.5}$$

$$\frac{d\left[Sn_{In}^{\bullet}\right]}{dt} = -2k_f \left[Sn_{In}^{\bullet}\right]^2 \left[O_i^{''}\right] + 2k_r \left[2Sn_{In}^{\bullet} - O_i^{''}\right] \tag{3.6}$$

We define dimensionless concentrations and a dimensionless radial length scale as:

$$\overline{\left[Sn_{In}^{\bullet}\right]} = \frac{\left[Sn_{In}^{\bullet}\right]}{\left[Sn_{In}^{\bullet}\right]^{Initial}} \tag{3.7}$$

$$\overline{\left[O_i^{''}\right]} = \frac{\left[O_i^{''}\right]}{\left[Sn_{In}^{\bullet}\right]^{Initial}} \tag{3.8}$$

$$\overline{\left[2Sn_{In}^{\bullet} - O_i^{''}\right]} = \frac{\left[2Sn_{In}^{\bullet} - O_i^{''}\right]}{\left[Sn_{In}^{\bullet}\right]^{Initial}} \tag{3.9}$$

$$\bar{r} = \frac{r}{R} \tag{3.10}$$

where $\left[Sn_{In}^{\bullet}\right]^{Initial}$ and R are the initial substitutional Sn concentration and nanocrystal radius, respectively. Substituting these quantities into equations (3.5) and (3.6), as well as expanding the Arrhenius dependence of the rate constants and diffusivity, yields:

$$\frac{d\overline{\left[O_i^{"}\right]}}{dt}=\frac{D_0 e^{\frac{Ea_{diff}}{RT}}}{R^2}\frac{1}{\bar{r}^{-2}}\frac{d}{d\bar{r}}\left(\bar{r}^{-2}\frac{d\overline{\left[O_i^{"}\right]}}{d\bar{r}}\right)-k_f^{'}\overline{\left[Sn_{In}^{\bullet}\right]}^2\overline{\left[O_i^{"}\right]}+k_r^{'}\overline{\left[2Sn_{In}^{\bullet}-O_i^{"}\right]} \tag{3.11}$$

$$\frac{d\overline{\left[Sn_{In}^{\bullet}\right]}}{dt}=-2k_f^{'}\left(\left[Sn_{In}^{\bullet}\right]^{Initial}\right)^2\overline{\left[Sn_{In}^{\bullet}\right]}^2\overline{\left[O_i^{"}\right]}+2k_r^{'}\overline{\left[2Sn_{In}^{\bullet}-O_i^{"}\right]} \tag{3.12}$$

with the following effective rate constants:

$$k_f^{'}=k_{fr\_0}e^{\frac{Ea_f}{RT}}\left(\left[Sn_{In}^{\bullet}\right]^{Initial}\right)^2 \tag{3.13}$$

$$k_r^{'}=k_{rr\_0} \tag{3.14}$$

The boundary conditions emerge as follows. Oxygen atoms are delivered to and removed from the nanocrystal through its outer surface. Thus, the boundary condition at the surface for $O_i^{"}$ and $Sn_{In}^{\bullet}$ are:

$$\left[O_i^{"}\right]\left(\bar{r}=1\right)=\left[O^{"}\right](t) \tag{3.15}$$

$$\frac{d\left[Sn_{In}^{\bullet}\right]}{d\bar{r}}\left(\bar{r}=1\right)=0 \tag{3.16}$$

To determine $\left[O^{"}\right](t)$, we assume the simplest absorption model, in which one oxygen molecule absorbs on the surface and dissociates into two oxygen atoms on a single surface site:

$$O_2\left(gas\right)\underset{k_1^{'}}{\overset{k_1}{\rightleftarrows}}O_2^{*} \qquad \text{(Reaction 2)}$$

$$O_2^{*}\underset{k_2^{'}}{\overset{k_2}{\rightleftarrows}}2O^{"} \qquad \text{(Reaction 3)}$$

The mass balance for each oxygen species is:

$$\frac{d\left[O_2\right]}{dt}=-k_1P_{O_2}+k_1^{'}\left[O_2^{*}\right] \tag{3.17}$$

$$\frac{d\left[O_2^*\right]}{dt} = k_1 P_{O_2} - k_1^{'}\left[O_2^*\right] - k_2\left[O_2^*\right] + k_2^{'}\left[O^{''}\right]^2 \tag{3.18}$$

$$\frac{d\left[O^{''}\right]}{dt} = 2k_2\left[O_2^*\right] - 2k_2^{'}\left[O^{''}\right]^2 \tag{3.19}$$

Applying the pseudo steady-state approximation on the intermediate, O_2^*, yields the following differential equation for $O^{''}$:

$$\frac{d\left[O^{''}\right]}{dt} = \frac{2k_1k_2}{k_1^{'}+k_2} P_{O_2} + \left(\frac{2k_2k_2^{'}}{k_1^{'}+k_2} - 2k_2^{'}\right)\left[O^{''}\right]^2 \tag{3.20}$$

By defining $k_{sf} = \frac{2k_1k_2}{k_1^{'}+k_2}$ and $k_{sr} = \frac{2k_2k_2^{'}}{k_1^{'}+k_2} - 2k_2^{'}$ and expanding the Arrhenius dependence of the rate constants, equation (3.11) simplifies to:

$$\begin{aligned}\frac{d\left[O^{''}\right]}{dt} &= k_{sf} P_{O_2} + k_{sr}\left[O^{''}\right]^2 \\ &= k_{sf}^{'} e^{\frac{Ea_{sf}}{RT}} P_{O_2} + k_{sr}^{'} e^{\frac{Ea_{sr}}{RT}}\left[O^{''}\right]^2\end{aligned} \tag{3.21}$$

and is used in equation (3.15) above. At the center of the nanocrystal, the concentration gradient is zero due to the symmetry:

$$\frac{d\left[O_i^{''}\right]}{d\bar{r}}\left(\bar{r}=0\right) = 0 \tag{3.22}$$

$$\frac{d\left[Sn_{In}^{\bullet}\right]}{d\bar{r}}\left(\bar{r}=0\right) = 0 \tag{3.23}$$

We also allow the substitutional Sn composition to be radially-dependent, which has been shown for the ITO nanocrystal synthesis method used here.[83] A sigmoid function is used to simulate the doping profile and we note that poor model fits result in the absence of this dependence.

The connection between carrier density and the plasma frequency is introduced by:[89]

$$\omega_{sp} = \alpha\omega_p = \sqrt{\frac{Ne^2}{\varepsilon_0 m_\varepsilon}} \tag{3.24}$$

where N is the charge carrier density, e is the elementary charge, ε_0 is the permittivity of free space, and m_ε is the effective mass of an electron. Normalizing the LSPR frequency relative to its value prior to oxygen annealing (i.e., at t = 0 minutes) assuming constant m_ε gives:[90]

$$\frac{\omega_{sp}(t)}{\omega_{sp}(t=0)} = \frac{\sqrt{\frac{N(t)e^2}{\varepsilon_0 m_\varepsilon}}}{\sqrt{\frac{N(t=0)e^2}{\varepsilon_0 m_\varepsilon}}} = \sqrt{\frac{N(t)}{N(t=0)}} \tag{3.25}$$

The total carrier density in the nanocrystal is the sum of substitutional tin atoms:

$$N = \int_0^1 4\pi r^{-2} \left[Sn_{In}^{\bullet} \right] d\bar{r} \tag{3.26}$$

Finally, the governing mass balances in equations (3.11) and (3.12) are solved with the boundary conditions in equations (3.15), (3.16), (3.22) and (3.23). Values of the model parameters, for both the oxidation and reduction steps, are shown in Table 3.2.

Table 3.2. Fitted parameters for the reaction-diffusion model.

Parameter	Oxidation	Reduction
D_0 (m^2/s)	5.52×10^{-10}	7.79×10^{-10}
Ea_{diff} (kJ/mol)	103	107
Ea_f (kJ/mol)	53.0	107
Ea_r (kJ/mol)	12.0	62.0
Ea_{sf} (kJ/mol)	46.0	17.0
Ea_{sr} (kJ/mol)	49.0	12.0
k_f	4.41×10^{5}	3.52×10^{6}
k_r	1.48×10^{3}	1.56×10^{3}
k_{sf}	5.39×10^{5}	1.28×10^{5}
k_{sr}	2.31×10^{5}	

Our model successfully predicts the LSPR shift under O_2 and N_2 annealing, as seen in Figures 3.2(b) and 3.3(b). The radial concentration of each species as a function of time is shown in Figure 3.6 for 300 °C. At t = 0 minutes (i.e., prior to annealing), no excess interstitial oxygen is present. Upon introducing O_2, excess interstitial oxygen begins to accumulate in the near surface region and diffuse into the nanocrystal. Due to the high concentration of substitutional Sn near the nanocrystal surface,[83] there is a rapid decrease in $\left[Sn_{In}^{\bullet} \right]$ and increase in $\left[2Sn_{In}^{\bullet} - O_i^{''} \right]$ at short times. At longer times, $\left[Sn_{In}^{\bullet} \right]$ and $\left[2Sn_{In}^{\bullet} - O_i^{''} \right]$ do not change substantially; however, interstitial oxygen continues to diffuse into the nanocrystal. Equilibrium is eventually reached for both the surface O_2 decomposition and tin-oxygen complex formation reactions, which explains the observed plateau of the LSPR peak position in Figures 3.2(b) and 3.3(b). We note that $\left[Sn_{In}^{\bullet} \right]$ rises sharply near $\bar{r} = 0.98$ (Figure 3.6). Assuming a nanocrystal diameter of 10 nm, the thickness of this near-surface tin region is ~0.1 nm and is consistent with prior work.[83]

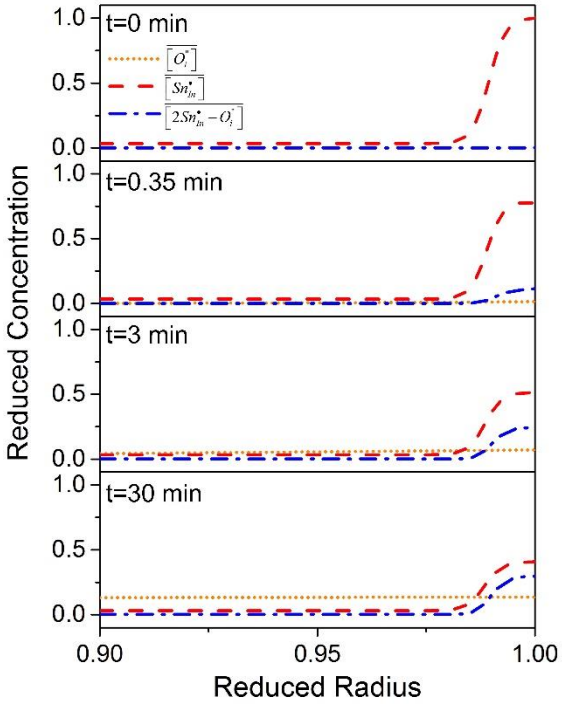

Figure 3.6. Model prediction of the reduced concentrations of interstitial oxygen, substitutional Sn, and the tin-oxygen complex as a function of reduced radius at t = 0, 0.35, 3 and 30 minutes during O_2 annealing at 300 °C.

The difference between oxidation and reduction times (i.e., 30 vs. 50 minutes) stems from oxygen concentration, and thus driving force, differences between the interior and surface of the nanocrystal. In the case of O_2 annealing, the surface oxygen atom concentration (the source) is high relative to the interior (the sink), and remains so for the duration of the process. However, for N_2 annealing, the delta between the concentration of excess interstitial oxygen in the nanocrystal interior (now the source) and surface oxygen concentration (now the sink) is not

as large as for O_2 annealing. Moreover, the interstitial oxygen concentration decreases over time, which progressively reduces the driving force, during O_2 annealing.

Our experiments show only a modest blueshift upon N_2 annealing at 250 °C. Reduced reduction capacity has been reported for thin films for annealing temperatures below 300 °C.[55] We attribute this behaviour to the strength of metal oxygen bonds.[87] Additional experiments are requried to further understand this phenomenon.

The parameters extracted for nanocrystal oxidation and reduction are consistent (Table 1), which would be expected for inverse processes. For example, the activation energy for interstitial oxygen diffusion is found to be 102 kJ/mol for nanocrystal oxidation and 106 kJ/mol for nanocrystal reduction. The pre-exponential factor for interstitial oxygen diffusion for oxidation and reduction are 5.52 $x10^{-10}$ and 7.79 $x10^{-10}$ m^2/s, respectively. While our results for ITO nanocrystals are internally consistent, there are notable differences relative to the values reported for thin films. For example, chemical vapor-deposited ITO and (undoped) In_2O_3 films exhibit activation energies for interstitial oxygen diffusion of 144 [91] and 166 kJ/mol,[92] respectively. The pre-exponential factor for interstitial oxygen diffusion in ITO and (undoped) In_2O_3 thin films are 8.1 x 10^{-4} [91] and 3.63 x 10^{-6} m^2/s,[92] respectively. Importantly, these values are determined with electrical measurements using more lightly doped materials and higher temperatures (> 700 °C) than the present study.

3.5 Conclusions

In summary, the LSPR of colloidal ITO nanocrystals can be modified post-synthetically by gas-phase annealing in O_2 and N_2. A reaction-diffusion model is proposed that includes aliovalent dopant (i.e., Sn) compensation during oxidation (in O_2) and the opposite process for

reduction (in N_2). The agreement between experiment and modelling support a mechanism whereby a combination of surface reaction, interstitial oxygen diffusion, and tin-oxygen complex formation control the dynamics of the process. This fundamental understanding provides a foundation from which to rationally program nanocrystal structure for a desired spectral response. A variety of exotic behaviors could be engineered by controlling dopant atom radial position during nanocrystal synthesis. For example, step changes to spectral response as a function of annealing time would be possible by placing substitutional Sn shells at multiple nanocrystal radii.

CHAPTER 4

DOPANT EFFECTS ON PLASMONIC PROPERTIES OF ZINC OXIDE NANOCRYSTAL

4.1 Overview

The synthesis of doped ZnO nanocrystals have been investigated in recent years, but there remains a number of unanswered questions regarding their doping profile and infrared optical properties. Here, we report a systematic comparison, of group III dopant contribution toplasmonic response of ZnO nanocrystals. We show that the quality factor of synthesized Al and Ga doped ZnO, which is 4 times higher than previous reports, is comparable to widely-used infrared plasmonic material, ITO nanocrystals. We show that Al and Ga occupy the nanocrystalcore while In occupies of shell layer, which prevents observation of an LSPR. Similar to ITO, we demonstrate that AZO and GZO nanocrystal spectral response can be reversibly modulated by O_2 and vacuum annealing at a mild temperature due to its defect chemistry.

4.2 Introduction

Mid-infrared (IR) photons, typically range from 2.5 to 20 μm, have received intense attention and are rapidly emerging as powerful tools for various applications, including catalysis[93-96], spectroscopy[30, 97] and energy conversion.[98] As it overlaps with the fingerprint window, the light-mater interaction in this region is essential for infrared spectroscopy.[30, 97] By selectively depositing infrared photon energies into vibrational mode of key reagents, many studies have demonstrated the capability to modify reaction pathways which opens the window for photon-assisted selective chemistry.[93-96] However, due to the nature of the mid-infrared

photons possessing low energy, as well as absorption cross-section of molecules being small, it is still difficult to apply mid-infrared photons in large-scale energy fields.

Localized surface plasmons resonances – the collective oscillation of charge carriers sustained by small particles – have recently gained prominence due to their large absorption cross-sections and ability to confine light into deep subwavelength volumes. Conventionally, noble metal nanostructures, specifically colloidal gold and silver, have been demonstrated to show LSPR in the visible range.[89] However, colloidal gold and silver cannot support a LSPR within IR ranges because their carrier densities are too large ($\sim 10^{23}$ cm^{-3}) and difficult to change appreciably. In addition, gold and silver have high losses in the visible and near-IR ranges and very large negative real permittivity values.[99] As an alternative to gold and silver, the heavily doped semiconductors allow for tuning of LSPR in near-IR to mid-IR range by varying the doping concentration which can exhibit both a small negative real permittivity and relatively small losses in the near-IR.[41, 49, 51, 59, 100] Transparent conductive oxides (TCOs) can be doped much higher than many other semiconductors (such as silicon) which gives them metal-like optical properties in the near and mid-IR. The list of potential plasmonic TCO materials has expanded to doped niobium oxide,[101] tungsten oxide,[47] cadmium oxide,[48] indium oxide[49-50] and zinc oxide.[51] Among them, Sn-doped indium oxide (ITO) attracts most attention due to its broadly adjustable LSPR, and its chemical stability under ambient conditions. However, limited by the cost and natural reserves of indium, researchers show interest in doped zinc oxide (ZnO) for large-scale applications. Compared to ITO, ZnO is a nontoxic, inexpensive, earth abundant material and it can support LSPR in mid-infrared owing to the increased free carrier concentration when highly doped with trivalent cations, like Al^{3+}.Consequently, doped ZnO is

one of the most attractive and significant plasmonic materials for applications in infrared due to its abundance, SPR peaks in the infrared, and remaining transparent in the visible range.

Preparation of plasmonic nanoparticles with uniformity in composition, size, shape, internal structure, and surface chemistry is essential for infrared plasmonic properties. Among many reports about preparation of ZnO, colloidal synthesis method with high temperature solution phase provides a method of showing an opportunity to control and tune the size, shape, doping ratio, and localized surface plasmon resonances.[51, 102] The first demonstration of plasmonic properties in ZnO is introduced by Al doped ZnO (AZO) synthesized using hot injection method. By varying the growth temperature and precursor amount, the LSPR energies can be varied between 2000 cm^{-1} to 3000 cm^{-1}. Following this paper, the synthesis of indium[103] and gallium[104]-doped ZnO nanocrystals use the same synthesis method. Detailed physical properties and morphology are studied for these materials, but no well-defined LSPR properties are shown. More recently, a non-injection synthesis of ZnO nanocrystals doped with Al, Ga and In has been demonstrated to be amenable to high precursor concentration and high reaction yields.[52] But due to the large particle distribution of this technique, the quality factor is relatively low compared to other doped metal oxide nanocrystals. Thus, a confirmation that if doped ZnO can support low-loss LSPR comparable to ITO in infrared is necessary.

Here, a systematic comparison, of group III dopant effect on the LSPR of ZnO nanocrystals film is reported. We synthesize aluminum doped ZnO (AZO), gallium doped ZnO (GZO), and indium doped ZnO (IZO) nanocrystals with varying doping concentration and investigate the resulting optical properties. Combining the etching and XPS data, the doping profile in the nanoparticles are revealed. In addition, we investigate the thermal stability with vacuum and oxidation annealing of plasmonic AZO and GZO nanocrystals. Time-resolved

extinction spectra are collected with *in situ* diffuse reflectance infrared Fourier transform spectroscopy (DRIFTS) as a function of gaseous species (O_2) and temperature. We identify conditions that permit AZO and GZO nanocrystal spectral response to be reversibly modulated by gas phase reactions.

4.3 Experimental Details

All chemicals have been used without further purification. Zinc stearate ($Zn(St)_2$, 65%), aluminum acetylacetonate ($Al(acac)_3$, 99%), gallium acetylacetonate ($Ga(acac)_3$, 99.99%), indium acetylacetonate ($In(acac)_3$, 99.99%), oleic acid (OA, 90%), and 1-octadecene (ODE, 90%) are supplied by Sigma-Aldrich. 1,2-hexadecanediol (HDDIOL, ≥90%) are supplied by Santa Cruz Biotechnology. Hexane (98.5%) are purchased from BDH.

Nanocrystal structure is characterized with a suite of techniques, including X-ray diffraction (XRD, X' Pert PRO Alpha-1), transmission electron microscopy ((S)TEM, Hitachi HD-2700), and scanning electron microscopy (SEM, Zeiss Ultra 60 FE). Nanoparticles are deposited onto carbon grids for TEM measurement. Inductively coupled plasma atomic emission spectrometer (ICP-AES, Perkin Elmer Optima 3000 DV) and X-ray photoelectron spectroscopy (XPS, Thermo K-Alpha) are used to evaluate dopants contents of the doped ZnO nanocrystals.

4.3.1 Preparation of doped zinc oxide

The synthesis of colloidal doped zinc oxide nanocrystals is based on slight modifications of previous reports[51] and carried out under an N_2 atmosphere using standard Schlenk-line techniques. Briefly, in a 20 mL of glass vial, a precursor solution A containing $Zn(St)_2$ (1 mmol), $Al(acac)_3$ (0.1, 0.2, and 0.3 mmol), or $Ga(acac)_3$ (0.1, 0.2, and 0.3 mmol) or $In(acac)_3$ (0.05, 0.2, and 0.5 mmol) and OA (3 mmol) in 4 ml of ODE is magnetically stirred at 140 °C for 1 h. In a

separate 50 mL of three-neck flask, solution B containing 10 mmol of HDDIOL in 11 mL of ODE is magnetically stirred and heated to 140 °C for 1 h under N_2. The precursor solution A is injected quickly into solution B using a syringe when the temperature of solution B reaches 230 °C. The reaction mixture is kept at 210 °C for 5 h for the growth of doped ZnO nanocrystals. When the reaction mixture is cooled down to room temperature, ethanol is added to the reaction mixture to precipitate the nanocrystals out of the solution. The doped ZnO nanocrystals were then collected by centrifugation (5000 rpm for 10 min). After two cycles of redispersion in hexane (2 mL) and reprecipitation by ethanol, 20-30 mg of precipitate is eventually collected and dispersed in 10 mL of hexane. The synthesized particles were then deposited in thin film formed by spin-coating on aluminum-silicon wafer and UV ozone.

4.3.2 Doped ZnO nanocrystal film preparation and IR measurements

The doped ZnO nanocrystals are spin-coat onto Al coated Si substrate for IR measurements. The substrate is prepared by depositing ~100nm Al on the silicon wafers (0.4mm, p type B doped, resistivities: 0.1- 0.3 ohm-cm) purchased from MTI using gas sputtering. 30 μL of the nanocrystal (AZO, GZO, and IZO)/hexane solution (~ 6 mg/mL) is spin-cast onto the substrate (7×7 mm^2) with a spin profile consisting of an initial 2000 rpm spin for 30 second and a 4000 rpm spin for 20 seconds. After deposition, the surface ligands are removed by UV-ozone (Hitachi, ZONETEM) for 30 min. The spin-casting and UV-ozone cleaning are repeated by another two cycles, uniform nanocrystal films, with thickness around 80 nm, are successfully prepared and then used for IR detection.

All the IR absorption data are acquired using a diffused reflectance accessory (Harrick Scientific Products, Praying Mantis) coupled to a Fourier transform infrared spectrometer (Bruker, Vertex 70) equipped with a KBr beam splitter and a liquid nitrogen-cooled HgCdTe

detector. The reflectance accessory is able to direct the incident infrared beam onto the thin nanocrystal film sample and collect the reflected light with the Al film works as the reflective mirror on substrate. The time-resolved LSPR shifting is collected with unpolarized light and a spectrometer resolution of 4 cm^{-1}. Each spectrum consists of 64 scans and a blank Al coated Si substrate is used as a reference. The gas annealing reaction is conducted in the reaction chamber backed up by a rotary vane pump (Edwards, RV12) with a base pressure of 5 mTorr. The annealing gas is delivered through a mass flow controller (MKS Instruments, 1479A) The flow rate of O_2 (Airgas, 99.999%) keeps at 45 sccm for all annealing experiments.

4.3.3 Preparation of etching doped zinc oxide samples

The etching solution is a 0.5 mM of hydrochloric acid solution (pH=4.5). All the samples (AZO, GZO, and IZO) were deposited in thin film formed by spin-coating on silicon wafer with UV ozone and immersed in etching solution for 1, 2, 3, and 5 min. The etched sample is rinsed with DI water and dried with nitrogen for SEM images and XPS measurements.

4.4 Results and Discussion

Doped ZnO nanocrystals are synthesized using hot injection method. Solution A containing metal precursors, surfactant OA and an activating agent ODE is quickly injected into solution B containing reductant HDDIOL and ODE at nucleation temperature. The reaction relies on the irreversible alcoholysis induced by nucleophile (e.g. HDDIOL for this reaction), which generates metal hydroxide species that ultimately condense to for the oxide at growth temperature accompanied by loss of water.[52, 64] For the systematic comparison of the doped ZnO with group III dopants, all experiments were done under the same condition.

As shown in Figure 4.1A, SEM images are used to compare Al-, Ga- and In-doped nanocrystal morphologies. It shows that AZO nanocrystals (0.3 mmol of Al dopant precursor) are larger in diameter which is 24.5 ± 0.7 nm, and more faceted with predominantly spherical shapes, compared to the smaller and more spherical GZO (0.3 mmol of Ga dopant precursor) and IZO (0.2 mmol of In dopant precursor) with the average sizes of 8.5 ± 0.2 and 10.8 ± 0.3 nm, respectively. High resolution TEM (Figure 4.1B) analysis of the three kinds of doped ZnO nanocrystals reveal that their lattice fringes match well with the hexagonal wurtzite phase of ZnO nanocrystals, which is confirmed by their electron diffractions.

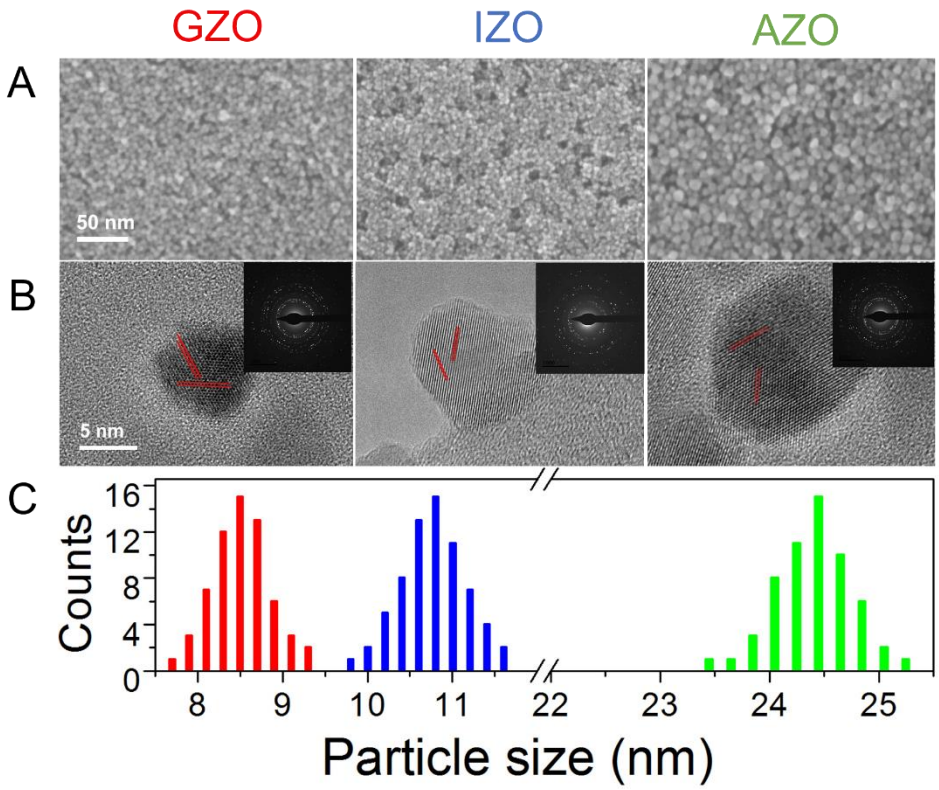

Figure 4.1. (A) SEM images of spin-cast nanocrystal films of GZO, IZO, and AZO. (B) HRTEM images of GZO, IZO, and AZO. The lattice fringes correspond to spacings of 2.47 Å and 2.81 Å which match well the *d* spacing of the (101) and (100) planes of wurtzite ZnO. The insets show the electron diffraction of GZO, IZO, and AZO with the expected wurtzite pattern.

(C) Histograms of size distribution of GZO (red), IZO (blue), and AZO (green) evaluated from SEM images.

The possible implications of the dopants on the structure of ZnO nanocrystals are probed by X-ray diffraction (XRD). As shown in the Figure 4.2, all the doped ZnO nanocrystals peaks centered at 2θ values of 31.9°, 34.6°, 36.4°, 47.8°, 56.7°, 63.1°, 66.6°, 68.2°, 69.3°, 72.8°, and 77.2°, which are indexed to (100), (002), (101), (102), (110), (103), (200), (112), (201), (004), and (202) planes. The XRD pattern shows that all synthesized doped ZnO nanocrystals possess the hexagonal wurtzite structure of ZnO phase (JCPDS No. 36-1451). No additional crystalline phases are observed regarding to other possible oxide based crystalline impurities, which implies that trivalent Al^{3+}, Ga^{3+}, In^{3+} are properly doped in the ZnO system. The present of dopant atoms in ZnO nanocrystals can be confirmed by XPS data. It is worth to note that the XRD peaks of GZO and IZO are broadened than AZO which is attributed to the variation in shape or size of nanocrystals and the lattice strain.

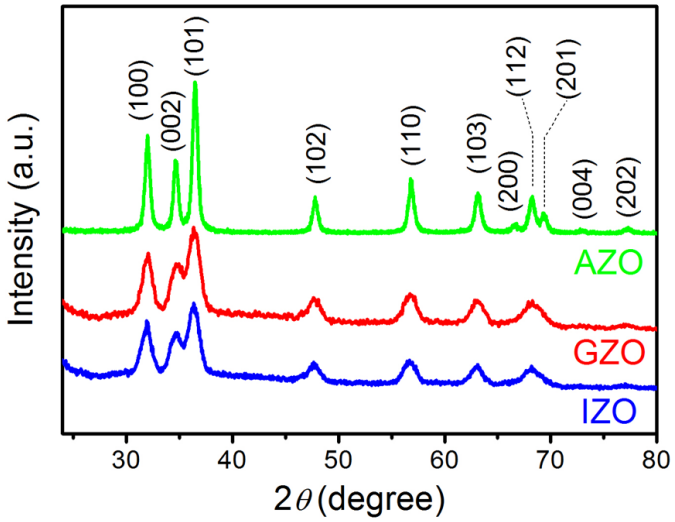

Figure 4.2. XRD patterns of the dried powders of AZO (green curve), GZO (red curve), and IZO (blue curve).

The rise of the LSPR peak centered at mid-IR (2.5-10 μm) range is clear evidence of the free electron from the extrinsic doping.[105] Using FTIR spectroscopy, the comparison of the LSPR spectra of AZO, GZO, and IZO with different doping concentrations is shown in Figure 4.3. The mid-IR plasmonic absorption peaks of AZO are measured from 2562 to 3050 cm^{-1}, as well as that of GZO from 3120 to 4011 cm^{-1}. In spite of different concentrations of In are incorporated into the zinc oxide nanocrystal, the absorbance spectrum of IZO display no obvious LSPR absorbance in the IR.

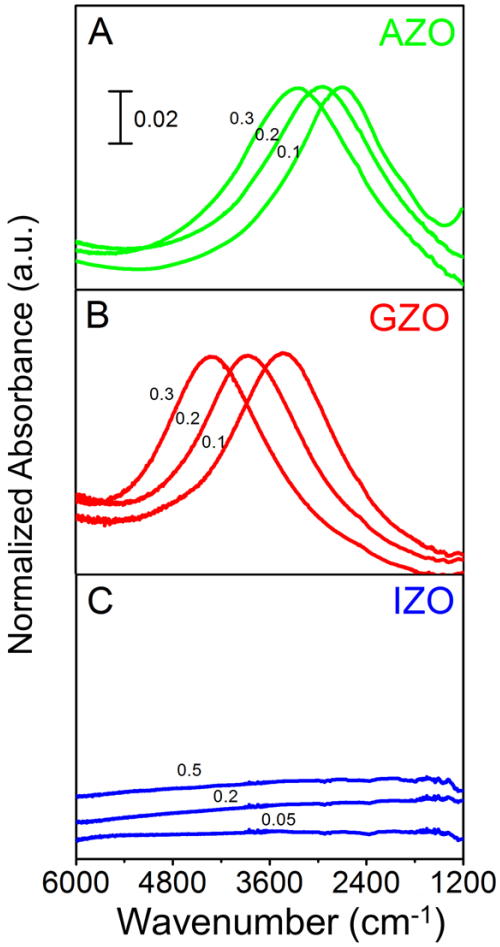

Figure 4.3. Absorption spectra of doped ZnO nanocrystals in the form with different precursor concentrations of (A) Al, (B) Ga, and (C) In.

In order to understand the absence of LSPR in IZO nanocrystals, XPS scans as function of etching time are used to compare the surface elemental composition between IZO and AZO, GZO. As shown in Figure 4.4, unlike the AZO and GZO, the intensity of In element decreases significantly with increasing etching time. In particular, the intensity of the In is reduced by half of the original intensity upon first minute of etching. This result implies that a significant amount of In dopants are present on the surface of zinc oxide nanocrystal. On the contrary, the intensity of Al and Ga elements slightly increase with the etching time increases (Figure 4.4 A and B). The results indicate that the closer is to the core, the higher is the Al and Ga doping concentration. The morphology of doped ZnO nanocrystals at each etching stage are confirmed by SEM (Figure 4.5). On average, about 1nm of ZnO on the surface is etched after 5 minutes and no destructive damage are observed after etching. The etching data implies that there is significant amount of In atoms segregate on the surface form an amorphous In_2O_3 layer which does not contribute free electrons to the conduction band of the nanoparticle. As a result, no LSPR is observed for IZO nanocrystals with this synthesis condition.

While the broad ensemble linewidths of doped metal oxide nanocrystals result from sample heterogeneity,[106] we observe relative narrow plasmon absorption peaks of AZO (Figure 4.3A) and GZO (Figure 4.3B) thin films. Previous reports on plasmonic ZnO nanocrystals show broad LSPR absorptions with quality factors less than 1.[51-52, 103-104] Here, we show that Al- and Ga-doped ZnO nanocrystals is able to hole well defined LSPR with quality factor higher than 3. The previous near-filed measurement suggests that the significant spectral inhomogeneity is primarily due to large distribution of dopant incorporation instead of size.[106] We hypothesize that by removing the capping ligands on the nanocrystals, the electron density distribution of doped ZnO nanocrystals reduces which result in narrow linewidths.

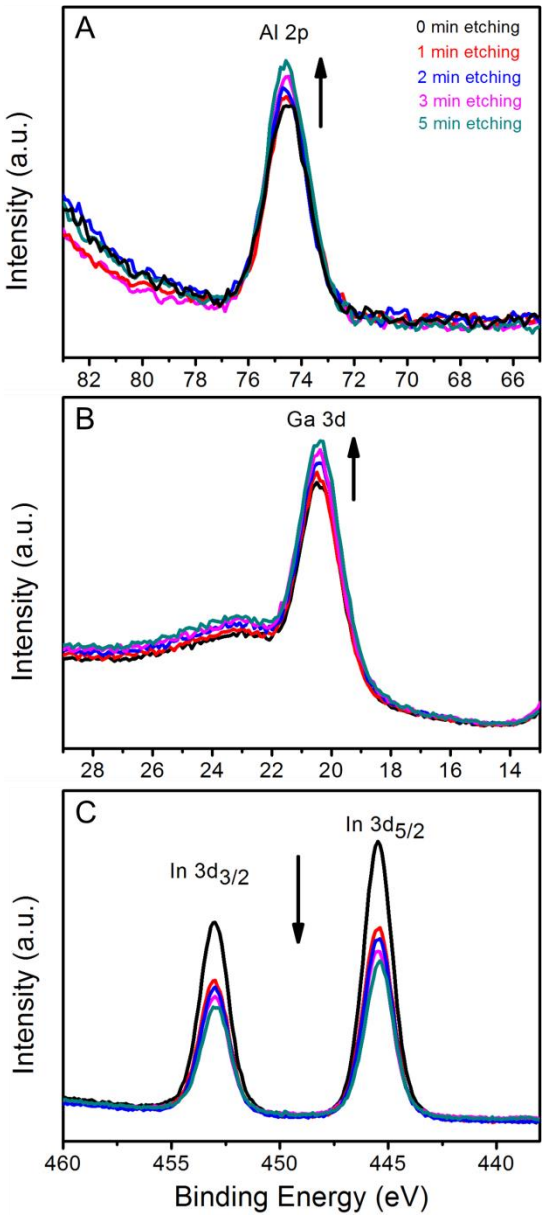

Figure 4.4. High resolution XPS spectra of Al 2p (A), Ga 3d (B), and In 3d (C) of AZO, GZO, and IZO as a function of etching time. Etching solution is HCl (0.5 mM, pH=4.5).

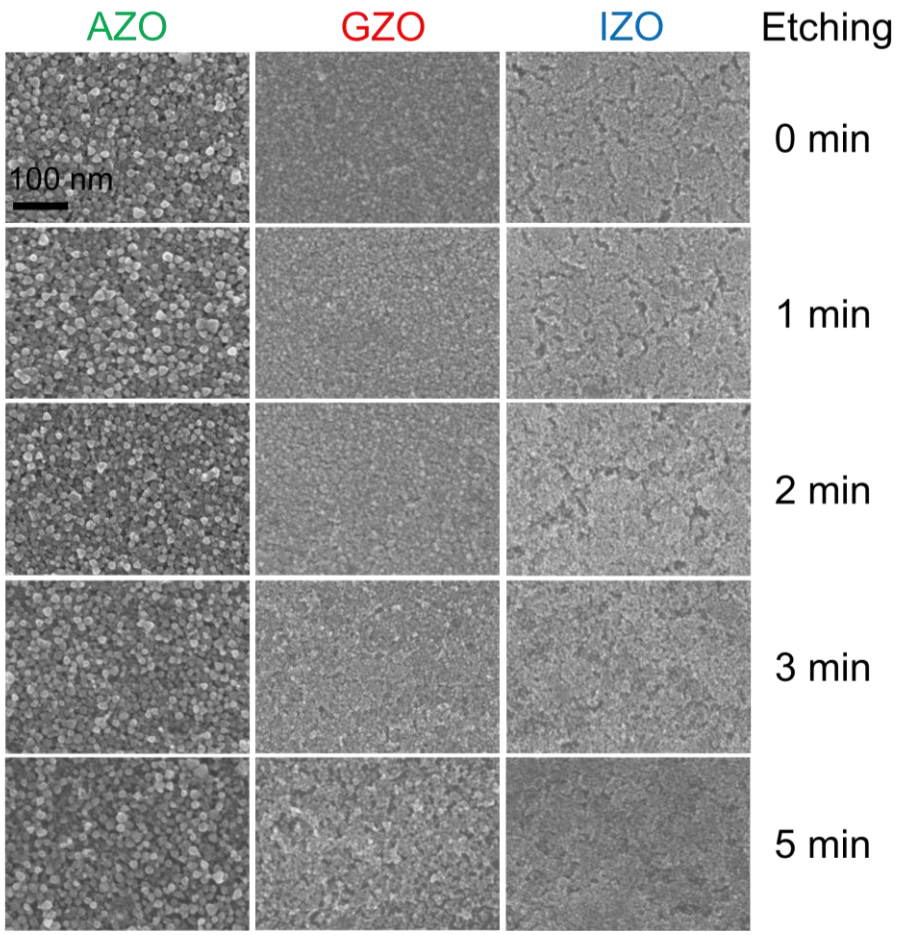

Figure 4.5. SEM images of AZO, GZO, and IZO as a function of etching time.

Chemical compositions of the doped ZnO nanocrystals are systematically studied by ICP and XPS. ICP measurements (Figure 4.6A) show that the LSPR peak position increases from 2562 and 3120 cm^{-1} up to 3056 and 4011 cm^{-1} with increased dopant concentration. The peak positions of both Al- and Ga- doped ZnO nanocrystal show a linear correlation with increasing dopant level which indicates the doping mechanism for both dopants are identical. From a comparison of the $[X(acac)_3]/[Zn(st)_2]$ ratios from precursor (0.1, 0.2, and 0.3 for AZO and GZO, 0.05, 0.2, and 0.5 for IZO) and [X]/[Zn] ratios from ICP (1.8, 2.6, and 3.8 % for AZO, 2.8, 4.7, and 7.2 % for GZO, and 2.3, 3.2, and 5.8 % for IZO) (Figure 4.6B), all the doped ZnO

nanocrystals show an approximately linear change with concentration, respectively. We can also clearly observe that the incorporation ratio of Ga atoms is highest among all doped zinc oxides with the same amount of precursor. It is due to Ga^{3+} share similar atom size with Zn^{4+} which result least lattice strain. The dopants concentration in the samples measured by ICP is consistent with that measured by XPS, which shows that XPS is capable to measure bulk elemental composition in the nanoparticles with diameter ~10 to 20 nm (Figure 4.6C).

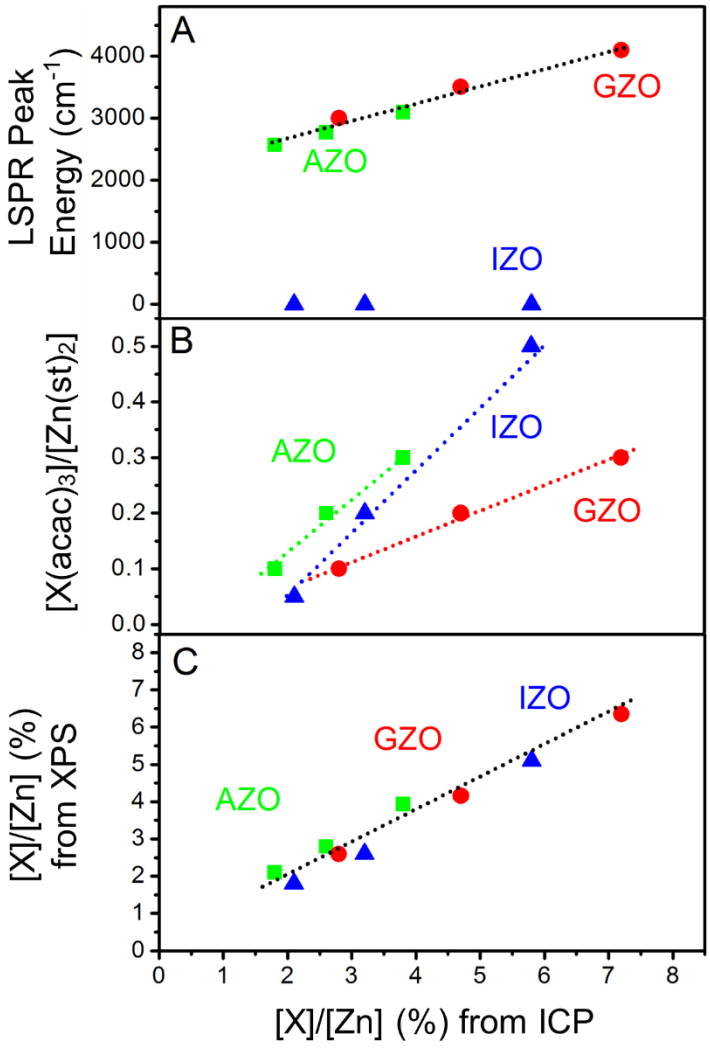

Figure 4.6. (A) LSPR peak energy of AZO (green), GZO (red), and IZO (blue) as the [X]/[Zn] (%) ratios from ICP. (B) $[X(acac)_3]/[Zn(st)_2]$ ratios from precursor and (C) [X]/[Zn] (%) ratios from XPS as the [X]/[Zn] (%) ratios from ICP. [X] presents Al, Ga, and In.

As shown in Figure 4.7 and 4.8, AZO and GZO nanocrystals films exhibit a LSPR near 3270 and 4782 cm^{-1} after spin-cast and ligand removal on the Al coated silicon substrate after annealing at 250 °C for 30 min (i.e., t=0 min). The LSPR red-shifts to approximately 2984 and 3424 cm^{-1} under 15 min O_2 annealing at 250 °C. (i.e., t=15 min). An inverse process occurs upon annealing AZO and GZO nanocrystals film in a vacuum environment for another 15 min and blue shifts back to 3125 and 4270 cm^{-1} at 250 ˚C for 15 min (i.e., t=30 min). While the hexagonal wurtzite crystal structure does not naturally possess oxygen vacancies, many observations in photo-luminescence, electron paramagnetic resonance spectroscopy, and conductivity measurements shows the existence of native oxygen vacancies and their modulation by annealing in ZnO nanostructures.[107-109] We attribute the observed red-shift and blue-shift upon O_2 and vacuum annealing to reversibly filling the oxygen vacancies in the lattice. The additional interstitial oxygen atoms trap the free electrons donated by dopants and cause the observed LSPR change. Comparing AZO and GZO at the same temperature, we found that the shifts of GZO are significantly stronger than that of AZO which indicates there are more oxygen defects in GZO.

The experimental results at different temperatures (300 and 350 ˚C) are also shown in Figure 4.7 and 4.8. Before annealing, LSPR peak energies of AZO and GZO located at 3533 and 4851 cm^{-1} for 300 ˚C and 3768 and 4937 cm^{-1} for 350 ˚C (t=0 min). The cause of the difference in LSPR energies before annealing is due to equilibrium oxygen vacancies differences at different temperature.[107] The LSPR peak energies of AZO and GZO red-shift to 2762 and 3101 cm^{-1} for 300 ˚C and 2610 and 2586 cm^{-1} for 350 ˚C (t=15 min), blue-shift back to 3203 and 4420 cm^{-1} for 300 ˚C and 3408 and 4610 cm^{-1} for 350 ˚C (t=30 min). Notice that the higher the temperature, the stronger the red-shift of AZO and GZO for O_2 annealing, which indicate that more oxygen atoms diffuse into the bulk and trap more free electrons similar to previous

reported system in ITO nanocrystals.[110] LSPR peak position of AZO and GZO are plotted in Figure 4.9 as a function of time for O_2 and vacuum annealing at 250, 300, and 350 ˚C, respectively. For all O_2 annealing, a red-shift occurs at short times before saturation at long times. For vacuum annealing, LSPR blue-shifts back to closed original peak position at 250, 300, and 350 ˚C, respectively. The higher the temperature, the faster the red- and blue-shifts. Notably, red-shift in O_2 annealing is faster than blue-shift in vacuum annealing.

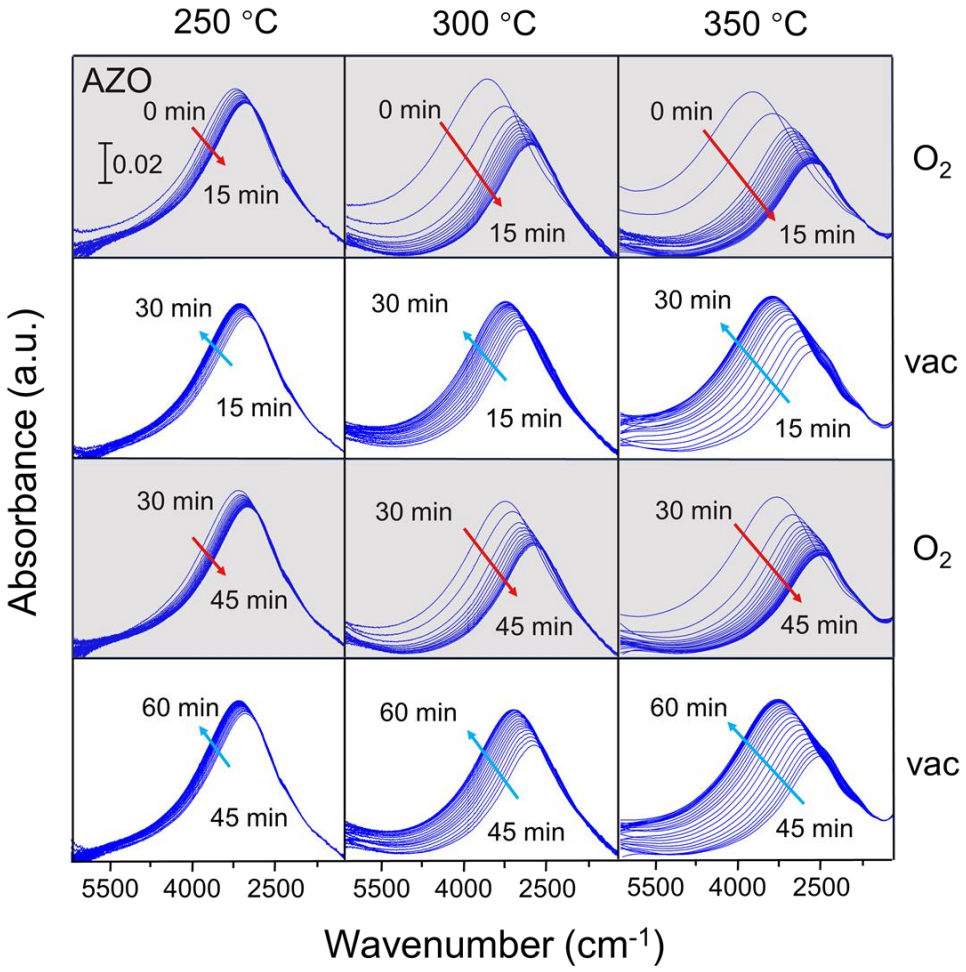

Figure 4.7 Absorption spectra of AZO as a function of time during O_2 and vacuum at 250, 300, and 350 ˚C.

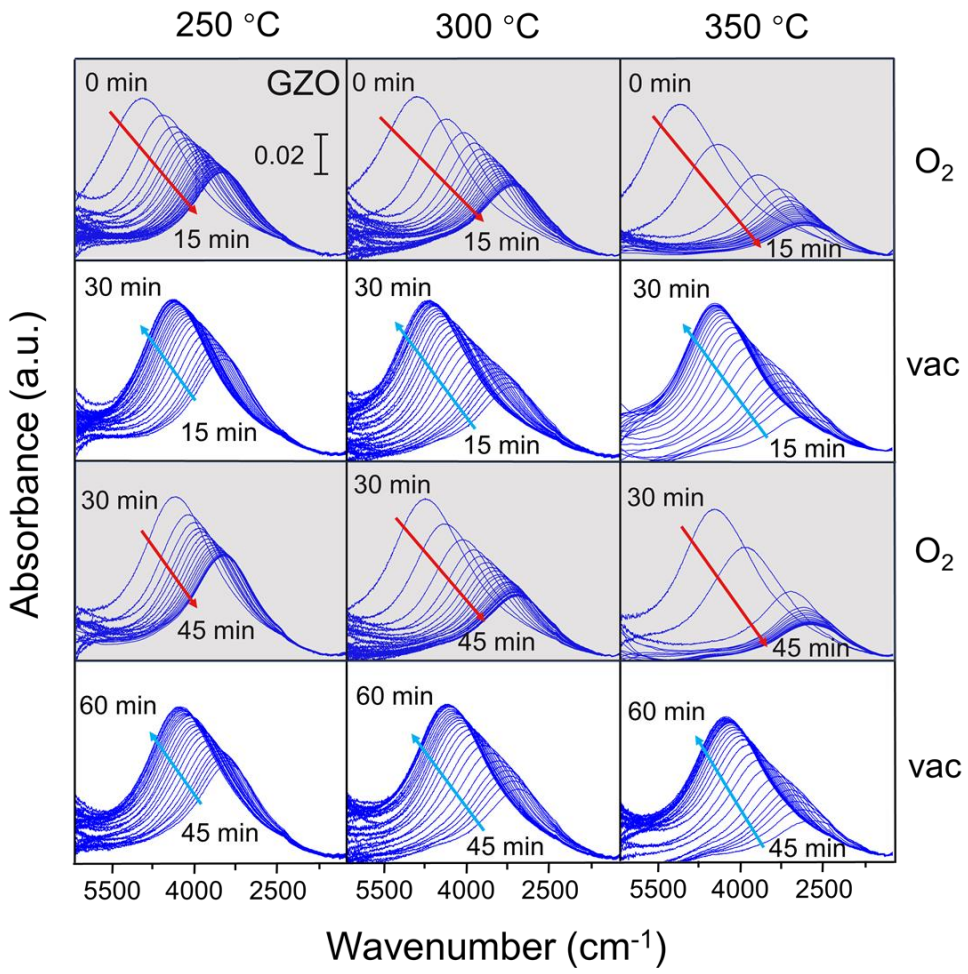

Figure 4.8 Absorption spectra of GZO as a function of time during O_2 and vacuum at 250, 300, and 350 ˚C.

4.5 Conclusions

In conclusion, we have presented a detailed study of the dopant effect (Al, Ga and In) on plasmonic properties of ZnO nanocrystals synthesized by hot injection method. Through the controlled doping of Al and Ga, ZnO nanocrystals exhibit a surface plasmon resonances in the mid-infrared. Importantly, we show that the plasmonic quality factors of AZO and GZO are

comparable to widely used ITO and they can serve as a cost-effective substitution for infrared applications.

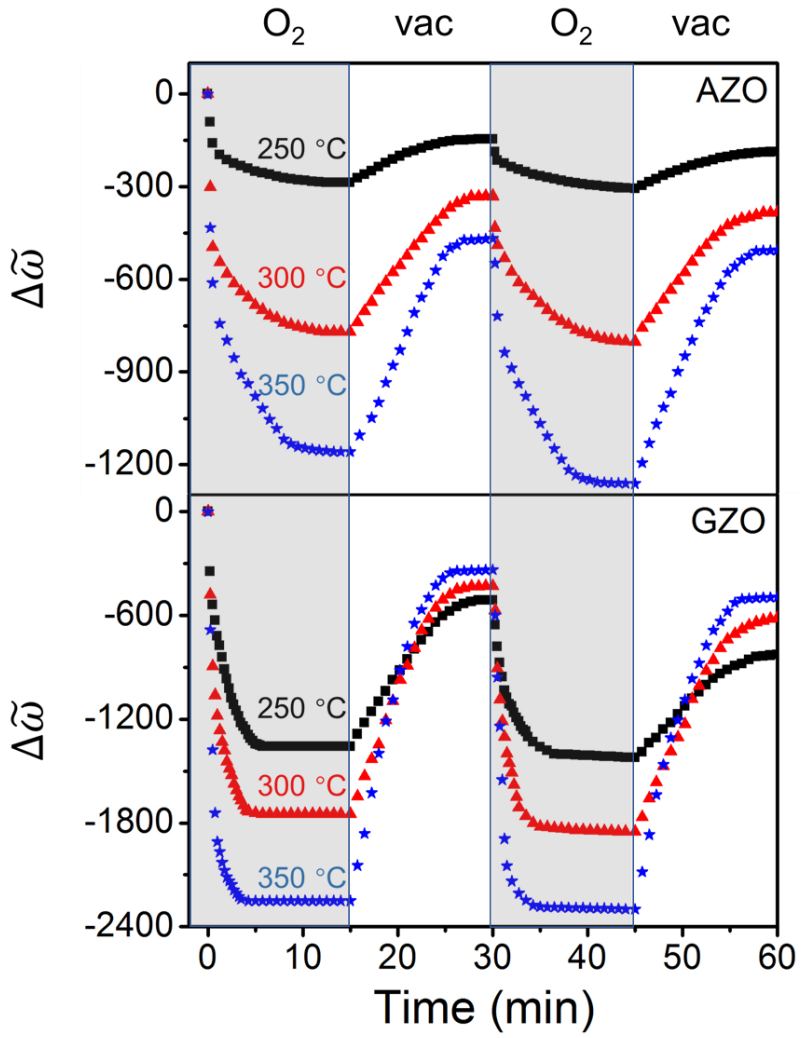

Figure 4.9 Peak position as a function of time for O_2 and vacuum at 250 (black squares), 300 (red triangles), and 350 (blue stars) ˚C.

The modulation of LSPR through gas-phase oxidation and reduction provide extra degree of freedom to engineer the optical properties in these material as shown in Figure 4.9. However, with same reaction condition, there is no such absorption in In doped ZnO nanocrystals. The

elemental analysis of etched nanocrystals indicates the dopant surface segregation limits the generation of free electrons. More controlled synthesis conditions need to be further investigated to enable plasmonic properties in IZO.

CHAPTER 5

ENHANCED PHOTODESORPTION FROM MID-INFRARED PLASMONIC NANOCRYSTAL THIN FILMS

5.1 Overview

In previous two chapters, we demonstrate the impact of chemical reactions on LSPRs supported by ITO, AZO and GZO. In the opposite way, exploring the plasmonic effect on surface adsorbates may provide us more insight of the interplay between low-energy localized surface plasmons and surface reactions. In this chapter, we show that the desorption rate of two model molecules, indole and benzoic acid, from thin films of indium tin oxide (ITO) nanocrystals supporting near- and mid-infrared (0.33 – 0.48 eV) localized surface plasmon resonances (LSPRs) is enhanced by as much as 60% upon illumination with broadband infrared light. The desorption rate increases linearly with light intensity. No increase in desorption rate is detected for undoped In_2O_3 nanocrystal thin films or when photons resonant with the LSPR are blocked. We study desorption rate enhancement as a function of illumination intensity, LSPR energy, and isotopic substitution. Importantly, we demonstrate accelerated desorption via in-coupling of light to LSPRs with energies lower than previously reported. Our work opens the door to mid-infrared photons as choreographers of chemical processes and sets the stage for future mechanistic studies.

5.2 Introduction

Photons have long been used as reagents in chemical reactions.[111-114] Light can improve the spatial and temporal resolution of energy delivery[115-116] and also control product

distribution.[117] The majority of photochemical transformations utilize ultraviolet, visible, and near-infrared photons to electronically excite one or more of the reactants. Mid-infrared photons, although much less studied than their ultraviolet, visible, and near-infrared counterparts, are also intriguing modifiers of chemical transformations. Mid-infrared photon-driven chemistry has been explored in the gas phase[96, 118-119] and on surfaces.[93-95, 120-123] Early studies of heterogeneous processes showed that heating induced by resonant excitation of adsorbate vibrational degrees of freedom can induce desorption.[120-123] State-resolved experiments demonstrate that vibrational mode excitation of impinging molecules can, in some situations, result in athermal surface product distributions.[94] In either case, the small cross-sections of vibrational modes necessitates the use of large photon fluxes that, although suitable for fundamental studies, limits the widespread utility of mid-infrared light for controlling chemistry.

Localized surface plasmons resonances – the collective oscillation of charge carriers sustained by small particles – have recently gained prominence due to their large absorption cross-sections and ability to confine light into deep subwavelength volumes. The acceleration of several reactions, including water splitting, hydrogen dissociation,[20] ethylene epoxidation,[21-22] and methane formation,[23] by visible LSPRs has been reported. The catalytic effects of near-infrared LSPRs are demonstrated recently as well.[124-125] Experiments definitively confirm the role of the LSPR, but also identify multiple energy transfer mechanisms, including direct coupling,[24-25] hot electron,[20, 126-127] and heating.[128-129] Doped semiconductor nanostructures, including colloidal metal oxide nanocrystals,[130] plasma-synthesized Si nanocrystals,[43] and vapor-liquid-solid (VLS)-grown Si nanowires,[41] have recently been shown to support LSPRs in the near- and mid-infrared. Unlike noble metals, the carrier density of semiconductors can be readily

tuned via chemical doping.[48, 131] Redox reactions[110, 132] or photoexcitation[63, 133] also provide a route to actively modify the LSPR.

The ability of mid-infrared LSPRs to modify chemistry, via any mechanism, and whether practical utility can be derived from such a process, is an open question. While the limited energy of each infrared photon and the associated LSPR indicate that any influence might be minor, several other considerations suggest that exciting opportunities do exist. While the energy of an individual infrared LSPR is small, hot spots can lead to locally outsized effects.[134-135] The design of multispectral absorbers would allow for the 'integration' of multiple, energetically-distinct photons.[136] In the event of direct infrared LSPR-molecular coupling, as supported by recent work,[51] the diversity of molecular structures, and thus vibrational fingerprints, provides a nearly limitless playground with which to engineer energy transfer. As mid-infrared (i.e., thermal) radiation is generated from bodies at temperatures between about 100 and 300 °C, broadband photon sources are readily available.

Here, we use infrared spectroscopy to study the influence of near- and mid-infrared LSPRs (0.33 – 0.48 eV) on the simplest heterogeneous chemical process: desorption. The simplicity of desorption is ideal for initially exploring low energy infrared LSPR-induced photochemistry, but it is also relevant to applications such as pressure swing adsorption and catalyst regeneration. More specifically, we investigate the desorption of model molecules – indole and benzoic acid – from thin films of heavily-doped indium tin oxide (ITO) nanocrystals at room temperature. We find that the desorption rate of these molecules upon illumination with broadband infrared light increases by as much as 60%. This effect is only observed when nanocrystals support a LSPR resonate with the incident photon flux. Studies of desorption rate enhancement as a function of illumination intensity, LSPR energy, and isotopic substitution are

conducted to understand the underlying mechanism. Importantly, we demonstrate enhanced desorption for plasmon energies well within the mid-infrared spectral regime.

5.3 Experimental Details

Time-dependent infrared spectra of indole and benzoic acid multilayers on ITO or In_2O_3 nanocrystal thin films are collected in a transmission geometry, as shown in Figure 5.1. ITO or In_2O_3 nanocrystal thin films are mounted on the transmission film holder (Figure 2.5) and placed in the IR sample compartment. Detection light from the spectrometer is incident upon the nanocrystal thin film at an angle of 40°.

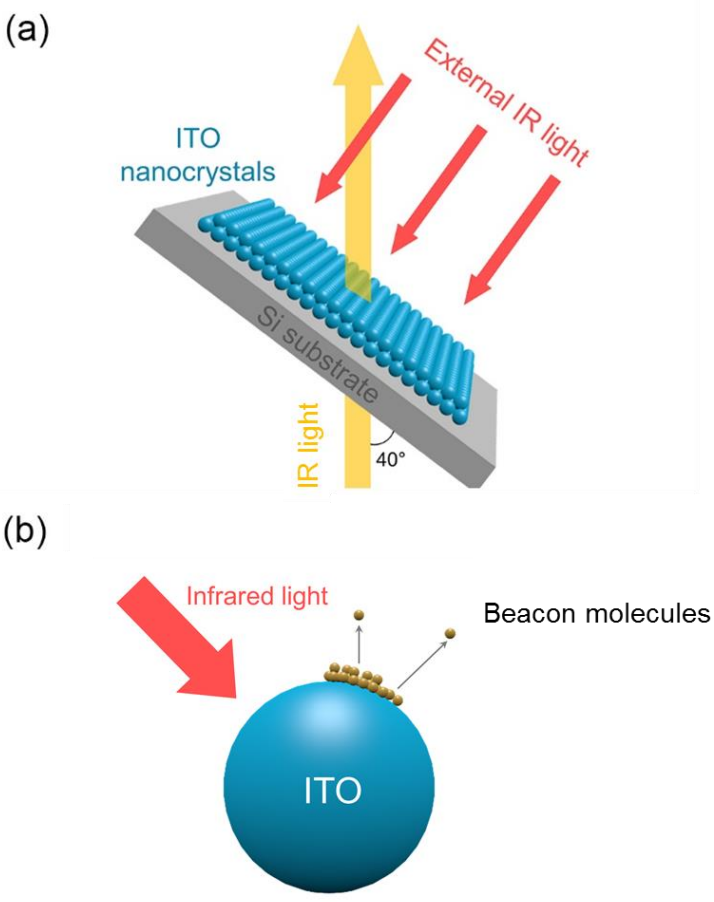

Figure 5.1. (a) Schematic illustration of IR measurement of molecular desorption from mid-infrared plasmonic nanocrystal thin films. The detection light passes through the ITO nanocrystal

thin film with a 40° angle. The illumination light is perpendicular to the film. (b) Illustration of the desorption process on a single ITO nanocrystal.

ITO and undoped In_2O_3 nanocrystals with average diameters of ~10 nm are synthesized with previously reported colloidal methods.[50] ITO nanocrystals contain 13.4 atom% Sn, as approximately determined by X-ray photoelectron spectroscopy (not shown). As shown in Figure 5.2, uniform nnanocrystal thin films, of ITO and In_2O_3, are deposited via spin-coating. A Si wafer (El-Cat, 25 × 5 × 0.5 mm, FZ, 15-30 ohm-cm, double-side polished) is cut into 1.5 cm × 1.5 cm squares and cleaned via sonication in deionized water, acetone, and hexane for 15 minutes each. 70 μL ITO/hexane solution (~30 mg/mL) is spin-cast onto the Si substrate in a two-step procedure: an initial 1000 rpm spin for 30 seconds followed by a 4000 rpm spin for 20 seconds. The ITO surface ligands are removed by UV-ozone (Hitachi, ZONETEM) for 30 min. The resulting nanocrystal thin films are ~30 nm thick. Indole (C_8H_7N, Sigma-Aldrich, ≥99%) and benzoic acid (C_6H_5COOH, Sigma-Aldrich, ≥99.5%) are dissolved in methanol (CH_3OH, BDH, 99.8%) to make 0.1 M solutions. For the indole-d_7 (C_8D_7N, C/D/N Isotopes Inc., 98 atom % D) solution, fully deuterated methanol (CD_3OD, C/D/N Isotopes Inc., 99 atom % D) is used as a solvent to limit isotopic exchange. For each experiment, these solutions are spin-cast onto the nanocrystal thin films initially at 2000 rpm spin for 5 seconds and followed by 1000 rpm for 15 seconds.

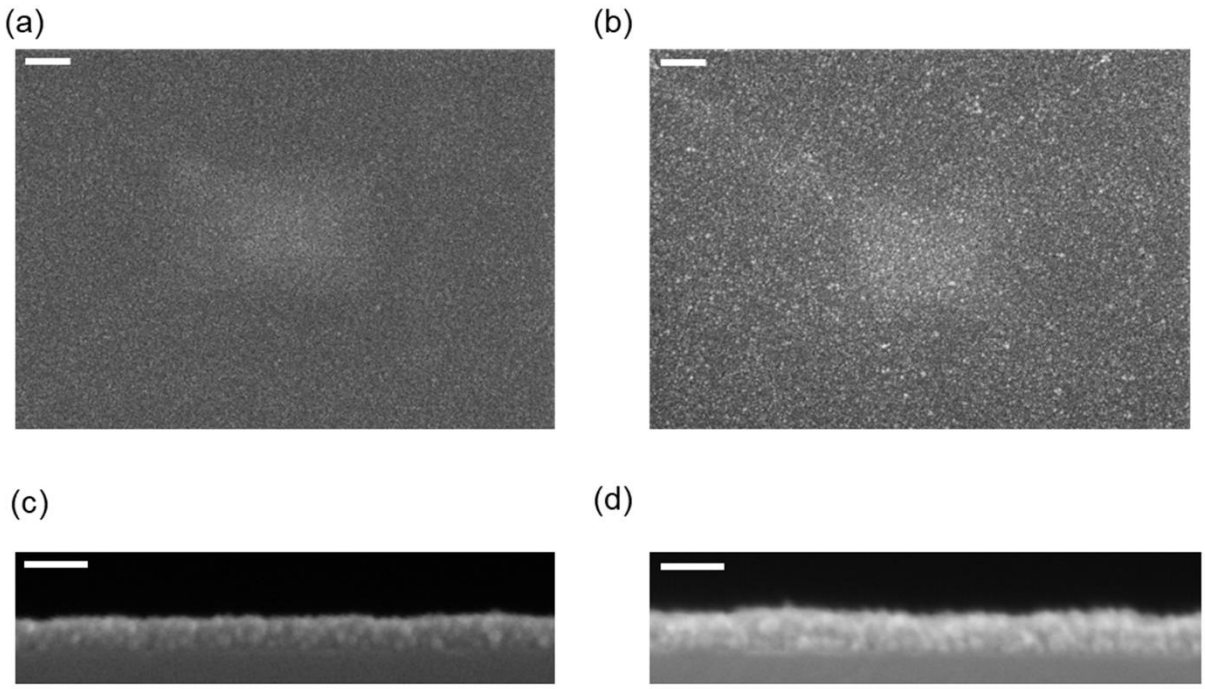

Figure 5.2. Top-down SEM images of representative (a) ITO and (b) In_2O_3 nanocrystal thin films. Scale bars, 200 nm. Cross-sectional SEM images of representative (c) ITO and (d) In_2O_3 nanocrystal thin films. Scale bars, 50 nm.

Spectra are collected at room temperature with a Fourier transform infrared (FTIR) spectrometer (Bruker, Vertex 70) equipped with an unpolarized mid-infrared source, a KBr beam splitter, and a liquid nitrogen-cooled HgCdTe detector. The spectrometer resolution is 4 cm^{-1}. Each spectrum consists of 64 scans and the background is that of the nanocrystal thin film on a Si substrate following UV-ozone treatment. Indole and benzoic acid desorption are monitored under 'dark' and 'light' conditions. Under light conditions, the nanocrystal film is illuminated with an external, broadband, and unpolarized infrared light source (Thorlabs, SLS203L) at normal incidence. The intensity of the external infrared source (Molectron, PM5200) is approximately two orders magnitude higher than the infrared spectrometer's internal light source.

Light intensity at the nanocrystal film surface is controlled by varying the distance of the external infrared light source. Any contributions to desorption rate from the spectrometer itself, while negligible relative to the external light source, would affect all measurements (i.e., light and dark) equally. Measurements are completed with a long wavelength pass filter (Spectrogon, LP-2000) that blocks photons from the external infrared source above 5000 cm^{-1} (Figure 5.3). A short wavelength pass filter (Spectrogon, SP-2010), which is used instead of the LP-2000 filter where noted, blocks photons with energies less than 5000 cm^{-1} (Figure 5.3).

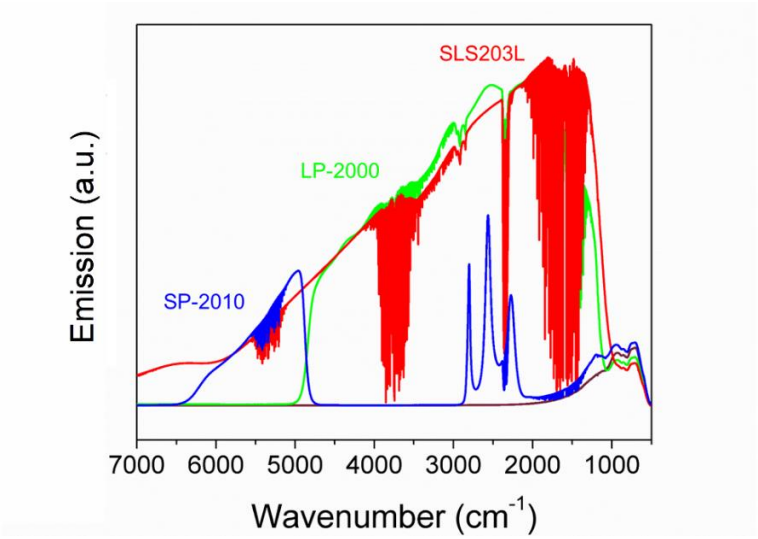

Figure 5.3. Emission spectra of short wavelength pass filter SP-2010 (blue), long wavelength pass filter LP-2000 (green), and the external IR light source (SLS203L) without a filter.

As shown in Figure 5.4, desorption rate is quantitatively determined by monitoring the (loss of) integrated intensity of υ(N−H) (~3400 cm^{-1}) and υ(C=O) (~1690 cm^{-1}) stretching modes for indole and benzoic acid, respectively. Data points, including averages and error bars, are from the integrated peak intensity for 3 distinct desorption experiments.

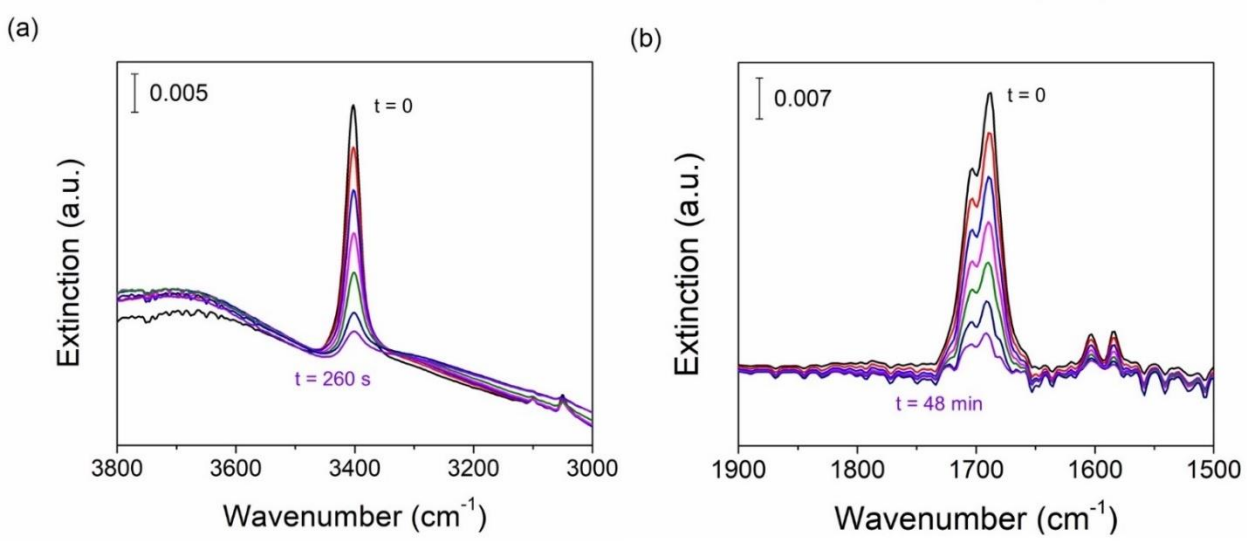

Figure 5.4. Time-dependent *in situ* IR spectra of the (a) ν(N–H) stretching region during indole desorption and (b) ν(C=O) stretching region during benzoic acid desorption from an ITO nanocrystal thin film.

5.4 Results and Discussion

Figure 5.5 shows the infrared extinction spectra of ITO and In_2O_3 nanocrystal thin films following UV-ozone cleaning. A strong LSPR, consistent with the literature,[59] is observed only for the ITO nanocrystal thin film at ~4000 cm^{-1}. Undoped In_2O_3 nanocrystals are an excellent control because they do not support an LSPR, but exhibit nanocrystal and film morphologies similar to ITO. Spectral features associated with nanocrystal ligands (e.g., υ(C−H)) are not observed for ITO nor In_2O_3 following UV-ozone treatment.

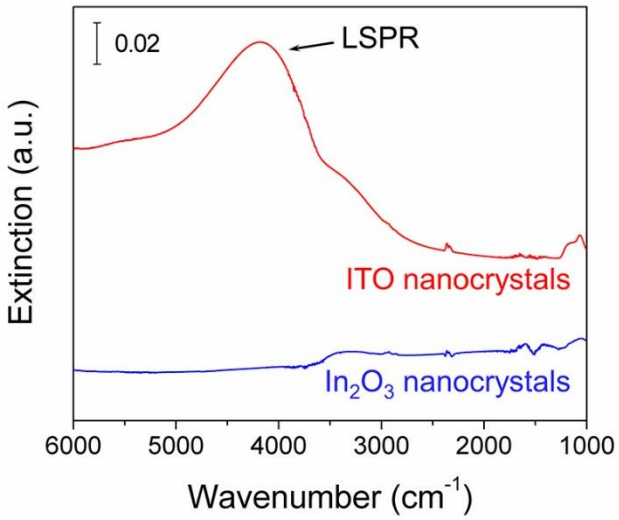

Figure 5.5. Extinction spectra of ITO and In_2O_3 nanocrystal thin films on Si substrates.

Dark and light integrated peak intensities (normalized to the initial intensity) as a function of time for indole and benzoic acid desorption are shown in Figures 5.6(a) and 2(b), respectively. For all situations, the quantity of adsorbed indole and benzoic acid decreases linearly with time, and is consistent with the zeroth-order sublimation of molecular multilayers.[137] The desorption rate of both molecules from In_2O_3 nanocrystals is indistinguishable in the dark and light. For ITO nanocrystal films, however, illumination with infrared light leads to a clear increase in desorption rate for both molecules. At this light intensity (185 mW/cm^2), the desorption rate enhancements for indole and benzoic acid on ITO nanocrystals are 60 ± 2 % and 49 ± 6 %, respectively. We attribute the enhancement difference to each molecule's volatility. The sublimation energy of indole ($\Delta_{sub}H°_{indole}$ = 77.6 kJ/mol[138]) is lower than benzoic acid ($\Delta_{sub}H°_{benzoic\ acid}$ = 93.3 kJ/mol[139]), which supports indole's larger increase in desorption rate. Importantly, no rate enhancement is found when photons with energies below 5000 cm^{-1} are blocked using a short wavelength pass filter (Figure 5.6).

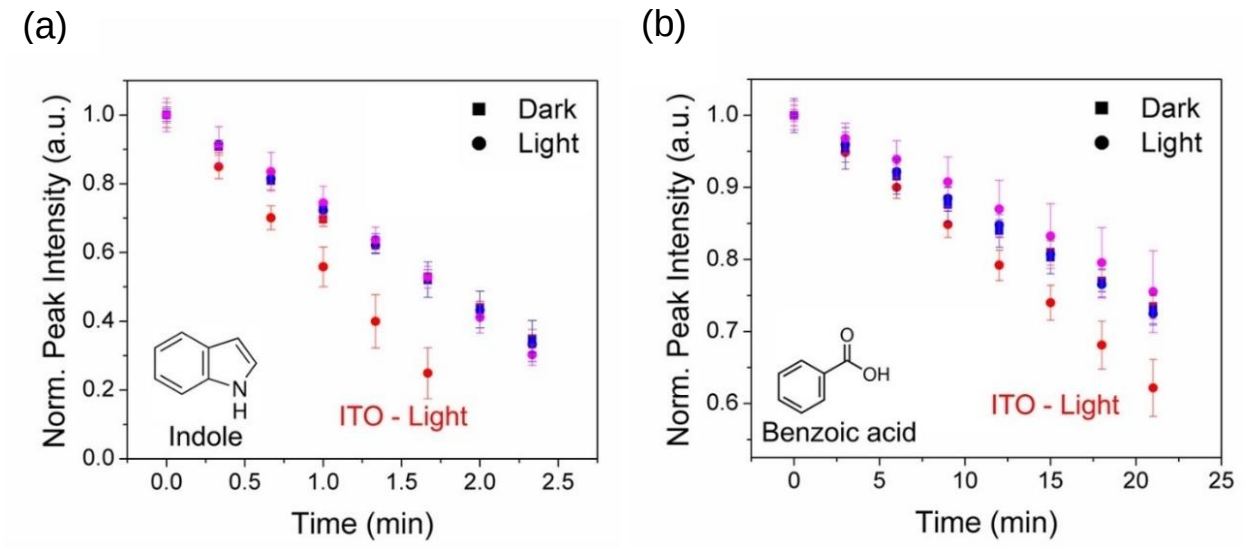

Figure 5.6. Integrated intensity of (a) indole υ(N-H) and (b) benzoic acid υ(C=O) stretching peaks as a function of time during desorption from ITO w/ long wavelength pass filter (red) and w/ short wavelength filter (magenta); In_2O_3 (blue) nanocrystal thin films at room temperature.

Desorption rate increases as a function of external infrared light intensity as displayed in Figures 5.7(a) and (b) for indole and benzoic acid, respectively.

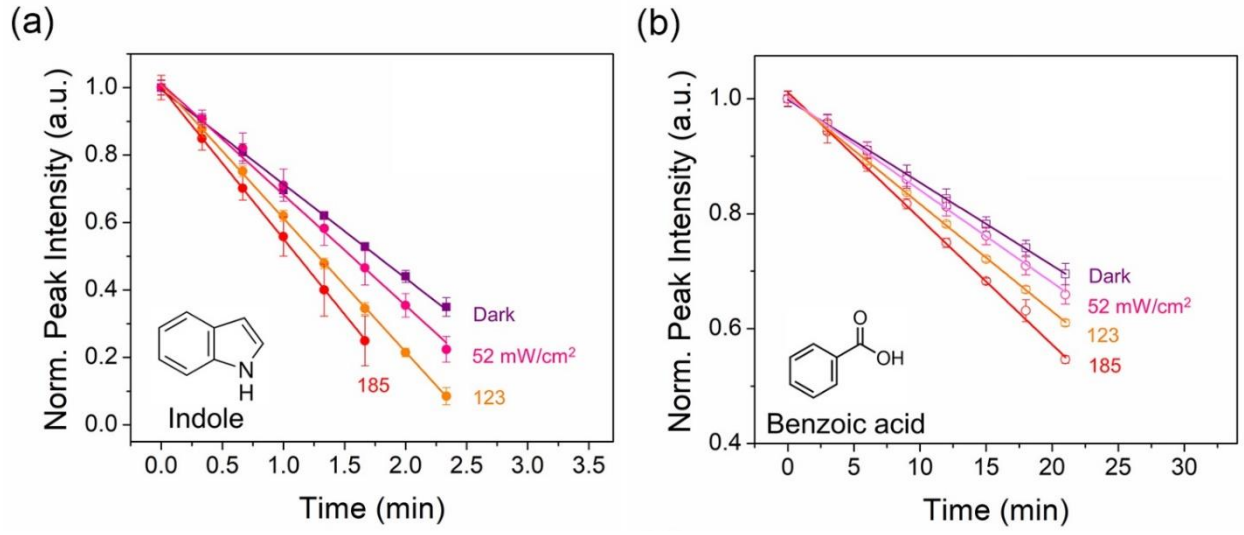

Figure 5.7. Integrated intensity of the (a) ν(N-H) stretching peak of indole and (b) ν(C=O) stretching peak of benzoic acid as a function of time during indole and benzoic acid desorption,

respectively, from an ITO nanocrystal thin film under dark conditions (purple) and light illumination at 52 (pink), 123 (orange), and 185 (red) mW/cm^2.

Figure 5.8 shows a linear dependence of desorption rate as a function of light intensity for both molecules. These data collectively indicate that the LSPR is playing a central role in the enhanced desorption rate and that the desorption rate enhancement is due to a single-photon process, as reported for ultraviolet/visible LSPRs.[20, 22]

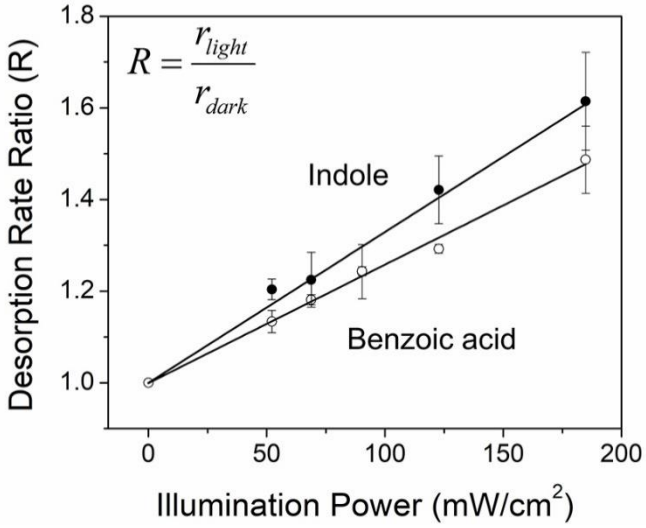

Figure 5.8. Indole and benzoic acid desorption rate ratio as a function of illumination power.

We next study desorption rate as a function of LSPR energy and isotopic substitution. As shown in Figure 5.9(a), the LSPR is redshifted from 4200 to 2600 cm^{-1} by air annealing at 200 °C using our previously reported procedure.[110] This treatment reduces the free carrier density of the ITO nanocrystals, but leaves the nanocrystal and film morphology nominally unchanged.[110] Figure 5.9(b) shows that the desorption rate of indole is, within the sensitivity of

our measurements, the same at both LSPR energies. However, we emphasize that 2600 cm^{-1} is well within the mid-infrared, but these LSPRs can still accelerate desorption rate.

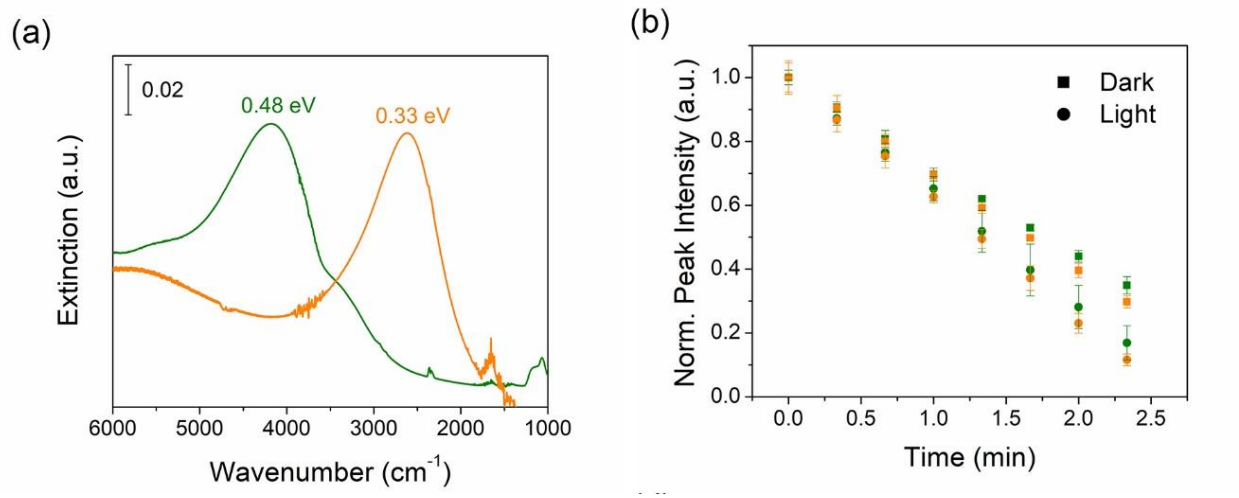

Figure 5.9. (a) Extinction spectra of ITO nanocrystal thin films as prepared (0.48 eV) or following air annealing at 200 °C (0.33 eV). (b) Integrated intensity of the ν(N-H) stretching peak of indole as a function of time during indole desorption from a ITO nanocrystal thin film with a LSPR centered at 0.33 (orange) and 0.48 eV (green) under dark (squares) and light (circles) conditions.

Figure 5.10(a) shows the extinction spectrum of indole and indole-d_7 adsorbed on ITO nanocrystal thin films. The main spectral differences are the ν(N–H) and ν(N–D) peaks at 3402 cm^{-1} and 2520 cm^{-1}, respectively. We attribute the broad peak near 3800 cm^{-1} to changes in the dielectric environment surrounding the nanocrystals upon adsorption of the molecular multilayer. Figure 5.10(b) compares the desorption rate enhancement for indole and indole-d_7 from an ITO nanocrystal film with an LSPR centered at 4200 cm^{-1}. While this energy is strongly resonate with the ν(N–H) stretch of indole, we cannot observe a difference in desorption rate for indole and indole-d_7.

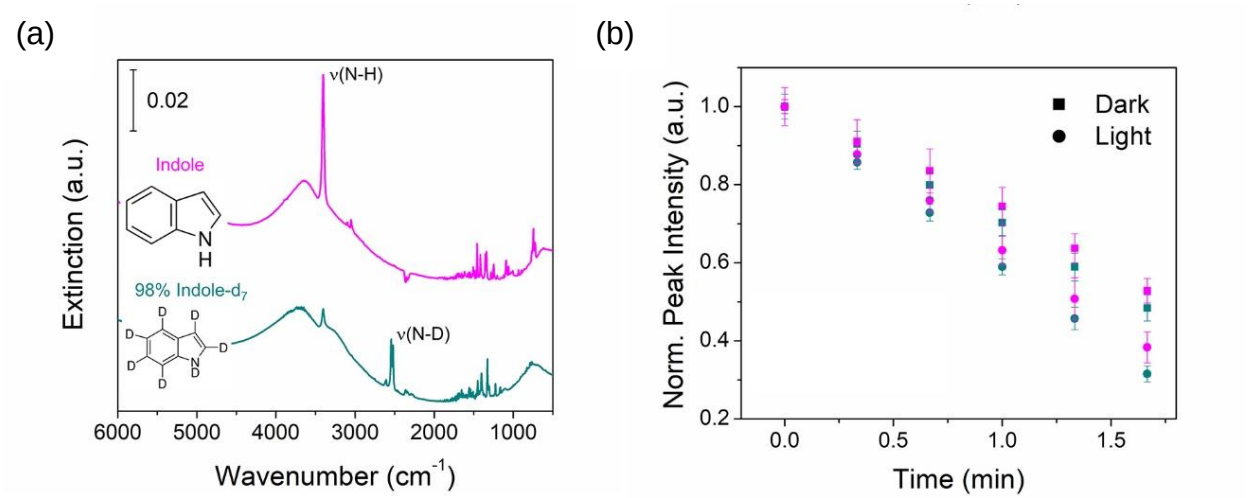

Figure 5.10. (a) Extinction spectra of indole and indole-d_7 multilayers adsorbed on an ITO nanocrystal thin film. (b) Integrated intensity of the ν(N-H) stretching peak of indole (magenta) and ν(N-D) stretching peak of indole-d_7 (cyan) as a function of time during indole and indole-d_7 desorption from a ITO nanocrystal thin film with a LSPR centered at 0.48 eV under dark (squares) and light (circles) conditions.

Our experiments show that low energy infrared LSPRs can accelerate the desorption rate. The lack of a LSPR energy or isotope dependence argue against an athermal mechanism. If the process is predominantly thermal in nature, a kinetic model of zeroth-order desorption,[120] which is consistent with the observed desorption rate (Figure 5.6), allows the average temperature rise within the ITO nanocrystal thin film to be extracted. The rate of desorption can be expressed as:

$$r_{sub} = -\frac{dN_A}{dt} = -k \tag{5.1}$$

where N_A is the number of molecules on the nanocrystal surface, k is the Arrhenius rate constant, and t is time. Integration of Equation (1) with $N_A = N_{A0}$ at $t = 0$ yields:

$$N_A = -kt + N_{A0} \tag{5.2}$$

The rate constant is the slope of the curve in any integrated intensity vs. time plot (e.g., Figure 5.6(a)). The ratio of the rate constants for desorption in the light and dark, including the Arrhenius dependence of each, is:

$$\frac{k_{light}}{k_{dark}} = \frac{k_0 e^{\frac{-\Delta_{sub}H^\circ}{RT_{light}}}}{k_0 e^{\frac{-\Delta_{sub}H^\circ}{RT_{dark}}}} \tag{5.3}$$

We assume the activation energy for desorption is equal to the heat of sublimation (*vide supra*) for each molecule and T_{dark} = 298.5 *K*. A thermally-driven desorption mechanism at the observed rate requires an average temperature rise of 4.6 and 3.2 K for indole and benzoic acid, respectively.

The maximum temperature rise following LSPR excitation can be derived from the energy balance. For a single spherical particle with diameter R, the heat in equals the heat out which gives:

$$q_r = -kA\frac{dT}{dr} \tag{5.4}$$

where q_r is the total energy in, k is the surrounding thermal conductivity, A is the area. Substitute the spherical surface area in to equation 5.4,

$$q_r = -k \bullet 4\pi r^2 \frac{dT}{dr} \tag{5.5}$$

By integration, we get:

$$q_r \int \frac{1}{r^2} = -4\pi k \int dT$$

$$q_r\left(\frac{1}{r_2}-\frac{1}{r_1}\right)=-4\pi k\left(T_2-T_1\right) \tag{5.6}$$

Assuming the thermal conductivity inside of the particle is much higher than the surrounding (which is beacon molecules or air), the temperature is uniform inside of the particle:

$$T=T_{\max}\left(r\le R\right) \tag{5.7}$$

Relative to the environmental temperature where $r=\infty$, the maximum temperature on the particle can be derived from equation 5.6 as:

$$T_{\max}=\frac{q_r}{4\pi k}\left(\frac{1}{R}\right) \tag{5.8}$$

We can also calculate analytically the heat generation Q, with the assumption that the wavelength of the incident light is much longer than the nanocrystal radius ($\lambda \gg R$): [140]

$$Q=\frac{\omega}{8\pi}E_0^2\left|\frac{3\varepsilon_0}{2\varepsilon_0+\varepsilon_{NP}}\right|^2\mathrm{Im}\left(\varepsilon_{NP}\right) \tag{5.9}$$

where E_0 is the amplitude of the incident radiation, ε_{NP} and ε_0 are the dielectric constants of the nanocrystals and surrounding medium, respectively.

$$q_r=Q\cdot V \tag{5.10}$$

According to the illumination light intensity expression, we can get the amplitude of the incident radiation as:

$$\frac{cE_0^2\sqrt{\varepsilon_0}}{8\pi}=I\left(t\right)=I_0 \tag{5.11}$$

$$E_0^2=\frac{8\pi I_0}{c\sqrt{\varepsilon_0}} \tag{5.12}$$

where c is the speed of light. Substitute equation 5.9, 5.10 and 5.12 into equation 5.8, we get the maximum temperature

$$\Delta T_{\max} = \frac{R^2}{3k}\frac{\omega I_0}{c\sqrt{\varepsilon_0}}\left|\frac{3\varepsilon_0}{2\varepsilon_0+\varepsilon_{NC}}\right|^2 \mathrm{Im}\left(\varepsilon_{NC}\right) \quad (5.13)$$

The maximum temperature rise, according to this model, should be no more than 10^{-6} K for our mid-IR LSPRs, which is many orders of magnitude below what is required to achieve the desorption rate observed here. Multiple mechanisms may account for this discrepancy, including near-field interactions and ensemble effects. Plasmonic hot spots can yield local thermal enhancements as large a several hundred degrees of ambient for visible LSPRs.[141-143] It has also been reported that the temperature rise in nanocrystal ensembles depends linearly on cluster size.[134-135] While the energy accumulated within a nanocrystal thin film may be substantial, we note that linear scaling on cluster size cannot continue *ad infinitum*.

We note that the observed linear dependence of external light intensity on desorption rate is, in fact, consistent with an athermal mechanism. The further investigation of athermal mechanisms is supported by recent demonstrations that visible LSPRs are able to directly transfer energy to nearby reacting molecules[16] and that infrared LSPRs can couple to adsorbed ligands.[144] Future studies will be facilitated by improved nanocrystal properties (e.g., monodisperse morphologies and sizes,[145] narrower bandwidths[105]) as well as better controlled reactive environments (e.g., monolayers rather than multilayers).

5.5 Conclusions

Our work demonstrates that heavily-doped ITO nanocrystals supporting low energy infrared LSPRs enhance the rate of molecular desorption when illuminated. Relative to past studies of mid-infrared light-induced desorption on non-plasmonic surfaces,[120-122] the strong in-coupling of light by LSPRs greatly reduces the required photon flux and enables local energy

delivery. Our experiments make clear that LSPRs well within the mid-infrared can affect chemistry and we anticipate new opportunities will emerge as the underlying mechanisms become better understood and controlled.

CHAPTER 6

CONCLUSION AND PERSPECTIVE

6.1 Impacts

Throughout this thesis, we have presented the interplay between low energy LSPRs and surface adsorbates on doped metal oxides, which have been previously underestimated due to its low energy. In chapter 3, we have introduced a brand new gas-phase annealing method for dynamical LSPR modulation. Using ITO as a model, the underlying physicochemical processes which involve a nanocrystal redox reaction, solid-state diffusion, carrier density modulation are systematically studied using a reaction-diffusion model. The key advantages of this method is that it provides a more precise engineering of the optical properties through controlling the time and temperature of reaction. More importantly, the LSPR energy remains unchanged post annealing, and stable for months in atmosphere (Figure 6.1).

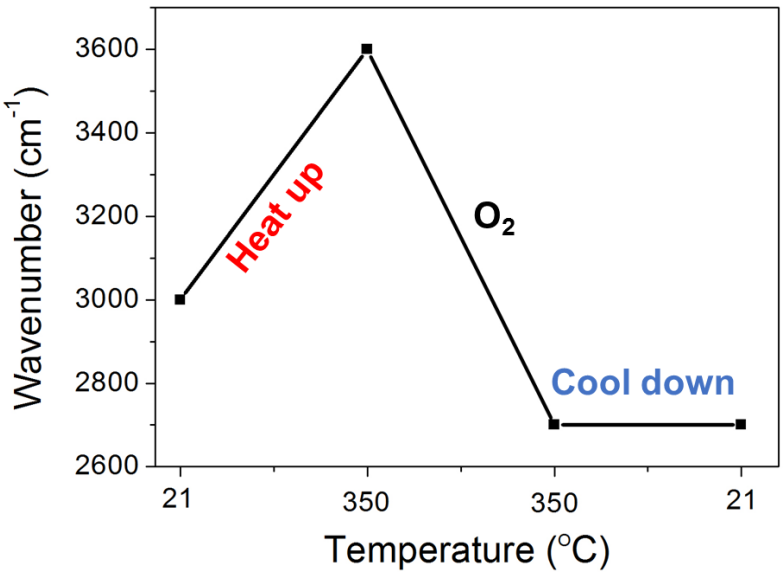

Figure 6.1. Absorption spectra of AZO as a function of temperature during O_2 annealing.

In parallel, our research on doped ZnO nanocrystals yielded similar results in LSPR modulation via chemical redox reactions. In both cases, interstitial oxygen compensation plays the key role in the modulation which indicate this method can be universally applied to plasmonic metal oxide with a similar doping mechanism. In Chapter 4, we also systematically studied the synthesis of Al-, Ga- and In-doped ZnO nanocrystals by the hot-injection method. We demonstrated that the synthesized AZO and GZO possesses mid-infrared LSPR peaks with a quality factor comparable to ITO which make them a cost-effective and earth-abundant substitution of ITO. In addition, due to the dopant atom size difference, the doping profile of IZO is completely different from AZO and GZO. The etching experiment shows that a significant amount of In dopants are segregated on the surface which prevent IZO nanocrystals from exhibiting plasmonic properties.

In chapter 5, we show for the first time, that the deep subwavelength confinement of low energy infrared light (4200 to 2600 cm^{-1}) by plasmonic nanocrystals can accelerate aheterogeneous chemical process. We specifically use time-dependent infrared spectroscopy to quantify the increase in desorption rate for two model molecules upon mid-infrared light illumination of indium tin oxide (ITO) nanocrystal thin films. Whereas the majority of plasmonic literature focuses on ultraviolet/visible plasmons, we demonstrate that low energy plasmons also have the potential to manipulate chemical processes. This initial work is likely to motivate further studies of low energy plasmon-molecule coupling on the nanomaterial surface

Overall, the major contributions of the surface chemical studies on plasmonic metal oxides are as follows. First, colloidal synthesized metal oxide nanocrystals exhibiting near- to mid- infrared LSPRs are compelling materials for applications of plasmonics. The dynamic modulation of carrier density via redox reactions provides an extra degree of freedom to design

these materials. Second, this work brings attention to low-energy LSPRs and their coupling with surface adsorbates. The unique focusing capability of LSPRs may bring a new route to utilizing mid-infrared photons.

6.1 Outlook

6.1.1 Mechanism study for LSPR enhanced reaction

The observed molecular desorption enhancement makes it clear that LSPRs well outside of the ultraviolet/visible can also affect chemistry. We anticipate new opportunities, like local energy delivery or bond-selective chemistry, will emerge as underlying mechanisms of this nature become better understood and controlled. Although molecular desorption is a great starting point because it only involves one energy barrier, some of the parameters are difficult to control using this setup. For example, we can hardly quantify the beacon molecule deposited on the film which results in multilayer desorption. In addition, since the whole process runs in an ambient environment, we cannot vary temperature and pressure to evaluate their impact. A new reaction system is needed for further mechanism study. The trimethylaluminum (TMA) reaction with surface hydroxyl groups is recommended for this study. Being the major reaction for Al_2O_3 atomic layer deposition (ALD), it is well-studied on various surfaces.[146-150] More importantly, the deposition has been applied to colloidal synthesized ITO nanocrystals successfully.[151] Initial results were collected in the DRIFTS reaction cell in the lab. The reaction is carried out on a spin-cast ITO nanocrystal film with deposition conditions shown in Figure 6.2 (a). Similar to annealing experiments, the precursors are delivered through a MFC or manually-controlled valve. After each pulse, an IR spectrum is collected to quantitatively trace the reaction process. Particularly, the characteristic peaks of C-H stretches in between 2800 – 3000 cm^{-1} are used to

quantify the surface coverage. However, the reaction is carried out too fast even we are running this reaction at room temperature (Figure 6.2 (b)). In addition, the pumping speed of the rotary pump is not high enough to eliminate signatures of physisorbed water. For further study, I would suggest this reaction be carried out in the ultra-high vacuum chamber coupling with sub-mTorr dosing which alleviate the issues encountered in the DRIFTS reaction cell. By controlling whether particles are on resonance or off-resonance with the reactant molecular vibrations, it is possible to elucidate the athermal component in the surface chemistry enhancing mechanism.

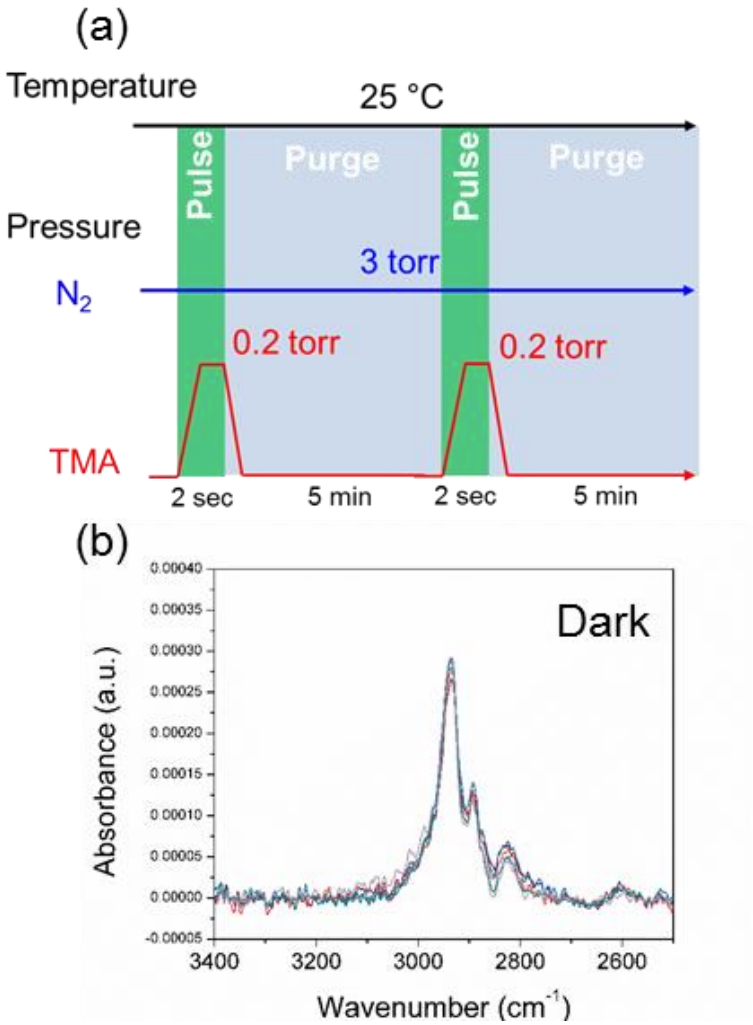

Figure 6.2. (a) Reaction conditions for TMA pulse experiment. The carrier gas N2 flows continuous at 3 torr. TMA is pulsed with 2 seconds with partial pressure up to 0.2 torr. Between

each pulse, 5 minutes' purging allow all the TMA gas to be pumped out. Characteristic IR peak of C-H stretches after each pulse under dark environment.

6.1.2 Core-shell structure

It would be beneficial to couple more light into a single nanocrystal for local energy delivery applications. Theoretical calculations have demonstrated hundreds of degrees temperature increase upon excitation in a multi-shell nanoparticle.[152] A multilayer nanoparticle with each layer exhibiting different LSPR energies may amplify this temperature rise by many folds. There have been many demonstrations of colloidal synthesized core-shell nanostructures in noble metals[153-154] and metal oxides.[155] A multi-stage injection method to supply different precursors along nanocrystal growth may provide a possible route to synthesize these materials. Consequently, new nanocrystal-based growth chemistries with additional plasmonic layers will improve the LSPR enhancement on surface chemistries.

REFERENCES

1. Willets, K. A.; Van Duyne, R. P., Localized Surface Plasmon Resonance Spectroscopy and Sensing. *Annu. Rev. Phys. Chem.* **2007**, *58*, 267-297.

2. Kerker, M.; Wang, D. S.; Chew, H., Surface Enhanced Raman-Scattering (Sers) by Molecules Adsorbed at Spherical-Particles. *Appl. Opt.* **1980**, *19*, 3373-3388.

3. Wang, D. S.; Kerker, M., Enhanced Raman-Scattering by Molecules Adsorbed at the Surface of Colloidal Spheroids. *Phys. Rev. B* **1981**, *24*, 1777-1790.

4. Stiles, P. L.; Dieringer, J. A.; Shah, N. C.; Van Duyne, R. R., Surface-Enhanced Raman Spectroscopy. *Annual Review of Analytical Chemistry* **2008**, *1*, 601-626.

5. Kneipp, K.; Kneipp, H.; Itzkan, I.; Dasari, R. R.; Feld, M. S., Surface-Enhanced Raman Scattering: A New Tool for Biomedical Spectroscopy. *Current Science* **1999**, *77*, 915-924.

6. Stuart, D. A.; Yonzon, C. R.; Zhang, X. Y.; Lyandres, O.; Shah, N. C.; Glucksberg, M. R.; Walsh, J. T.; Van Duyne, R. P., Glucose Sensing Using near-Infrared Surface-Enhanced Raman Spectroscopy: Gold Surfaces, 10-Day Stability, and Improved Accuracy. *Anal. Chem.* **2005**, *77*, 4013-4019.

7. Braun, G.; Lee, S. J.; Dante, M.; Nguyen, T. Q.; Moskovits, M.; Reich, N., Surface-Enhanced Raman Spectroscopy for DNA Detection by Nanoparticle Assembly onto Smooth Metal Films. *J. Am. Chem. Soc.* **2007**, *129*, 6378-+.

8. Vo-Dinh, T.; Yan, F.; Wabuyele, M. B., Surface-Enhanced Raman Scattering for Biomedical Diagnostics and Molecular Imaging. *Surface-Enhanced Raman Scattering: Physics and Applications* **2006**, *103*, 409-426.

9. Nie, S. M.; Emery, S. R., Probing Single Molecules and Single Nanoparticles by Surface-Enhanced Raman Scattering. *Science* **1997**, *275*, 1102-1106.

10. Kneipp, K.; Wang, Y.; Kneipp, H.; Perelman, L. T.; Itzkan, I.; Dasari, R.; Feld, M. S., Single Molecule Detection Using Surface-Enhanced Raman Scattering (Sers). *Phys. Rev. Lett.* **1997**, *78*, 1667-1670.

11. Prinz, J.; Heck, C.; Ellerik, L.; Merk, V.; Bald, I., DNA Origami Based Au-Ag-Core-Shell Nanoparticle Dimers with Single-Molecule Sers Sensitivity. *Nanoscale* **2016**, *8*, 5612-5620.

12. Zhao, J.; Das, A.; Zhang, X. Y.; Schatz, G. C.; Sligar, S. G.; Van Duyne, R. P., Resonance Surface Plasmon Spectroscopy: Low Molecular Weight Substrate Binding to Cytochrome P450. *J. Am. Chem. Soc.* **2006**, *128*, 11004-11005.

13. Haes, A. J.; Chang, L.; Klein, W. L.; Van Duyne, R. P., Detection of a Biomarker for Alzheimer's Disease from Synthetic and Clinical Samples Using a Nanoscale Optical Biosensor. *J. Am. Chem. Soc.* **2005**, *127*, 2264-2271.

14. Haes, A. J.; Zou, S. L.; Zhao, J.; Schatz, G. C.; Van Duyne, R. P., Localized Surface Plasmon Resonance Spectroscopy near Molecular Resonances. *J. Am. Chem. Soc.* **2006**, *128*, 10905-10914.

15. Liu, N.; Tang, M. L.; Hentschel, M.; Giessen, H.; Alivisatos, A. P., Nanoantenna-Enhanced Gas Sensing in a Single Tailored Nanofocus. *Nat. Mater.* **2011**, *10*, 631-636.

16. Kazuma, E. J., J; Ueba, H; Trenary, M; Kim, Y, Real-Space and Real-Time Observation of a Plasmon-Induced Chemical Reaction of a Single Molecule. *Science* **2018**, *360*, 521-526.

17. Thimsen, E.; Le Formal, F.; Gratzel, M.; Warren, S. C., Influence of Plasmonic Au Nanoparticles on the Photoactivity of Fe2o3 Electrodes for Water Splitting. *Nano Lett.* **2011**, *11*, 35-43.

18. Liu, Z. W.; Hou, W. B.; Pavaskar, P.; Aykol, M.; Cronin, S. B., Plasmon Resonant Enhancement of Photocatalytic Water Splitting under Visible Illumination. *Nano Lett.* **2011**, *11*, 1111-1116.

19. Ingram, D. B.; Linic, S., Water Splitting on Composite Plasmonic-Metal/Semiconductor Photoelectrodes: Evidence for Selective Plasmon-Induced Formation of Charge Carriers near the Semiconductor Surface. *J. Am. Chem. Soc.* **2011**, *133*, 5202-5205.

20. Mukherjee, S.; Zhou, L.; Goodman, A. M.; Large, N.; Ayala-Orozco, C.; Zhang, Y.; Nordlander, P.; Halas, N. J., Hot-Electron-Induced Dissociation of H_2 on Gold Nanoparticles Supported on Sio_2. *J. Am. Chem. Soc.* **2014**, *136*, 64-67.

21. Christopher, P.; Xin, H. L.; Marimuthu, A.; Linic, S., Singular Characteristics and Unique Chemical Bond Activation Mechanisms of Photocatalytic Reactions on Plasmonic Nanostructures. *Nat. Mater.* **2012**, *11*, 1044-1050.

22. Christopher, P.; Xin, H.; Linic, S., Visible-Light-Enhanced Catalytic Oxidation Reactions on Plasmonic Silver Nanostructures. *Nat. Mater.* **2011**, *3*, 467-472.

23. Zhang, X.; Li, X. Q.; Zhang, D.; Su, N. Q.; Yang, W. T.; Everitt, H. O.; Liu, J., Product Selectivity in Plasmonic Photocatalysis for Carbon Dioxide Hydrogenation. *Nature Communications* **2017**, *8*, 1-9.

24. Boerigter, C.; Campana, R.; Morabito, M.; Linic, S., Evidence and Implications of Direct Charge Excitation as the Dominant Mechanism in Plasmon-Mediated Photocatalysis. *Nature Communications* **2016**, *7*.

25. Boerigter, C.; Aslam, U.; Linic, S., Mechanism of Charge Transfer from Plasmonic Nanostructures to Chemically Attached Materials. *Acs Nano* **2016**, *10*, 6108-6115.

26. Snapshot of Global Photovoltaic Markets. *International Energy Agency* **2017**.

27. Atwater, H. A.; Polman, A., Plasmonics for Improved Photovoltaic Devices. *Nat. Mater.* **2010**, *9*, 205-213.

28. Zhou, Z. G.; Kong, B.; Yu, C.; Shi, X. Y.; Wang, M. W.; Liu, W.; Sun, Y. A.; Zhang, Y. J.; Yang, H.; Yang, S. P., Tungsten Oxide Nanorods: An Efficient Nanoplatform for Tumor Ct Imaging and Photothermal Therapy. *Scientific Reports* **2014**, *4*.

29. Liu, Q.; Sun, C. Y.; He, Q.; Liu, D. B.; Khalil, A.; Xiang, T.; Wu, Z. Y.; Wang, J.; Song, L., Ultrathin Carbon Layer Coated Moo2 Nanoparticles for High-Performance near-Infrared Photothermal Cancer Therapy. *Chem. Commun.* **2015**, *51*, 10054-10057.

30. Abb, M.; Wang, Y. D.; Papasimakis, N.; de Groot, C. H.; Muskens, O. L., Surface-Enhanced Infrared Spectroscopy Using Metal Oxide Plasmonic Antenna Arrays. *Nano Lett.* **2014**, *14*, 346-352.

31. Tervo, E. J.; Boyuk, D. S.; Cola, B. A.; Zhang, Z. M. M.; Filler, M. A., Sub-Diffractional Waveguiding by Mid-Infrared Plasmonic Resonators in Semiconductor Nanowires. *Nanoscale* **2018**, *10*, 5708-5716.

32. Boriskina, S. V.; Tong, J. K.; Huang, Y.; Zhou, J. W.; Chiloyan, V.; Chen, G., Enhancement and Tunability of near-Field Radiative Heat Transfer Mediated by Surface Plasmon Polaritons in Thin Plasmonic Films. *Photonics* **2015**, *2*, 659-683.

33. van der Stam, W.; Berends, A. C.; Donega, C. D., Prospects of Colloidal Copper Chalcogenide Nanocrystals. *Chemphyschem* **2016**, *17*, 559-581.

34. Coughlan, C.; Ibanez, M.; Dobrozhan, O.; Singh, A.; Cabot, A.; Ryan, K. M., Compound Copper Chalcogenide Nanocrystals. *Chem. Rev.* **2017**, *117*, 5865-6109.

35. Zhang, H.; Kulkarni, V.; Prodan, E.; Nordlander, P.; Govorov, A. O., Theory of Quantum Plasmon Resonances in Doped Semiconductor Nanocrystals. *Journal of Physical Chemistry C* **2014**, *118*, 16035-16042.

36. Shen, G. H.; Guyot-Sionnest, P., Hgs and Hgs/Cds Colloidal Quantum Dots with Infrared Intraband Transitions and Emergence of a Surface Plasmon. *Journal of Physical Chemistry C* **2016**, *120*, 11744-11753.

37. Dorfs, D.; Hartling, T.; Miszta, K.; Bigall, N. C.; Kim, M. R.; Genovese, A.; Falqui, A.; Povia, M.; Manna, L., Reversible Tunability of the near-Infrared Valence Band Plasmon Resonance in $Cu_{2-X}se$ Nanocrystals. *J. Am. Chem. Soc.* **2011**, *133*, 11175-11180.

38. Naik, G. V.; Schroeder, J. L.; Ni, X. J.; Kildishev, A. V.; Sands, T. D.; Boltasseva, A., Titanium Nitride as a Plasmonic Material for Visible and near-Infrared Wavelengths. *Optical Materials Express* **2012**, *2*, 478-489.

39. Mahboob, I.; Veal, T. D.; McConville, C. F.; Lu, H.; Schaff, W. J., Intrinsic Electron Accumulation at Clean Inn Surfaces. *Phys. Rev. Lett.* **2004**, *92*.

40. Liu, Z. H.; Beaulac, R., Nature of the Infrared Transition of Colloidal Indium Nitride Nanocrystals: Nonparabolicity Effects on the Plasmonic Behavior of Doped Semiconductor Nanomaterials. *Chem. Mater.* **2017**, *29*, 7507-7514.

41. Chou, L.-W.; Shin, N.; Sivaram, S. V.; Filler, M. A., Tunable Mid-Infrared Localized Surface Plasmon Resonances in Silicon Nanowires. *J. Am. Chem. Soc.* **2012**, *134*, 16155-16158.

42. Chou, L.-W.; Filler, M. A., Engineering Multimodal Localized Surface Plasmon Resonances in Silicon Nanowires. *Angewandte Chemie-International Edition* **2013**, *52*, 8079-8083.

43. Zhang, H.; Zhang, R. M.; Schramke, K. S.; Bedford, N. M.; Hunter, K.; Kortshagen, U. R.; Nordlander, P., Doped Silicon Nanocrystal Plasmonics. *Acs Photonics* **2017**, *4*, 963-970.

44. Rowe, D. J.; Jeong, J. S.; Mkhoyan, K. A.; Kortshagen, U. R., Phosphorus-Doped Silicon Nanocrystals Exhibiting Mid-Infrared Localized Surface Plasmon Resonance. *Nano Lett.* **2013**, *13*, 1317-1322.

45. Kramer, N. J.; Schramke, K. S.; Kortshagen, U. R., Plasmonic Properties of Silicon Nanocrystals Doped with Boron and Phosphorus. *Nano Lett.* **2015**, *15*, 5597-5603.

46. Huang, Q. Q.; Hu, S.; Zhuang, J.; Wang, X., Moo3-X-Based Hybrids with Tunable Localized Surface Plasmon Resonances: Chemical Oxidation Driving Transformation from Ultrathin Nanosheets to Nanotubes. *Chemistry-a European Journal* **2012**, *18*, 15283-15287.

47. Manthiram, K.; Alivisatos, A. P., Tunable Localized Surface Plasmon Resonances in Tungsten Oxide Nanocrystals. *J. Am. Chem. Soc.* **2012**, *134*, 3995-3998.

48. Ye, X. C.; Hickey, D. R.; Fei, J. Y.; Diroll, B. T.; Paik, T.; Chen, J.; Murray, C. B., Seeded Growth of Metal-Doped Plasmonic Oxide Heterodimer Nanocrystals and Their Chemical Transformation. *J. Am. Chem. Soc.* **2014**, *136*, 5106-5115.

49. Kanehara, M.; Koike, H.; Yoshinaga, T.; Teranishi, T., Indium Tin Oxide Nanoparticles with Compositionally Tunable Surface Plasmon Resonance Frequencies in the near-Ir Region. *J. Am. Chem. Soc.* **2009**, *131*, 17736-17737.

50. Choi, S.-I.; Nam, K. M.; Park, B. K.; Seo, W. S.; Park, J. T., Preparation and Optical Properties of Colloidal, Monodisperse, and Highly Crystalline Ito Nanoparticles. *Chem. Mater.* **2008**, *20*, 2609-2611.

51. Buonsanti, R.; Llordes, A.; Aloni, S.; Helms, B. A.; Milliron, D. J., Tunable Infrared Absorption and Visible Transparency of Colloidal Aluminum-Doped Zinc Oxide Nanocrystals. *Nano Lett.* **2011**, *11*, 4706-4710.

52. Della Gaspera, E.; Chesman, A. S. R.; van Embden, J.; Jasieniak, J. J., Non-Injection Synthesis of Doped Zinc Oxide Plasmonic Nanocrystals. *Acs Nano* **2014**, *8*, 9154-9163.

53. Gilstrap, R. A., Jr.; Capozzi, C. J.; Carson, C. G.; Gerhardt, R. A.; Summers, C. J., Synthesis of a Nonagglomerated Indium Tin Oxide Nanoparticle Dispersion. *Adv. Mater.* **2008**, *20*, 4163-4166.

54. Zhang, Z. H.; Lu, M. H.; Xu, H. R.; Chin, W. S., Shape-Controlled Synthesis of Zinc Oxide: A Simple Method for the Preparation of Metal Oxide Nanocrystals in Non-Aqueous Medium. *Chemistry-a European Journal* **2007**, *13*, 632-638.

55. Frank, G.; Kostlin, H., Electrical-Properties and Defect Model of Tin-Doped Indium Oxide Layers. *Appl. Phys. A: Mater. Sci. Process.* **1982**, *27*, 197-206.

56. Mattox, T. M.; Bergerud, A.; Agrawal, A.; Milliron, D. J., Influence of Shape on the Surface Plasmon Resonance of Tungsten Bronze Nanocrystals. *Chem. Mater.* **2014**, *26*, 1779-1784.

57. Jain, P. K.; Manthiram, K.; Engel, J. H.; White, S. L.; Faucheaux, J. A.; Alivisatos, A. P., Doped Nanocrystals as Plasmonic Probes of Redox Chemistry. *Angewandte Chemie-International Edition* **2013**, *52*, 13671-13675.

58. Mendelsberg, R. J.; McBride, P. M.; Duong, J. T.; Bailey, M. J.; Llordes, A.; Milliron, D. J.; Helms, B. A., Dispersible Plasmonic Doped Metal Oxide Nanocrystal Sensors That Optically Track Redox Reactions in Aqueous Media with Single-Electron Sensitivity. *Advanced Optical Materials* **2015**, *3*, 1293-1300.

59. Garcia, G.; Buonsanti, R.; Runnerstrom, E. L.; Mendelsberg, R. J.; Llordes, A.; Anders, A.; Richardson, T. J.; Milliron, D. J., Dynamically Modulating the Surface Plasmon Resonance of Doped Semiconductor Nanocrystals. *Nano Lett.* **2011**, *11*, 4415-4420.

60. Llordes, A.; Garcia, G.; Gazquez, J.; Milliron, D. J., Tunable near-Infrared and Visible-Light Transmittance in Nanocrystal-in-Glass Composites. *Nature* **2013**, *500*, 323-+.

61. Fujishima, A.; Honda, K., Electrochemical Photolysis of Water at a Semiconductor Electrode. *Nature* **1972**, *238*, 37-+.

62. Haase, M.; Weller, H.; Henglein, A., Photochemistry and Radiation-Chemistry of Colloidal Semiconductors .23. Electron Storage on Zno Particles and Size Quantization. *J. Phys. Chem.* **1988**, *92*, 482-487.

63. Schimpf, A. M.; Lounis, S. D.; Runnerstrom, E. L.; Milliron, D. J.; Gamelin, D. R., Redox Chemistries and Plasmon Energies of Photodoped In_2O_3 and Sn-Doped In_2O_3 (Ito) Nanocrystals. *J. Am. Chem. Soc.* **2015**, *137*, 518-524.

64. Agrawal, A.; Cho, S. H.; Zandi, O.; Ghosh, S.; Johns, R. W.; Milliron, D. J., Localized Surface Plasmon Resonance in Semiconductor Nanocrystals. *Chem. Rev.* **2018**, *118*, 3121-3207.

65. Jansons, A. W.; Plummer, L. K.; Hutchison, J. E., Living Nanocrystals. *Chem. Mater.* **2017**, *29*, 5415-5425.

66. Rand, B. P.; Peumans, P.; Forrest, S. R., Long-Range Absorption Enhancement in Organic Tandem Thin-Film Solar Cells Containing Silver Nanoclusters. *J. Appl. Phys.* **2004**, *96*, 7519-7526.

67. Kim, S. S.; Na, S. I.; Jo, J.; Kim, D. Y.; Nah, Y. C., Plasmon Enhanced Performance of Organic Solar Cells Using Electrodeposited Ag Nanoparticles. *Appl. Phys. Lett.* **2008**, *93*.

68. Morfa, A. J.; Rowlen, K. L.; Reilly, T. H.; Romero, M. J.; van de Lagemaat, J., Plasmon-Enhanced Solar Energy Conversion in Organic Bulk Heterojunction Photovoltaics. *Appl. Phys. Lett.* **2008**, *92*.

69. Hagglund, C.; Zach, M.; Petersson, G.; Kasemo, B., Electromagnetic Coupling of Light into a Silicon Solar Cell by Nanodisk Plasmons. *Appl. Phys. Lett.* **2008**, *92*.

70. Jensen, T. R.; Van Duyne, R. P.; Johnson, S. A.; Maroni, V. A., Surface-Enhanced Infrared Spectroscopy: A Comparison of Metal Island Films with Discrete and Nondiscrete Surface Plasmons. *Appl. Spectrosc.* **2000**, *54*, 371-377.

71. Shimizu, K. T.; Woo, W. K.; Fisher, B. R.; Eisler, H. J.; Bawendi, M. G., Surface-Enhanced Emission from Single Semiconductor Nanocrystals. *Phys. Rev. Lett.* **2002**, *89*.

72. Chen, X.; Zhu, H. Y.; Zhao, J. C.; Zheng, Z. T.; Gao, X. P., Visible-Light-Driven Oxidation of Organic Contaminants in Air with Gold Nanoparticle Catalysts on Oxide Supports. *Angew. Chem. Int. Ed.* **2008**, *47*, 5353-5356.

73. Zheng, Z.; Tachikawa, T.; Majima, T., Single-Particle Study of Pt-Modified Au Nanorods for Plasmon-Enhanced Hydrogen Generation in Visible to near-Infrared Region. *J. Am. Chem. Soc.* **2014**, *136*, 6870-6873.

74. Shim, M.; Guyot-Sionnest, P., N-Type Colloidal Semiconductor Nanocrystals. *Nature* **2000**, *407*, 981-983.

75. Wang, C. J.; Shim, M.; Guyot-Sionnest, P., Electrochromic Nanocrystal Quantum Dots. *Science* **2001**, *291*, 2390-2392.

76. Liu, W. K.; Whitaker, K. M.; Kittilstved, K. R.; Gamelin, D. R., Stable Photogenerated Carriers in Magnetic Semiconductor Nanocrystals. *J. Am. Chem. Soc.* **2006**, *128*, 3910-3911.

77. Luther, J. M.; Jain, P. K.; Ewers, T.; Alivisatos, A. P., Localized Surface Plasmon Resonances Arising from Free Carriers in Doped Quantum Dots. *Nat. Mater.* **2011**, *10*, 361-366.

78. Diroll, B. T.; Gordon, T. R.; Gaulding, E. A.; Klein, D. R.; Paik, T.; Yun, H. J.; Goodwin, E. D.; Damodhar, D.; Kagan, C. R.; Murray, C. B., Synthesis of N-Type Plasmonic Oxide Nanocrystals and the Optical and Electrical Characterization of Their Transparent Conducting Films. *Chem. Mater.* **2014**, *26*, 4579-4588.

79. Hwang, J. H.; Edwards, D. D.; Kammler, D. R.; Mason, T. O., Point Defects and Electrical Properties of Sn-Doped in-Based Transparent Conducting Oxides. *Solid State Ionics* **2000**, *129*, 135-144.

80. Yamada, N.; Yasui, I.; Shigesato, Y.; Li, H. L.; Ujihira, Y.; Nomura, K., Donor Compensation and Carrier-Transport Mechanisms in Tin-Doped In_2O_3 Films Studied by Means of Conversion Electron ^{119}sn Mossbauer Spectroscopy and Hall Effect Measurements. *Jpn. J. Appl. Phys., Part 1* **2000**, *39*, 4158-4163.

81. Gonzalez, G. B.; Mason, T. O.; Quintana, J. P.; Warschkow, O.; Ellis, D. E.; Hwang, J. H.; Hodges, J. P.; Jorgensen, J. D., Defect Structure Studies of Bulk and Nano-Indium-Tin Oxide. *J. Appl. Phys.* **2004**, *96*, 3912-3920.

82. Kanai, Y., Electrical-Properties of In2o3 Single-Crystals Doped with Metallic Donor Impurity. *Jpn. J. Appl. Phys., Part 1* **1984**, *23*, 127-127.

83. Lounis, S. D.; Runnerstrom, E. L.; Bergerud, A.; Nordlund, D.; Milliron, D. J., Influence of Dopant Distribution on the Plasmonic Properties of Indium Tin Oxide Nanocrystals. *J. Am. Chem. Soc.* **2014**, *136*, 7110-7116.

84. Carey, G. F.; Finlayson, B. A., Orthogonal Collocation on Finite-Elements. *Chem. Eng. Sci.* **1975**, *30*, 587-596.

85. Cresswell, W. R. P. a. D. L., A Simple Method for the Calculation of Effectiveness Factors. *Chem. Eng. Sci.* **1971**, *16*, 605-616.

86. Tolle, P. T. B. a. J. W., Sequential Quadratic Programming. *Acta Numerica* **1995**, *4*, 1-51.

87. Warschkow, O.; Ellis, D. E.; Gonzalez, G. B.; Mason, T. O., Defect Structures of Tin-Doped Indium Oxide. *J. Am. Ceram. Soc.* **2003**, *86*, 1700-1706.

88. Aris, R., On Shape Factors for Irregular Particles .1. The Steady State Problem - Diffusion and Reaction. *Chem. Eng. Sci.* **1957**, *6*, 262-268.

89. Link, S.; El-Sayed, M. A., Spectral Properties and Relaxation Dynamics of Surface Plasmon Electronic Oscillations in Gold and Silver Nanodots and Nanorods. *J. Phys. Chem. B* **1999**, *103*, 8410-8426.

90. Preissler, N.; Bierwagen, O.; Ramu, A. T.; Speck, J. S., Electrical Transport, Electrothermal Transport, and Effective Electron Mass in Single-Crystalline In2o3 Films. *Phys. Rev. B* **2013**, *88*.

91. Berger, J.; Riess, I.; Tannhauser, D. S., Dynamic Measurement of Oxygen Diffusion in Indium-Tin Oxide. *Solid State Ionics* **1985**, *15*, 225-231.

92. Wirtz, G. P.; Takiar, H. P., Oxygen Diffusion in Vapor-Deposited Indium Oxide-Films. *J. Am. Ceram. Soc.* **1981**, *64*, 748-752.

93. Komeda, T.; Kim, Y.; Kawai, M.; Persson, B. N. J.; Ueba, H., Lateral Hopping of Molecules Induced by Excitation of Internal Vibration Mode. *Science* **2002**, *295*, 2055-2058.

94. Killelea, D. R.; Campbell, V. L.; Shuman, N. S.; Utz, A. L., Bond-Selective Control of a Heterogeneously Catalyzed Reaction. *Science* **2008**, *319*, 790-793.

95. Pascual, J. I.; Lorente, N.; Song, Z.; Conrad, H.; Rust, H. P., Selectivity in Vibrationally Mediated Single-Molecule Chemistry. *Nature* **2003**, *423*, 525-528.

96. Kim, Z. H.; Bechtel, H. A.; Zare, R. N., Vibrational Control in the Reaction of Methane with Atomic Chlorine. *J. Am. Chem. Soc.* **2001**, *123*, 12714-12715.

97. Noda, I., Two-Dimensional Infrared-Spectroscopy. *J. Am. Chem. Soc.* **1989**, *111*, 8116-8118.

98. Hartstein, A.; Kirtley, J. R.; Tsang, J. C., Enhancement of the Infrared-Absorption from Molecular Monolayers with Thin Metal Overlayers. *Phys. Rev. Lett.* **1980**, *45*, 201-204.

99. Law, S.; Podolskiy, V.; Wasserman, D., Towards Nano-Scale Photonics with Micro-Scale Photons: The Opportunities and Challenges of Mid-Infrared Plasmonics. *Nanophotonics* **2013**, *2*, 103-130.

100. Kriegel, I.; Jiang, C. Y.; Rodriguez-Fernandez, J.; Schaller, R. D.; Talapin, D. V.; da Como, E.; Feldmann, J., Tuning the Excitonic and Plasmonic Properties of Copper Chalcogenide Nanocrystals. *J. Am. Chem. Soc.* **2012**, *134*, 1583-1590.

101. De Trizio, L.; Buonsanti, R.; Schimpf, A. M.; Llordes, A.; Gamelin, D. R.; Simonutti, R.; Milliron, D. J., Nb-Doped Colloidal Tio2 Nanocrystals with Tunable Infrared Absorption. *Chem. Mater.* **2013**, *25*, 3383-3390.

102. Liang, X. Y., et al., Colloidal Indium-Doped Zinc Oxide Nanocrystals with Tunable Work Function: Rational Synthesis and Optoelectronic Applications. *Chem. Mater.* **2014**, *26*, 5169-5178.

103. Ghosh, S.; Saha, M.; De, S. K., Tunable Surface Plasmon Resonance and Enhanced Electrical Conductivity of in Doped Zno Colloidal Nanocrystals. *Nanoscale* **2014**, *6*, 7039-7051.

104. Saha, M.; Ghosh, S.; Ashok, V. D.; De, S. K., Carrier Concentration Dependent Optical and Electrical Properties of Ga Doped Zno Hexagonal Nanocrystals. *PCCP* **2015**, *17*, 16067-16079.

105. Runnerstrom, E. L.; Bergerud, A.; Agrawal, A.; Johns, R. W.; Dahlman, C. J.; Singh, A.; Selbach, S. M.; Milliron, D. J., Defect Engineering in Plasmonic Metal Oxide Nanocrystals. *Nano Lett.* **2016**, *16*, 3390-3398.

106. Johns, R. W.; Bechtel, H. A.; Runnerstrom, E. L.; Agrawal, A.; Lounis, S. D.; Milliron, D. J., Direct Observation of Narrow Mid-Infrared Plasmon Linewidths of Single Metal Oxide Nanocrystals. *Nature Communications* **2016**, *7*.

107. Drouilly, C.; Krafft, J. M.; Averseng, F.; Casale, S.; Bazer-Bachi, D.; Chizallet, C.; Lecocq, V.; Vezin, H.; Lauron-Pernot, H.; Costentin, G., Zno Oxygen Vacancies Formation and Filling Followed by in Situ Photoluminescence and in Situ Epr. *Journal of Physical Chemistry C* **2012**, *116*, 21297-21307.

108. Liu, L. S.; Mei, Z. X.; Tang, A. H.; Azarov, A.; Kuznetsov, A.; Xue, Q. K.; Du, X. L., Oxygen Vacancies: The Origin of N-Type Conductivity in Zno. *Phys. Rev. B* **2016**, *93*.

109. Tu, Y.; Chen, S. Q.; Li, X.; Gorbaciova, J.; Gillin, W. P.; Krause, S.; Briscoe, J., Control of Oxygen Vacancies in Zno Nanorods by Annealing and Their Influence on Zno/Pedot:Pss Diode Behaviour. *Journal of Materials Chemistry C* **2018**, *6*, 1815-1821.

110. Hu, W. Z.; Guo, S. W.; Gaul, J. P.; Boebinger, M. G.; McDowell, M. T.; Filler, M. A., Reversible Tuning of the Surface Plasmon Resonance of Indium Tin Oxide Nanocrystals by Gas-Phase Oxidation and Reduction. *Journal of Physical Chemistry C* **2017**, *121*, 15970-15976.

111. Hoffmann, M. R.; Martin, S. T.; Choi, W. Y.; Bahnemann, D. W., Environmental Applications of Semiconductor Photocatalysis. *Chem. Rev.* **1995**, *95*, 69-96.

112. Linsebigler, A. L.; Lu, G. Q.; Yates, J. T., Photocatalysis on Tio2 Surfaces - Principles, Mechanisms, and Selected Results. *Chem. Rev.* **1995**, *95*, 735-758.

113. Ciesla, P.; Kocot, P.; Mytych, P.; Stasicka, Z., Homogeneous Photocatalysis by Transition Metal Complexes in the Environment. *Journal of Molecular Catalysis a-Chemical* **2004**, *224*, 17-33.

114. Kudo, A.; Miseki, Y., Heterogeneous Photocatalyst Materials for Water Splitting. *Chem. Soc. Rev.* **2009**, *38*, 253-278.

115. Cao, L. Y.; Barsic, D. N.; Guichard, A. R.; Brongersma, M. L., Plasmon-Assisted Local Temperature Control to Pattern Individual Semiconductor Nanowires and Carbon Nanotubes. *Nano Lett.* **2007**, *7*, 3523-3527.

116. Baffou, G.; Quidant, R.; de Abajo, F. J. G., Nanoscale Control of Optical Heating in Complex Plasmonic Systems. *Acs Nano* **2010**, *4*, 709-716.

117. Kou, J. H.; Lu, C. H.; Wang, J.; Chen, Y. K.; Xu, Z. Z.; Varma, R. S., Selectivity Enhancement in Heterogeneous Photocatalytic Transformations. *Chem. Rev.* **2017**, *117*, 1445-1514.

118. Yoon, S.; Holiday, R. J.; Crim, F. F., Control of Bimolecular Reactions: Bond-Selected Reaction of Vibrationally Excited Ch3d with Cl(P-2(3/2)). *J. Chem. Phys.* **2003**, *119*, 4755-4761.

119. Yan, S.; Wu, Y. T.; Zhang, B. L.; Yue, X. F.; Liu, K. P., Do Vibrational Excitations of Chd3 Preferentially Promote Reactivity toward the Chlorine Atom? *Science* **2007**, *316*, 1723-1726.

120. Hussla, I.; Seki, H.; Chuang, T. J.; Gortel, Z. W.; Kreuzer, H. J.; Piercy, P., Infrared-Laser-Induced Photodesorption of Nh3 and Nd3 Adsorbed on Single-Crystal Cu(100) and Ag Film. *Phys. Rev. B* **1985**, *32*, 3489-3501.

121. Heidberg, J.; Stein, H.; Riehl, E., Resonance, Rate, and Quantum Yield of Infrared-Laser-Induced Desorption by Multiquantum Vibrational-Excitation of the Adsorbate Ch3f on Nacl. *Phys. Rev. Lett.* **1982**, *49*, 666-669.

122. Redlich, B.; Zacharias, H.; Meijer, G.; von Helden, G., Resonant Infrared Laser-Induced Desorption of Methane Condensed on Nacl(100): Isotope Mixture Experiments. *J. Chem. Phys.* **2006**, *124*.

123. Focsa, C.; Mihesan, C.; Ziskind, M.; Chazallon, B.; Therssen, E.; Desgroux, P.; Destombes, J. L., Wavelength-Selective Vibrationally Excited Photodesorption with Tunable Ir Sources. *Journal of Physics-Condensed Matter* **2006**, *18*, S1357-S1387.

124. Furube, A.; Yoshinaga, T.; Kanehara, M.; Eguchi, M.; Teranishi, T., Electric-Field Enhancement Inducing near-Infrared Two-Photon Absorption in an Indium-Tin Oxide Nanoparticle Film. *Angewandte Chemie-International Edition* **2012**, *51*, 2640-2642.

125. Lee, S. H.; Nishi, H.; Tatsuma, T., Plasmonic Behaviour and Plasmon-Induced Charge Separation of Nanostructured Moo3-X under near Infrared Irradiation. *Nanoscale* **2018**, *10*, 2841-2847.

126. Clavero, C., Plasmon-Induced Hot-Electron Generation at Nanoparticle/Metal-Oxide Interfaces for Photovoltaic and Photocatalytic Devices. *Nature Photonics* **2014**, *8*, 95-103.

127. Kang, Y. M.; Gong, Y. J.; Hu, Z. J.; Li, Z. W.; Qiu, Z. W.; Zhu, X.; Ajayan, P. M.; Fang, Z. Y., Plasmonic Hot Electron Enhanced Mos2 Photocatalysis in Hydrogen Evolution. *Nanoscale* **2015**, *7*, 4482-4488.

128. Neumann, O.; Urban, A. S.; Day, J.; Lal, S.; Nordlander, P.; Halas, N. J., Solar Vapor Generation Enabled by Nanoparticles. *Acs Nano* **2013**, *7*, 42-49.

129. Zhou, L.; Tan, Y. L.; Wang, J. Y.; Xu, W. C.; Yuan, Y.; Cai, W. S.; Zhu, S. N.; Zhu, J., 3d Self-Assembly of Aluminium Nanoparticles for Plasmon-Enhanced Solar Desalination. *Nature Photonics* **2016**, *10*, 393-+.

130. Agrawal, A.; Johns, R. W.; Milliron, D. J., Control of Localized Surface Plasmon Resonances in Metal Oxide Nanocrystals. *Annual Review of Materials Research, Vol 47* **2017**, *47*, 1-31.

131. Lounis, S. D.; Runnerstrorm, E. L.; Llordes, A.; Milliron, D. J., Defect Chemistry and Plasmon Physics of Colloidal Metal Oxide Nanocrystals. *Journal of Physical Chemistry Letters* **2014**, *5*, 1564-1574.

132. Engel, J. H.; Surendranath, Y.; Alivisatos, A. P., Controlled Chemical Doping of Semiconductor Nanocrystals Using Redox Buffers. *J. Am. Chem. Soc.* **2012**, *134*, 13200-13203.

133. Valdez, C. N.; Braten, M.; Soria, A.; Gamelin, D. R.; Mayer, J. M., Effect of Protons on the Redox Chemistry of Colloidal Zinc Oxide Nanocrystals. *J. Am. Chem. Soc.* **2013**, *135*, 8492-8495.

134. Govorov, A. O.; Zhang, W.; Skeini, T.; Richardson, H.; Lee, J.; Kotov, N. A., Gold Nanoparticle Ensembles as Heaters and Actuators: Melting and Collective Plasmon Resonances. *Nanoscale Research Letters* **2006**, *1*, 84-90.

135. Baral, S.; Miandashti, A. R.; Richardson, H. H., Near-Field Thermal Imaging of Optically Excited Gold Nanostructures: Scaling Principles for Collective Heating with Heat Dissipation into the Surrounding Medium. *Nanoscale* **2018**, *10*, 941-948.

136. Kowalska, E.; Mahaney, O. O. P.; Abe, R.; Ohtani, B., Visible-Light-Induced Photocatalysis through Surface Plasmon Excitation of Gold on Titania Surfaces. *PCCP* **2010**, *12*, 2344-2355.

137. Miyamoto, S., A Theory of the Rate of Sublimation. *Transactions of the Faraday Society* **1933**, *29*, 0794-0797.

138. Freedman, A.; Kebabian, P. L.; Li, Z. M.; Robinson, W. A.; Wormhoudt, J. C., Apparatus for Determination of Vapor Pressures at Ambient Temperatures Employing a Knudsen Effusion Cell and Quartz Crystal Microbalance. *Meas. Sci. Technol.* **2008**, *19*.

139. da Silva, M.; Cabral, J.; Gomes, J. R. B., Experimental and Computational Study on the Molecular Energetics of Indoline and Indole. *J. Phys. Chem. A* **2008**, *112*, 12263-12269.

140. Govorov, A. O.; Richardson, H. H., Generating Heat with Metal Nanoparticles. *Nano Today* **2007**, *2*, 30-38.

141. Coppens, Z. J.; Li, W.; Walker, D. G.; Valentine, J. G., Probing and Controlling Photothermal Heat Generation in Plasmonic Nanostructures. *Nano Lett.* **2013**, *13*, 1023-1028.

142. Ma, H. Y.; Tian, P. F.; Pello, J.; Bendix, P. M.; Oddershede, L. B., Heat Generation by Irradiated Complex Composite Nanostructures. *Nano Lett.* **2014**, *14*, 612-619.

143. Ndukaife, J. C.; Mishra, A.; Guler, U.; Nnanna, A. G. A.; Wereley, S. T.; Boltasseva, A., Photothermal Heating Enabled by Plasmonic Nanostructures for Electrokinetic Manipulation and Sorting of Particles. *Acs Nano* **2014**, *8*, 9035-9043.

144. Agrawal, A.; Singh, A.; Yazdi, S.; Ong, G. K.; Bustillo, K.; Johns, R. W.; Ringe, E.; Milliron, D. J., Resonant Coupling between Molecular Vibrations and Localized Surface Plasmon Resonance of Faceted Metal Oxide Nanocrystals. *Nano Lett.* **2017**, *17*, 2611-2620.

145. Park, J.; An, K. J.; Hwang, Y. S.; Park, J. G.; Noh, H. J.; Kim, J. Y.; Park, J. H.; Hwang, N. M.; Hyeon, T., Ultra-Large-Scale Syntheses of Monodisperse Nanocrystals. *Nat. Mater.* **2004**, *3*, 891-895.

146. Frank, M. M.; Chabal, Y. J.; Green, M. L.; Delabie, A.; Brijs, B.; Wilk, G. D.; Ho, M. Y.; da Rosa, E. B. O.; Baumvol, I. J. R.; Stedile, F. C., Enhanced Initial Growth of Atomic-Layer-Deposited Metal Oxides on Hydrogen-Terminated Silicon. *Appl. Phys. Lett.* **2003**, *83*, 740-742.

147. Frank, M. M.; Chabal, Y. J.; Wilk, G. D., Nucleation and Interface Formation Mechanisms in Atomic Layer Deposition of Gate Oxides. *Appl. Phys. Lett.* **2003**, *82*, 4758-4760.

148. Groner, M. D.; Fabreguette, F. H.; Elam, J. W.; George, S. M., Low-Temperature Al2o3 Atomic Layer Deposition. *Chem. Mater.* **2004**, *16*, 639-645.

149. Levrau, E.; Van de Kerckhove, K.; Devloo-Casier, K.; Sree, S. P.; Martens, J. A.; Detavernier, C.; Dendooven, J., In Situ Ir Spectroscopic Investigation of Alumina Ald on Porous Silica Films: Thermal Versus Plasma-Enhanced Ald. *Journal of Physical Chemistry C* **2014**, *118*, 29854-29859.

150. Weckman, T.; Laasonen, K., First Principles Study of the Atomic Layer Deposition of Alumina by Tma-H2o-Process. *PCCP* **2015**, *17*, 17322-17334.

151. Ephraim, J.; Lanigan, D.; Staller, C.; Milliron, D. J.; Thimsen, E., Transparent Conductive Oxide Nanocrystals Coated with Insulators by Atomic Layer Deposition. *Chem. Mater.* **2016**, *28*, 5549-5553.

152. Meng, L. J.; Yu, R. W.; Qiu, M.; de Abajo, F. J. G., Plasmonic Nano-Oven by Concatenation of Multishell Photothermal Enhancement. *Acs Nano* **2017**, *11*, 7915-7924.

153. Lu, L.; Burkey, G.; Halaciuga, I.; Goia, D. V., Core-Shell Gold/Silver Nanoparticles: Synthesis and Optical Properties. *J. Colloid Interface Sci.* **2013**, *392*, 90-95.

154. Karthika, V.; Arumugam, A.; Gopinath, K.; Kaleeswarran, P.; Govindarajan, M.; Alharbi, N. S.; Kadaikunnan, S.; Khaled, J. M.; Benelli, G., Guazuma Ulmifolia Bark-Synthesized Ag, Au and Ag/Au Alloy Nanoparticles: Photocatalytic Potential, DNA/Protein Interactions,

Anticancer Activity and Toxicity against 14 Species of Microbial Pathogens. *Journal of Photochemistry and Photobiology B-Biology* **2017**, *167*, 189-199.

155. Crockett, B. M.; Jansons, A. W.; Koskela, K. M.; Johnson, D. W.; Hutchison, J. E., Radial Dopant Placement for Tuning Plasmonic Properties in Metal Oxide Nanocrystals. *Acs Nano* **2017**, *11*, 7719-7728.